Doctoral Dissertation

博士論文

Interface control of Al_2O_3-based insulated-gate structures for high-frequency GaN HEMTs

（Al_2O_3 絶縁ゲート構造の界面制御と高周波 GaN HEMT への応用）

Shiro Ozaki

尾崎　史朗

Graduates School of Information Science and Technology
Hokkaido University
北海道大学大学院　情報科学研究科

February, 2019

Acknowlegement

First of all, I would like to express my deepest gratitude to my supervisor, Prof. Tamotsu Hashizume for spending a lot of time on supporting my research, including guidance for my research plans, fruitful discussions on experimental results, and instructive corrections of my research papers. Thanks to his enthusiasm supports and encouragements, I was able to have an invaluable experience that will be of great help to my future work. I am greatly happy to spend these three years under his direction, in Research Center for Integrated Quantum Electronics (RCIQE).

I would like to acknowledge the chief examiner and the co-examiners of my dissertation, Prof. Junichi Motohisa, Prof. Seiya Kasai, and Prof. Taketomo Sato, for spending their precious time on reviewing my dissertation and providing valuable suggestions that helped me to improve the quality of dissertation. I would also like to acknowledge other members of my dissertation committee, Prof. Tetsuya Asai, Prof. Yasuo Takahashi, Prof. Masato Motomura, Prof. Akihiro Murayama, Prof. Tetsuya Uemura, Prof. Kazuhisa Sueoka, Prof. Akihisa Tomita, Prof. Hiromichi Ohta, and Prof. Hajime Igarashi, for reviewing my dissertation and giving me valuable comments at dissertation defense.

I would like to acknowledge Prof. Masayuki Ikebe, Prof. Masamichi Akazawa, Prof. Katsuhiro Tomioka, and Prof. Shinjiro Hara, for their guidance and supports in RCIQE. I could do a productive research because they create and maintain a wonderful research environment.

I wish to thank the members of “Hashizume-group”, Dr. Maciek Matys, Dr. Kenya Nishiguchi, Mr. Shota Kaneki, Mr. Shota Toiya, Mr. Yuji Ando, Mr. Tatsuya Oyobiki, Mr. Shota Sasaki, Mr. Ryota Ochi, and Mr. Yuhei Morishita, for their technical supports of experiments and constructive discussions during my stay, from 2016 to 2019.

I am very grateful to the directors and managers of Fujitsu Laboratories Ltd., Dr. Ei Yano, Dr. Shigenori Aoki, Dr. Keiji Watanabe, Dr. Naoki Hara, Dr. Norikazu Nakamura, Dr. Naoya Okamoto, and Mr. Toshihiro Ohki, for giving me the opportunity to study in RCIQE as a mature student of doctoral course.

I am also grateful to the members of “GaN-group” in Fujitsu Laboratories Ltd., Dr. Masaru Sato, Mr. Masato Nishimori, Dr. Yoshitaka Niida, Ms. Naoko Kurahashi, Mr. Masao Yamada, Mr. Koji Honma, Mr. Mitsuhiro Hoshino, Mr. Kenji Saito, Dr. Junji Kotani, Dr. Atsushi Yamada, Mr. Yoichi Kamada, Dr. Junya Yaita, Mr. Takaaki Sakuyama, Dr. Kozo Makiyama, Mr. Yuichi Minoura, Dr. Yusuke Kumazaki, Mr. Yuichi Yamazaki, Mr. Takayuki Fujiwara, Mr. Takeshi Ito, Mr. Yukio Ito, Mr. Atsushi Takahashi, Mr. Yasuyuki Ishii, Mr. Yoji Tuneki, Ms. Junko Hara, and Mr. Akira Ohgizono, for their constructive discussions at meetings, and technical supports for experiments and device fabrications.

Special thanks to:

Dr. Zenji Yatabe, Dr. Joel T. Asuba, Dr. Chihoko Mizue, Dr. Yujin Hori, Dr. Yin Xiang, Mr. Keisuke Uemura, Prof. Toshikazu Suzuki, Dr. Kunio Tuda, Dr. Yohei Otoki, Dr. Fumimasa Horikiri, Mr. Chihiro Hirooka, Mr. Isao Makabe, Dr. Koji Yoshitsugu, Mr. Hiroshi Nakura, Dr. Ryuichi Sugie, Dr. Tomoji Nakamura, Dr. kenji Ishikawa, Dr. Yoshihisa Iba, Dr. Tomoyuki, Kirimura, Mr. Syunichi Fukuyama, Mr. Hirohumi Watatani, Mr. Yoshiyuki Ohkura, Dr. Kazukiyo Joshin, Mr. Kenji Imanishi, Mr. Masahito Kanamura, Mr. Masayuki Takeda, Mr. Toyoo Miyajima, Dr. Satoshi Masuda, Mr. Motoshu Miyajima, Mr. Yoshihiro Nakata, Mr. Hideki Kitada, Mr. Junichi Kon, Mr. Tsuyoshi Kanki, Mr. Tadahiro Imada, Mr. Yasushi Kobayashi, Ms. Yukiko Oshikubo, Ms. Ayumi Okano, Dr. Hironori Nishino, Dr. Koji Tsunoda, Mr. Kazuo Ozaki, Mr. Kishio Yoneyama, Dr. Tsuyoshi Takahashi, Dr. Kenichi Kawaguchi, Mr. Motonobu Sato, and Dr. Ikuo Soga

最後に、本研究の遂行にあたり筆者を支えてくださった富士通厚木研究所の皆様、友人、家族に心から感謝を申し上げ、謝辞の結びとさせていただきます。

February, 2019

Shiro Ozaki

Contents

Chapter 1

Introduction

1.1. Background of this study

Wireless communication started with telephones, and is connected with computers and mobile phones with the spread of Internet. Use of smartphones has spread globally. As a result, the amount of mobile data traffic is increasing rapidly, a 4000-fold increase in the past ten years. According to a report by Cisco Systems, Inc., the total mobile data traffic will have increased to 49 exabytes/month by 2021, as shown in Fig. 1-1.[1)] Therefore, the communication speed of mobile phones cannot keep up with the increase of mobile data traffic.

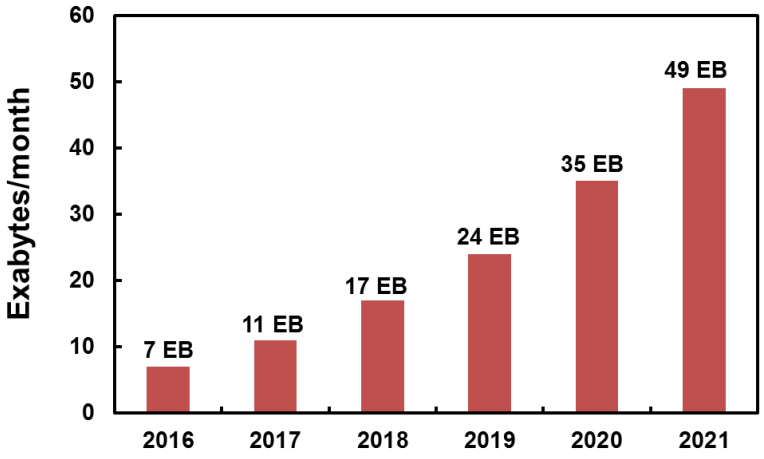

Fig. 1-1. Predicted amount of mobile data traffic in the world.[1)]

1.1.1. Requirements for next generation wireless communication system

In addition to smartphones, the concept of the Internet of Things (IoT) is spreading. In the IoT, various things are connected with the Internet, then the data accumulation and automation of things will be promoted by exchanging information mutually. Technology such as wearable devices, connected cars, and autonomous robots are expected as new

communication terminals connected to the Internet. The amount of wireless data traffic will be overwhelmingly increased due to Machine-to-Machine (M2M) communications. Consequently, it will be difficult to accommodate the data traffic only in the frequency band used in existing wireless communications: less than 6.0 GHz.

Therefore, a millimeter-wave band of 30–300 GHz is expected for the 5th-generation mobile communication system (5G), as a new frequency band. Also, in recent years, high-frequency wireless communications using the W band (75–110 GHz) are drawing increasing interest, both as a way to temporarily set up high-capacity communications for responding to disasters (Fig. 1-2 (a)), and also as a way to bring communications to remote areas where optic cables are difficult to install (Fig. 1-2 (b)). Compared to today's mobile phones using frequency range of 0.8–2.0 GHz, the W band is more than 50 times as broad with 50 times the speed, meaning it is well suited to these high-capacity wireless communications.

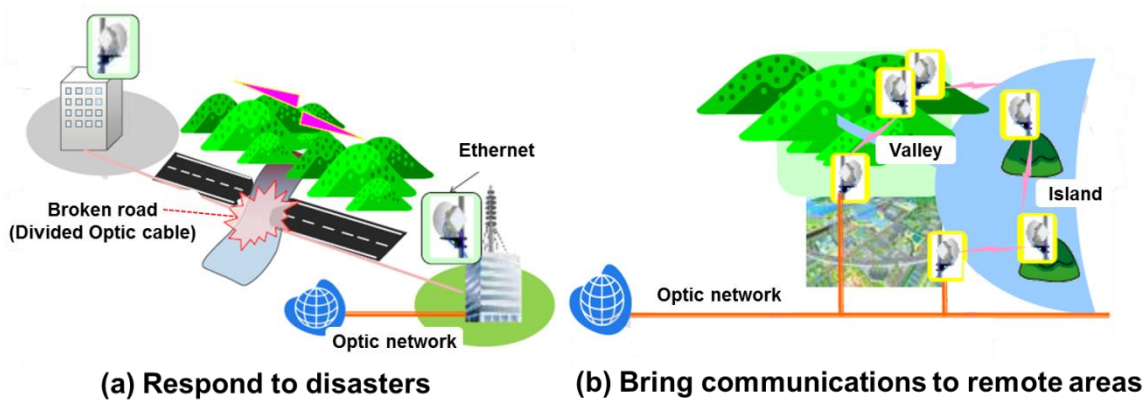

Fig. 1-2. High-frequency wireless communications using W band.

However, when using a millimeter-wave band for high-capacity wireless communications, it will be necessary to solve issues such as insufficient communication distance and the degradation in the atmosphere. Particularly, in the wireless backhaul of mobile communications (Fig. 1-3) where the W band and/or the E band (60–90 GHz) will be used, it is necessary to achieve a communication distance of 10 km and a data rate of 10–20 Gbit/s as the target performance for replacement of the conventional optic cables. To increase distance and capacity, it will be necessary to expand the frequency bandwidth that can be amplified while simultaneously supporting modulation methods

that can transmit more information within the same frequency bandwidth, and a strong requirement is to have less distortion when the signal is amplified. Another objective is keeping in check the energy consumption of the communication systems that accompanies greater distances and capacities, and improved energy efficiency in the power amplifiers. In order to transmit wireless signals over a distance of 10 km in 5G, the transmission antenna needs a power amplifier capable of a high output on the order of several watts. However, the output power of existing power amplifiers for a millimeter-wave band using GaAs or Si-based devices is limited around 0.1 W due to their operating voltage.

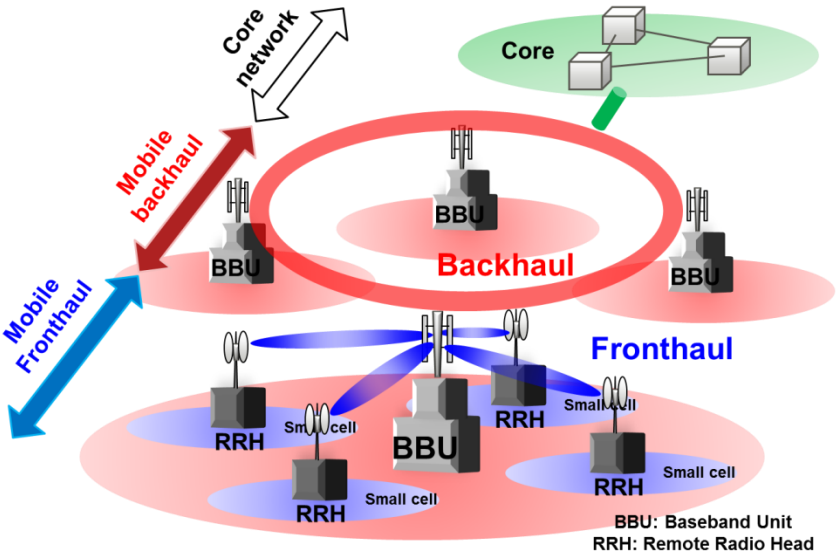

Fig. 1-3. Wireless backhaul of mobile communications.

1.1.2. High-frequency devices

High-frequency devices used for power amplifiers have developed according to each demand such as high-gain, low-noise, high-output, and high-efficiency performance. There are two types of device structure: bipolar junction transistors (BJTs) and field-effect transistors (FETs). In the case of FETs, the structures are divided into metal-semiconductor (MES), p-n junction, metal-oxide-semiconductor (MOS) FETs, and high electron mobility transistors (HEMTs), as shown in Fig. 1-4. In high-frequency applications, MOSFETs and HEMTs are desirable to obtain high-gain performance due to the high mobility of the two-dimensional channel. In particular, HEMTs using

heterostructures of compound semiconductors such as GaAs, InP, and GaN-based materials, are widely used as high-frequency devices applied in the information and communications field, due to the excellent high-speed and low-noise performance.

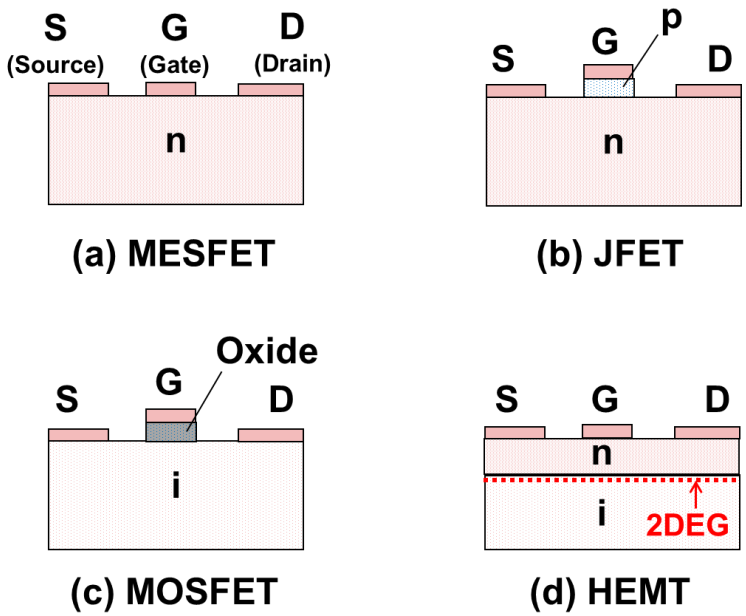

Fig. 1-4. Schematic cross-sectional view of FETs for high-frequency applications.

1.2. High electron mobility transistors (HEMTs)

This section describes HEMTs as the background of this thesis focusing on insulated-gate structures for HEMTs, from invention to commercial production.

The electron transport phenomenon in the semiconductor superlattice was first discussed by Esaki *et al*. in 1969, and Dingle *et al*. found that the in-plane mobility was dramatically increased by the modulation-doped AlGaAs/GaAs superlattice structures.[2)] The transistor that can control this outstanding electronic transport phenomenon by the electric field effect is HEMT. This concept was proposed by Mimura *et al*. in 1980 with two-dimensional electron gas (2DEG) induced by the interface of the AlGaAs/GaAs single heterojunction.[3)] These days, HEMTs are widely used as high-frequency devices applied in the information and communications field, in applications such as satellite broadcast receivers, mobile phones, and millimeter-wave radars for automobiles, due to the excellent high-speed and low-noise performance. In addition, HEMTs are also used

in radio telescopes for discovering unknown interstellar molecules. This has contributed to progress in basic science. Owing to these achievements, Dr. Mimura, inventor of HEMT, was honored with the 33rd Kyoto Prize (Advanced Technology Division), sponsored by the Inamori Foundation, in 2017.

1.2.1. Concept of HEMT

During the initial development of the HEMT in 1979, Dr. Mimura participated in research on the GaAs MOSFET for two years.[4)] The MOSFET is widely known as an indispensable device for large-scale integrations (LSIs), and the purpose of his study was to explore the possibility of LSIs with GaAs MOSFETs. His aim in particular was to reduce the electronic states at the oxide/GaAs interface to achieve an electron accumulation in the GaAs layer. Various methods were applied to reduce the electronic states at the oxide/GaAs interface, but it was difficult to observe the electron accumulation. Concerned about GaAs MOSFET, he became interested in the "modulation-doped heterojunction superlattices" reported by R. Dingle *et al*.[2)] In this structure, donor-doped AlGaAs layers and non-doped GaAs layers are stacked alternately, and electrons accumulate in the non-doped GaAs layer between the n-type AlGaAs layers.

From this phenomenon, he conceived the idea of the HEMT in July 1979.[4, 5)] The concept of HEMT is field-effect control of the high-mobility electron in selectively doped GaAs/n-AlGaAs heterostructures. Figure 1-5 shows the band diagram of the HEMT.[3)] If we regard the depleted n-type AlGaAs layer as a gate insulator film such as silicon dioxide (SiO_2), the device concept of the HEMT is structurally similar to the MOSFETs. At the same time, the Schottky barrier junction used to deplete the n-type AlGaAs layer has the function of the gate electrode in GaAs MESFETs. Therefore, we can understand that the concept of HEMT was based on the principle of GaAs MESFET and MOSFET (Fig. 1-6).

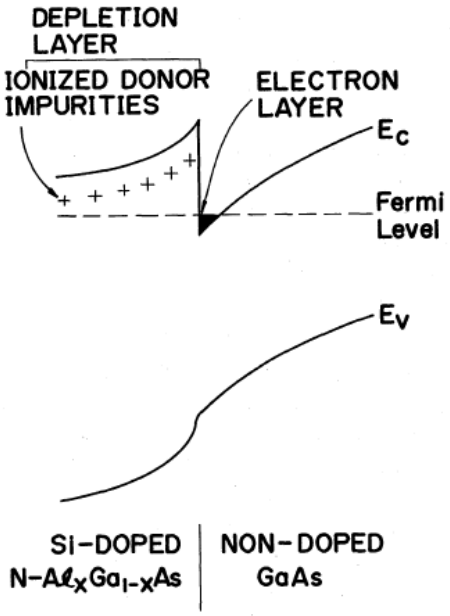

Fig. 1-5. Band diagram of HEMT proposed by Dr. Mimura (Reproduced from ref. 3, with the permission of IOP publishing).

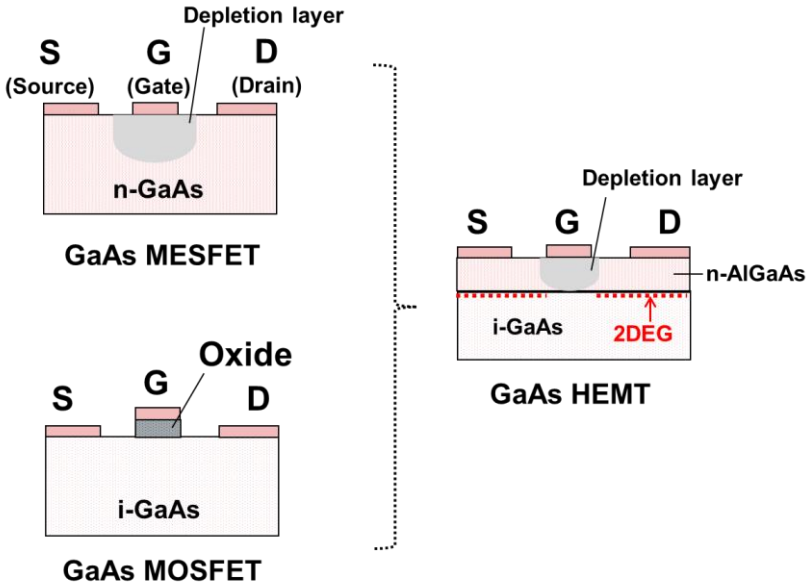

Fig. 1-6. Concept of HEMT based on principle of GaAs MESFET and MOSFET.

1.2.2. Development of fabrication process for HEMTs

The HEMT began to show potential as a high-frequency device soon after its first fabrication. However, there were serious issues to achieve precise control of device dimensions.[6] In the HEMT, an extremely thin AlGaAs layer existed under the gate electrode, and the thickness of this layer had to be controlled to obtain stable threshold voltage. However, AlGaAs is chemically unstable compared with GaAs because of the presence of aluminum (Al). Thus, aluminum oxide (Al_2O_3) was easily generated at the surface of the AlGaAs layer due to exposure to the air. As a result, the effective thickness of the AlGaAs layer was reduced by oxidation.

To resolve this issue, Dr. Mimura developed process technologies using a GaAs cap layer on the AlGaAs layer and reactive ion etching to remove this before gate electrode formation. The advantage of this technology was surface protection for the AlGaAs layer from exposure to the air. Thus, the thickness of the AlGaAs layer could be precisely controlled, the same as after crystal growth. This technology enabled the HEMTs to be fabricated with uniform characteristics and good repeatability for mass production.

1.2.3. Commercialization of HEMTs

The commercialization of HEMTs started at the IEEE International Solid-State Circuits Conference (ISSCC) held in 1983.[7] A researcher associated with the National Radio Astronomy Observatory in the United States showed an interest in the presentation on HEMT low-noise amplifiers for application to satellite communications in the microwave band, because the noise characteristics of HEMT in a low-temperature environment had the potential to replace existing parametric amplifiers or GaAs MESFET amplifiers. Taking this opportunity, low-noise amplifiers for radio telescopes became the first target of the application of HEMTs. The HEMT amplifiers were installed at the Nobeyama Radio Observatory of the National Astronomical Observatory of Japan in 1985, and contributed to the discovery of an unknown hydrocarbon molecule in a dark nebula.[8]

The use of HEMTs began to become widespread in 1987 when they came to replace the conventional GaAs MESFETs as low-noise amplifiers in converters for satellite broadcast receivers. HEMTs enabled parabolic antennas to be downsized to less than half the size of the conventional ones and contributed to the explosive growth of satellite broadcasting in Japan, Europe, and elsewhere. Figure 1-7 shows the progress in

noise figures of GaAs HEMTs and MESFETs at 12 GHz satellite broadcasting frequency.[9] Noise figures for Si MOSFETs and BJTs at different frequencies are plotted for reference. In 1983, there was no significant difference in performance between GaAs HEMTs and MESFETs. However, as HEMTs began to be evaluated by users, the progress in low-noise technology accelerated following user feedback. As a result, the noise figure of HEMTs was reduced to approximately 0.3 dB and the downsizing effect in parabolic antennas used for receiving satellite broadcasts reached its limit, leading to the expansion of satellite broadcasting.

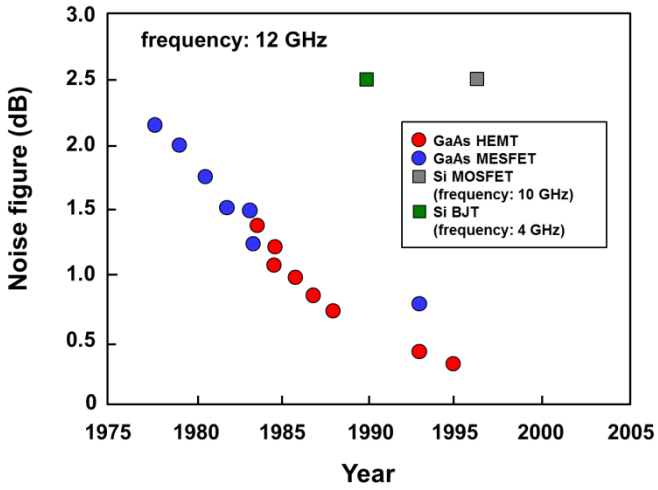

Fig. 1-7. Progress in noise figures of GaAs HEMTs and MESFETs at 12 GHz.[9]

Another feature of HEMTs is their ability to be applied in various kinds of compound semiconductors as mentioned in 1.1.2. In addition to the conventional GaAs HEMTs, the research and development of ultra-high-frequency HEMTs using InP and high-efficiency/high-power HEMTs using GaN is progressing. It is expected that InP-based HEMTs will be applied to high-speed downloaders and image sensing used in security checks. GaN-based HEMTs are already used in wireless base stations and contribute to power savings and downsizing in the 4th-generation mobile communication system (4G), instead of conventional GaAs HEMTs.[10]

1.3. High-frequency GaN HEMTs

As described above, HEMTs using GaN-based materials have realized excellent power characteristics, and will be indispensable for the next generation of power amplifiers in wireless communication systems and radar systems. For example, in mobile phone base stations and WiMAX using a frequency range of 1–2 GHz, 100 W-class power amplifiers are necessary to achieve adequate communication distance and data rate. However, in the case of conventional GaAs MESFETs and Si MOSFETs, the output power is less than 100 W with one chip. Therefore, two or more chips are necessary for the 100 W-class power amplifiers by parallel distribution. On the other hand, the output power of GaN HEMTs is more than 100 W with one chip. As a result, parallel distribution and synthetic circuits are unnecessary. Thus, small and high-efficiency power amplifiers can be achieved with GaN HEMTs.

1.3.1. GaN-based materials

Table 1-1 shows a comparison in the physical properties of the semiconductor materials used in high-frequency devices. GaN has a bandgap three times wider than Si and GaAs. Owing to its wide band gap, GaN exhibits stable operation even at high temperatures. Thus, the cooling system can be minimized in power amplifiers. Furthermore, the breakdown electric field of GaN is larger than 3 MV/cm, which is approximately one order of magnitude higher than that of Si and GaAs, meaning it is well suited to high-power applications. In addition, the electron mobility and electron velocity are very important for high-frequency devices. Electron mobility is defined as:

$$v = \mu E \,, \tag{1-1}$$

where v, μ, and E are electron velocity, electron mobility, and electric field, respectively. However, the electron velocity is not determined by only electron mobility. S. C. Jain *et al*. reported the relationship between electron velocity and the electric field of semiconductor materials calculated by Monte Carlo simulations.[11] The peak velocity and saturation velocity of GaN are 3×10^7 cm/s and 1.5×10^7 cm/s, respectively. Both values are higher than those of Si and GaAs.

Furthermore, Johnson's figure of merit shows the potential of semiconductor materials for high-frequency devices.[12] It is defined as:

$$V_m f_T = \frac{E_B v_s}{2\pi} , \tag{1-2}$$

where V_m and f_T are the maximum allowable applied voltage and cutoff frequency, respectively. Figure 1-8 shows Johnson's figure of merit of each semiconductor material. The f_T of GaN is one order of magnitude larger than that of GaAs at the same V_m. Thus, GaN-based materials are desirable for power amplifiers used in high-frequency and high-power applications.

Table. 1-1. Comparison in physics properties of semiconductor materials.

	Si	GaAs	SiC	GaN
Bandgap (eV)	1.1	1.4	3.2	3.6
Breakdown electric field (MV/cm)	0.3	0.4	3.0	3.0
Thermal conductivity (W/cmK)	1.5	0.5	4.9	1.5
Carrier concentration (/cm^2)	～10^{12}	～10^{12}	～10^{12}	～10^{13}
Electron mobility (cm^2/Vs)	1300	8000	600	2000
Electron saturation velocity (cm/s)	1.0 × 10^7	1.3 × 10^7	2.0 × 10^7	2.7 × 10^7

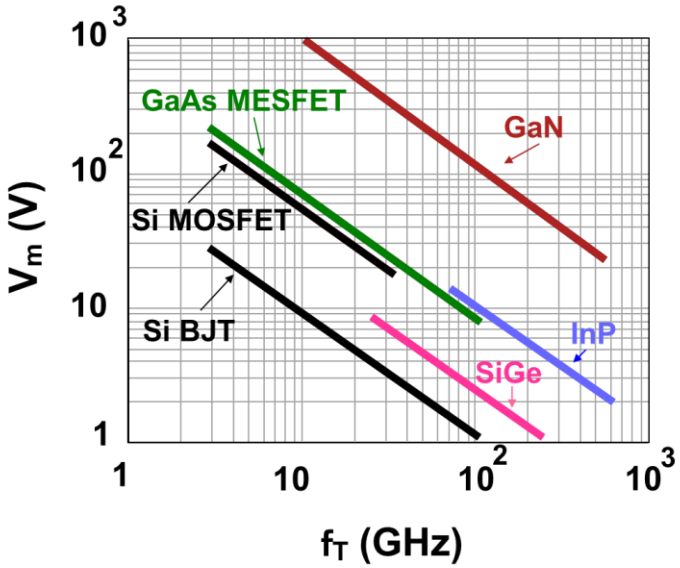

Fig. 1-8. Johnson's figure of merit of each semiconductor materials.

1.3.2. GaN-based HEMTs

One of the primary advantages of GaN-based HEMTs is the 2DEG generated at the interface of heterostructures such as AlGaN/GaN and InAlN/GaN. Figure 1-9 shows the typical structure and band diagram of the AlGaN/GaN heterostructure. When AlGaN is grown on the GaN layer, the high-density/high-mobility electron channel is generated at the AlGaN/GaN interface due to the spontaneous and piezoelectric polarization. Generally, those GaN and AlGaN layers are grown without doping. Thus, the electron mobility is higher than that of SiC MOSFETs because of the suppression in the impurity scattering at the AlGaN/GaN interface. At the same time, the typical electron density is over 1×10^{13} cm^{-2}, which is approximately one order of magnitude higher than that of Si MOSFETs. These characteristics are well suited for power amplifiers.

Furthermore, it is known that GaN HEMTs using In-based barrier layers such as InAlN and InAlGaN are promising, because of their high spontaneous polarization and high band offset at the conduction band, for enhancing 2DEG density.[13, 14] In fact, Makiyama *et al*. demonstrated an output power density of 4.5 W/mm at 94 GHz in GaN HEMTs using InAlGaN barrier layers as shown in Fig. 1-10.[15] These characteristics are

desirable for 5G communication systems where the W band (75–110 GHz) and the E band (60–90 GHz) frequency ranges are expected to be used for the wireless backhaul of mobile communications.

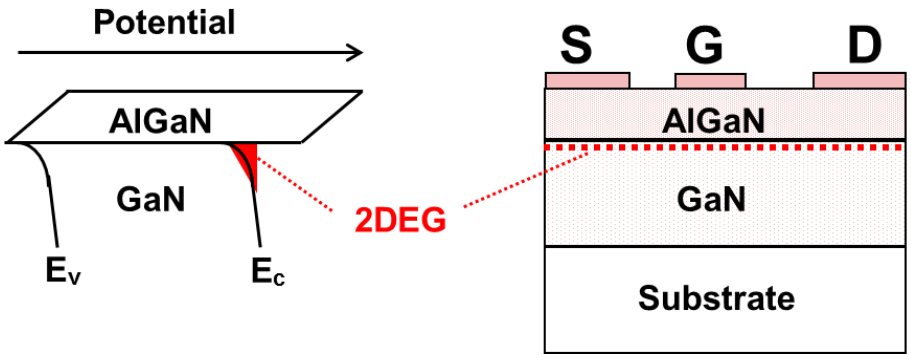

Fig. 1-9. Typical structure and band diagram of the AlGaN/GaN heterostructure.

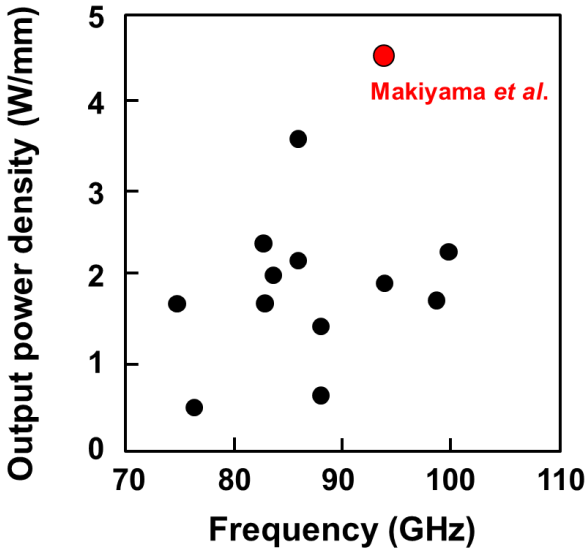

Fig. 1-10. Comparison in performance of GaN HEMT power amplifiers.

1.4. Insulated-gate structures for high-frequency GaN HEMTs

In next-generation wireless communications, including 5G, high-efficiency and high-linearity power amplifiers are required in wireless base stations. However, power amplifiers using Schottky-gate (SG) GaN HEMTs suffer from reduced gain and efficiency with increasing input radio frequency (RF) power due to significant gate leakage current caused by a large input swing that may drive the devices deep into the forward bias regime. Such high leakage currents seriously affect the operation stability and large signal linearity of power amplifiers. Insulated-gate structures are very effective in overcoming problems related to SG structures. In fact, Kanamura *et al*. demonstrated that gate leakage current of AlGaN/GaN HEMTs was sufficiently reduced by a SiN-based insulated-gate structure even under high input power operations, as shown in Fig. 1-11.[16)]

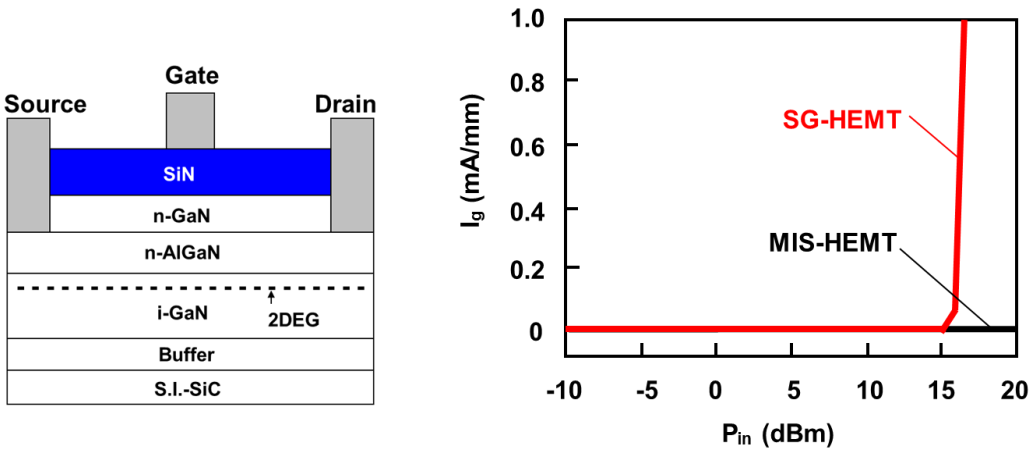

Fig. 1-11. Reduction in gate leakage current of AlGaN/GaN HEMTs using SiN-based insulated-gate structures.[16)]

Among the various kinds of insulators that have been applied in insulated-gate structures for GaN HEMTs, the candidates are limited because of the wide bandgap of GaN-based materials.[17)] In the case of Si- and GaAs-based devices, the bandgap of SiN is enough to block the electrons and holes at the conduction band and valence band, respectively. However, in the case of AlGaN/GaN HEMTs, the band offsets between SiN and AlGaN are less than 1 eV, as shown in Fig. 1-12. Thus, the higher forward gate

bias induces the higher gate leakage current due to the Fowler–Nordheim tunneling process, leading to electron injection. This causes degradation of performance and reliability.

Furthermore, in the case of InAlN/GaN HEMTs, an insulated-gate structure is indispensable. As mentioned in 1.3.2, GaN HEMTs using In-based barrier layers such as InAlN and InAlGaN are promising because of their high spontaneous polarization and high band offset at the conduction band, for enhancing 2DEG density. However, the large gate leakage current in InAlN/GaN HEMTs often limits their operation. Furthermore, in the case of InAlN/GaN HEMTs, the band offsets between insulator and barrier layer are smaller than that of AlGaN/GaN HEMTs.

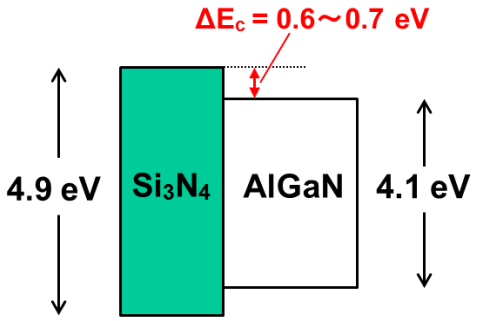

Fig. 1-12. Band offsets between Si_3N_4 and AlGaN.

Figure 1-13 shows the relationship between the bandgap and the dielectric constant of insulators. Although the bandgap of SiO_2 is highest in Fig. 1-13, the dielectric constant is very low (less than 5). If we use low-dielectric-constant materials for the gate insulator, the transconductance (g_m) of metal-insulator-semiconductor (MIS)-HEMTs will be decreased, and this causes RF performance degradations. On the other hand, the bandgaps of high-dielectric-constant materials such as HfO_2 and ZrO_2, are less than 6 eV. This value is insufficient as the barrier for GaN-based materials, as shown in Fig. 1-12. In this regard, Al_2O_3 is a good candidate for the gate insulator film used in GaN-based devices due to the wide bandgap and relatively high dielectric constant. In fact, Z. H. Liu *et al*. demonstrated the improved RF performances of 0.25 μm GaN metal-oxide-semiconductor (MOS)-HEMTs using 8 nm atomic-layer-deposited (ALD) Al_2O_3 films for low-noise amplifiers.[18)]

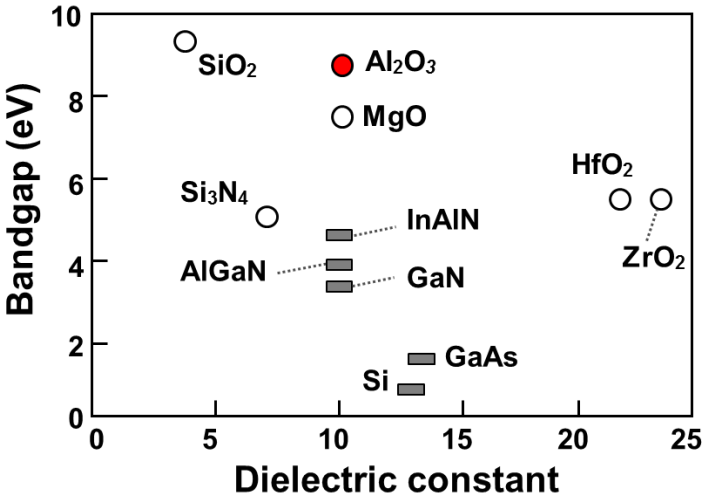

Fig. 1-13. Relationship between bandgap and dielectric constant of insulators.

1.5. Issues for insulated-gate GaN HEMTs

Power amplifiers using SG GaN HEMTs are already used in wireless base stations and contribute to power savings and downsizing. However, MIS-HEMTs and MOS-HEMTs using insulated-gate structures have not yet been used in mass production, because of the insufficient operation stability due to the electronic states at the insulator/semiconductor interface. As well as with GaN-based materials, it is also difficult to control the insulator/semiconductor interface when using other compound semiconductor materials. As mentioned in 1.2, Dr. Mimura, inventor of HEMT, gave up the development of GaAs MOSFETs because of the electronic states at the oxide/GaAs interfaces. Up to now, while various kinds of insulators have been applied to improve the performance and operation stability of insulated-gate structures for GaN HEMTs, several problems remain unsolved.[17)]

1.5.1. Instability of threshold voltage

The most serious problem is threshold voltage (V_{th}) instability, as shown in Fig. 1-14. It is considered that the V_{th} shift occurred due to an electron trap at the insulator/barrier

(AlGaN or InAlN) interface during a positive gate-voltage (V_{gs}) sweep, and this causes degradation in operation stability.[19] Therefore, the V_{th} shift is one of the critical issues to be solved for high-frequency and high-power applications. Several papers report that different bias conditions induce varying degrees of V_{th} shift in insulated-gate HEMTs. Lu *et al*. reported that the higher positive gate bias of the insulated-gate HEMTs induces larger V_{th} shift toward the forward bias direction.[20] There are two possible mechanisms for this issue. Under a high positive gate bias, the Fowler–Nordheim tunneling process enhances the gate leakage current, as mentioned in 1.4. In this case, electrons injected into trap levels in insulators cause excess negative charges, resulting in the V_{th} shift toward the positive bias direction. The high positive gate bias also supplies electrons to electronic states at the insulator/barrier interface, and the acceptor-type states produce negative charges when they trap electrons. Due to the long associated time constant for electron emission even at room temperature, electrons captured at deeper interface states remain trapped for the entire duration of gate sweeping toward the negative bias direction.[21] This also causes the V_{th} shift toward the positive bias direction in the I_{ds}–V_{gs} characteristics, as shown in Fig. 1-14.

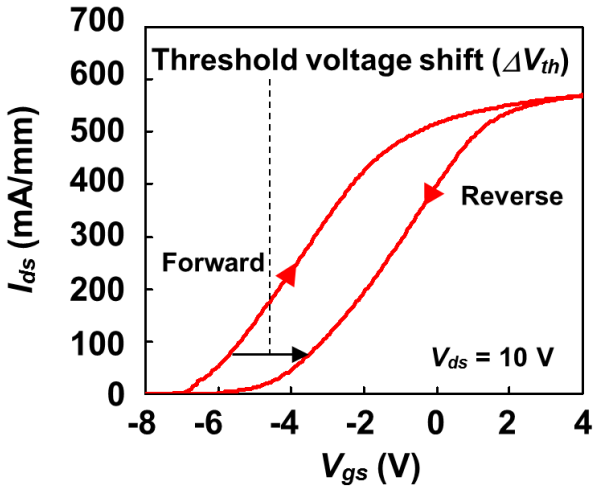

Fig. 1-14. V_{th} shift of insulated-gate GaN HEMTs due to positive gate bias.

1.5.2. Degradation of current linearity at forward gate bias

Another problem of insulated-gate structures is an unexpected degradation of current linearity.[22] Although a dynamic range of input-signal sweeping is one of the advantages

of insulated-gate GaN HEMTs, the sudden current saturation at the forward gate bias was reported, as shown in Fig. 1-15.[22, 23)] It is likely that a high density of electronic states at the insulator/barrier interface, in particular near the conduction band edge, screens the gate electric field and causes limited control of the surface potential of the barrier layer. This prevents further increase in the 2DEG density, leading to pronounced current saturation at the forward gate bias. Such degradation of current linearity can be responsible for gain loss and degradation of large-signal linearity in power amplifiers.

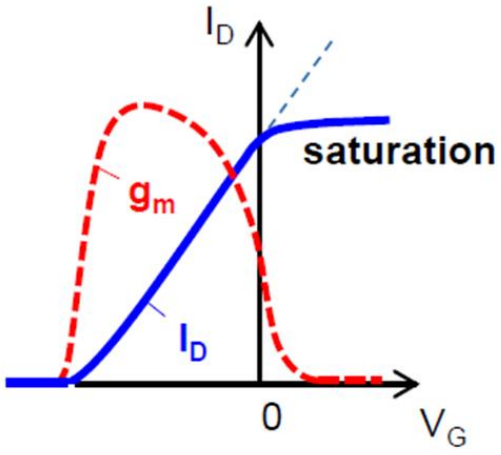

Fig. 1-15. Sudden current saturation at forward bias of insulated-gate GaN HEMTs (Reproduced from ref. 22, copyright 2017 by the Japan Society of Applied Physics).

1.5.3. Current collapse

Current collapse is one of the critical issues for operation stability, because it causes RF performance degradation, due to the decrease in the drain current under operation. Figure 1-16 shows the pulsed I_{ds}–V_{ds} characteristics of AlGaN/GaN HEMTs. A significant current decrease is observed under the off-state quiescent bias with a high drain voltage ($V_{gs\text{-}q}$ = -3 V and $V_{ds\text{-}q}$ = 20 V). In addition, this quiescent bias made gate control of the current very difficult, indicating that the pronounced current collapse behavior was due to the surface charging and the potential pinning at the AlGaN surface, particularly in the gate-to-drain access region. According to the widely accepted "virtual gate" model,[24)] as shown in Fig. 17, a high off-state drain bias voltage induces electron

trapping at the surface states of the barrier layer via a tunneling injection at the gate edge on the drain side. Subsequently, surface charges deplete the underlying 2DEG and increase the drain resistance, leading to current collapse. Current collapse is strongly dependent on the drain voltage during the off-state stress.[25, 26] On the basis of the gate injection and surface-hopping model,[27, 28] electron conduction via trap-to-trap hopping can be promoted with an increasing drain voltage. Consequently, this may lead to the widening of the "virtual gate" from the gate edge up to some further distance on the gate-to-drain access region.[29]

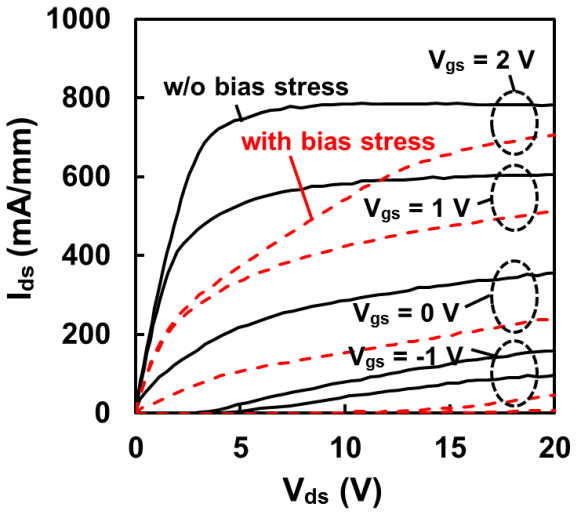

Fig. 1-16. Current collapse of AlGaN/GaN HEMTs.

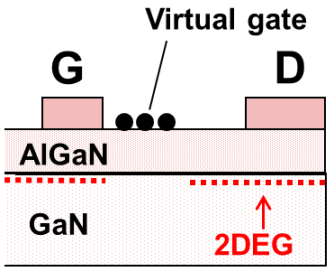

Fig. 1-17. Schematic illustration of virtual gate model for current collapse.

1.6. Objective

As discussed above, GaN HEMTs have enormous potential as high-frequency devices used in power amplifiers. In addition, insulated-gate structures are effective for improving the performance of GaN HEMTs in RF applications. Especially, Al_2O_3 is a good candidate for gate insulator film of GaN HEMTs due to the wide bandgap and relatively high dielectric constant. However, several problems remain unsolved, such as an instability of the V_{th}, a steep decrease in g_m at the forward gate bias, and severe current collapse.

In this thesis, to improve the performance and the operation stability of GaN HEMTs using Al_2O_3-based insulated-gate structures, the electrical properties are characterized by focusing on fabrication processes such as an ALD, post-deposition and post-metallization annealing (PMA), and methods of interface control are proposed.

1.7. Outline

The rest of this thesis is organized as follows.

Chapter 2 explains the basics of the physical properties of GaN and related heterostructures. The spontaneous and piezoelectric polarizations at the AlGaN/GaN heterostructure and the generation mechanism of the 2DEG are described.

Chapter 3 introduces the origin and effects of the electronic states induced at the interface between insulators and GaN-based materials. Furthermore, the evaluation methods of the interface states are explained, focusing on the capacitance–voltage (*C*–*V*) characteristics of the MOS structures.

Chapter 4 investigates the mechanism for V_{th} shift of AlGaN/GaN MOS-HEMTs when using ALD-Al_2O_3 for the gate insulator films. As an oxidant source for ALD-Al_2O_3, H_2O vapor and O_2 plasma were compared, focusing on $Al(OH)_x$ residues in ALD-Al_2O_3 and GaN oxidation at the Al_2O_3/GaN interface. The oxidant source was controlled for ALD-Al_2O_3, and a hybrid-Al_2O_3 structure (lower H_2O vapor-Al_2O_3/upper O_2 plasma-Al_2O_3) was proposed to reduce the V_{th} shift and the gate leakage current.

Chapter 5 discusses the effect of oxidant sources on the performance of InAlN/GaN MOS-HEMTs. Surface-oxide-control for the InAlN barrier layer was proposed to reduce the gate leakage current and the current collapse of InAlN/GaN MOS-HEMTs by focusing on In_2O_3, which has narrow bandgap and chemically unstable properties, compared with Al_2O_3.

Chapter 6 investigates the DC characteristics and operation stability of

Al_2O_3/InAlN/GaN MOS-HEMTs by focusing on the PMA process to control the defect levels in Al_2O_3 and the electronic states at the Al_2O_3/InAlN interface. The relationship between the *I*–*V* characteristics (the transconductance linearity, the subthreshold slope, and the current collapse) and the electronic states at the Al_2O_3/InAlN interface were evaluated by photo-assisted *C*–*V* measurements. Furthermore, TEM analysis of the Al_2O_3/InAlN structures was conducted to reveal the bond disorder at the Al_2O_3/InAlN interface by focusing on the relaxation of dangling bonds and/or point defects. Finally, the reduction in the oxygen-related defects in Al_2O_3 and the electronic states at the Al_2O_3/InAlN interface were demonstrated by optimized PMA, which led to improved gate controllability and operation stability for the Al_2O_3/InAlN/GaN MOS-HEMTs.

Chapter 7 summarizes the results presented in this thesis.

References

1) Cisco Visual Networking Index: Global Mobile Data Traffic Forecast Update, 2016-2021.
2) R. Dingle, H. L. Stormer, A. C. Gossard, and W. Wiegmann, Appl. Phys. Lett. **33**, 665 (1978).
3) T. Mimura, S. Hiyamizu, T. Fujii and K. Nanbu, Jpn. J. Appl. Phys. **19**, L225 (1980).
4) T. Mimura, Journal of the Institute of Image Information and Television Engineers **52**, 4 (1998).
5) T. Mimura, Japan Patent 1409643 (1979).
6) T. Mimura, Society of Semiconductor Industry Specialists, Encore, 66 (2010).
7) M. Niori, T. Saito, K. Joshin, and T. Mimura, ISSCC Tech. Dig., 198 (1983).
8) H. Suzuki, M. Ohishi, N. Naifu, S. Ichikawa, T. Kasuga, S. Saito, and K. Kawaguchi, Jpn. Publ. Astron. Soc. Japan, **38**, 911 (1986).
9) T. Mimura, IEICE Transactions J100-C, 10 (2017).
10) K. Inoue, and L. Yue, MWE Tech. Dig., FR2B-3 (2017).
11) S. C. Jain, M. Willander, J. Narayan, and R. Van Overstraeten, J. Appl. Phys. **87**, 965 (2000).
12) E. O. Johnson, RCA Rev. **26**, 163 (1965).
13) J. Kuzmik, IEEE Electron Device Lett. 22, 510 (2001).
14) K. Joshin, K. Makiyama, S. Ozaki, T. Ohki, N. Okamoto, Y. Niida, M. Sato, S. Masuda, and K. Watanabe, IEICE Trans. Electron. E97-C, 923 (2014).
15) K. Makiyama, S. Ozaki, Y. Niida, T. Ohki, N. Okamoto, Y. Minoura, M. Sato, Y. Kamada, K. Joshin, N. Nakamura, and Y. Miyamoto, ICNS Tech. Dig., C1.1 (2017).
16) M. Kanamura, T. Kikkawa, T. Iwai, K. Imanishi, T. Kubo, and K. Joshin, IEDM Tech. Dig., 572 (2005).
17) T. Hashizume, K. Nisgiguchi, S. Kaneki, J. Kuzmik and Z. Yatabe, Mat. Sci. Semicond. Process. **78**, 85 (2018).
18) Z. H. Liu, G. I. Ng, S. Arulkumaran, Y. K. T. Maung, K. L. Teo, S. C. Foo, and V. Sahmuganathan, IEEE Electron Device Lett. **31**, 803 (2010).
19) T. Imada, K. Motoyoshi, M. Kanamura, and T. Kikkawa, IEEE Integrated Reliability Workshop Final Report, 38 (2011).
20) Y. Lu, S. Yang, Q. Jiang, Z. Tang, B. Li, and K. J. Chen, Phys. Status Solidi C **10**, 1397 (2013).

21) Z. Yatabe, J. T. Asubar, and T. Hashizume, J. Phys. D **49**, 393001 (2016).
22) K. Nishiguchi, S. Kaneki, S. Ozaki, and T. Hashizume, Jpn. J. Appl. Phys. 56, 101001-1-8 (2017).
23) Z. Zhang, W. Li, K. Fu, G. Yu, X. Zhang, Y. Zhao, S. Sun, L. Song, X. Deng, Z. Xing, L. Yang, R. Ji, C. Zeng, Y. Fan, Z. Dong, Y. Cai, and B. Zhang, IEEE Electron Device Lett. **38**, 236 (2017).
24) R. Vetury, N. Q. Zhang, S. Keller, and U. K. Mishra, IEEE Trans. Electron Devices. **48**, 560 (2001).
25) W. Saito, T. Nitta, Y. Kakiuchi, Y. Saito, K. Tsuda, I. Omura, and M. Yamaguchi, IEEE Trans. Electron Devices. **54**, 1825 (2007).
26) S. Arulkumaran, I. G. Ng, C. H. Lee, Z. H. Liu, K. Radhakrishnan, N. Dharmarasu and Z. Sun, Solid-State Electron. **54**, 1430 (2010).
27) R. J. Trew, D. S. Green, and J. B. Shealy, IEEE Microwave Mag. **10**, 116 (2009).
28) J. Kotani, M. Tajima, S. Kasai, and T. Hashizume, Appl. Phys. Lett. **91**, 093501 (2007).
29) K. Nishiguchi, J. T. Asubar, and T. Hashizume, Jpn. J. Appl. Phys. **53**, 070301 (2014).

Chapter 2

Physical properties of GaN and related heterostructures

2.1. Basic properties of III-N semiconductor materials

2.1.1. Crystal structures

III-N semiconductors have a hexagonal wurtzite structure due to the strong ionicity of the chemical bonds between cation and anion atoms in the crystals. In the case of the wurtzite structure, the cation and anion atoms align in the same direction (vertically, in this case) as shown in Fig. 2-1 (a), while they align rotating by 60 degrees in the zincblend structure (b). Such symmetrical configurations with the ionic alignment lead to characteristic polarization effects. Furthermore, the wurtzite structure is thermodynamically favorable and easy to produce (for all binary, ternary, and quaternary alloys).[1)] Thus, a wurtzite structure is generally used in GaN-based devices, including high electron mobility transistors (HEMTs).

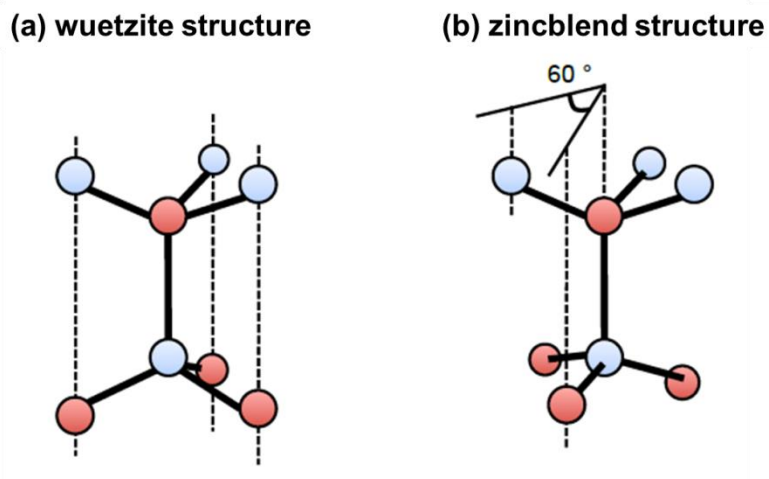

Fig. 2-1. Schematic illustrations of (a) wurtzite and (b) zincblend crystal structures.

Figure 2-2 shows the definition of lattice constant and orientations in the hexagonal wurtzite crystal. As shown in this figure, the c-axis direction [0001] is the same as that of the strong ionicity. Therefore, the polarization characteristics are generated along the c-axis. Thus, the c-plane (0001), oriented perpendicular to the c-axis, is called the "polar plane." On the other hand, the a-plane (11–20) and m-plane (1–100) do not have the polarization effects because of the atom configurations. Indeed, GaN HEMTs are generally fabricated on the c-plane of GaN-based materials. This feature will be discussed later in this chapter.

Furthermore, the lattice constants of the wurtzite crystal are defined as *a* and *c*, as shown in Fig. 2-3. Each lattice constant depends on the ionicity in the crystal. Table 2-1 summarizes the lattice parameters and bandgap of wurtzite AlN, GaN, and InN.[2)]

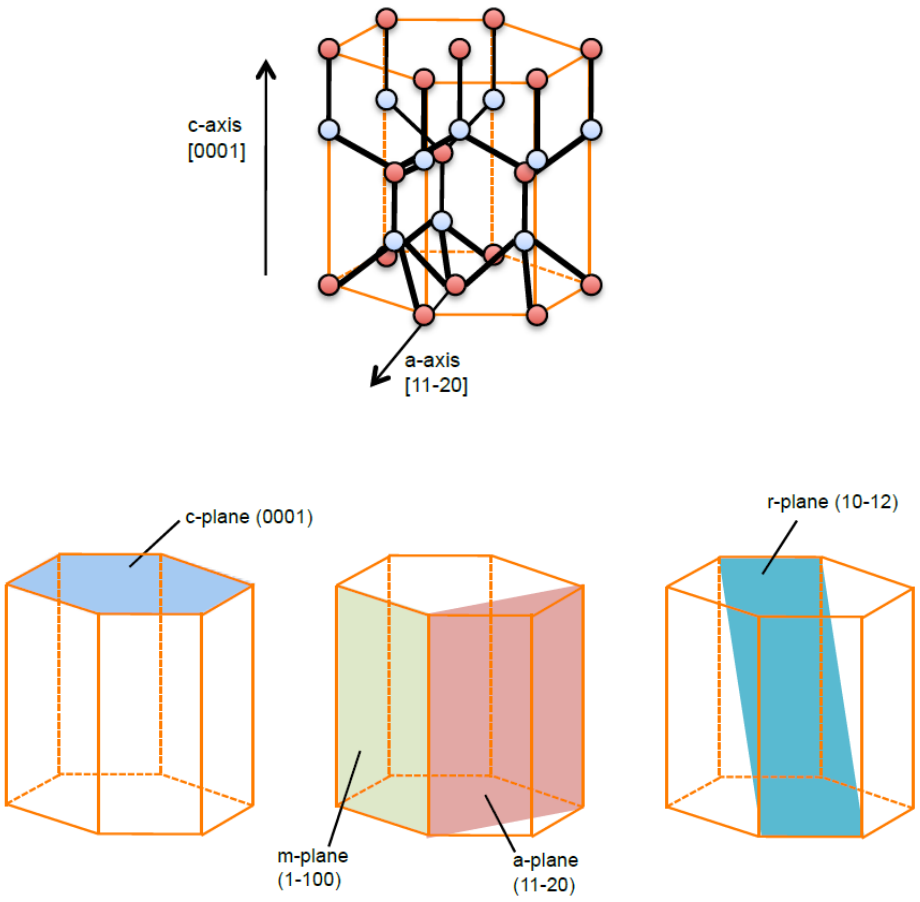

Fig. 2-2. Schematic illustrations of wurtzite crystal and its direction and orientations.

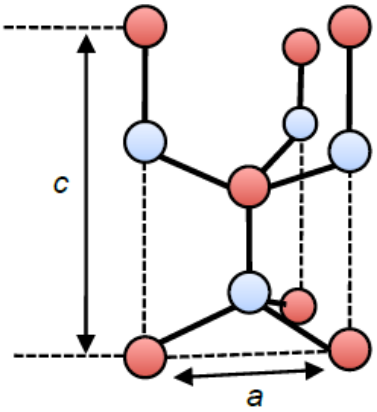

Fig. 2-3. Definition of lattice constants of wurtzite crystal.

Table 2-1. Lattice parameters and bandgap of wurtzite AlN, GaN, and InN.[2)]

	AlN	GaN	InN
Lattice constant *a* (Å)	3.112	3.189	3.545
Lattice constant *c* (Å)	4.982	5.185	5.703
Bandgap at RT (eV)	6.25	3.51	0.78

2.1.2. Epitaxial growth of III-N semiconductors

Epitaxial growth of III-N semiconductors is generally performed on foreign substrates such as Si, SiC, and sapphire due to the lack of commercial bulk substrates. In this case, a strong lattice mismatch is observed between III-Ns and substrates, as shown in Table 2-2, which of course has profound consequences for material growth and characteristics. As shown in Fig. 2-4, heteroepitaxial growth can occur basically in three ways. III-Ns grow lattice-mismatched with the substrate inducing either pseudomorphic or relaxed conditions. In strained structures (pseudomorphic), in-plane deformation (biaxial) occurs and the layer is either compressed or tensed. In this case, defects such as mosaicity, disorientation with respect to the growth axis, heterostructure curvature, and inhomogeneities can eventually appear.[3)] Some of the most important structural defects that occur in III-Ns growth are related with relaxation and dislocation formation. The relaxation can be correlated to the loss of biaxial deformation, with respect to the strained accommodation of the crystal lattice of the grown layer. It can be evaluated by the relaxation coefficient defined as:

$$R = \frac{a(layer) - a_0(substrate)}{a_0(layer) - a_0(substrate)}, \tag{2-1}$$

where the subindex 0 is related to the layer in its state of no deformation. The degree of relaxation will be zero when the layer is fully strained and 1 when the layer is completely relaxed (absence of biaxial strain).

Dislocations are linear defects occurring during material growth and that propagate into the material and are due to displacement of atoms in the lattice. In fact, relaxation of materials can occur via dislocation formation. Edge-type and screw-type dislocation may be the origin depending on the mechanism of formation.

Table 2-2. Lattice parameters of available substrates for III-Ns growth and lattice mismatch with GaN. Values for GaN are a = 3.189 Å and c = 5.185 Å.

Substrate	a (Å)	c (Å)	$\Delta a_{GaN}/a_{sub}$ (%)
SiC	3.081	5.039	3.5
Sapphire	4.758	12.991	16.1
Si (111)	3.840	5.438	-17.0

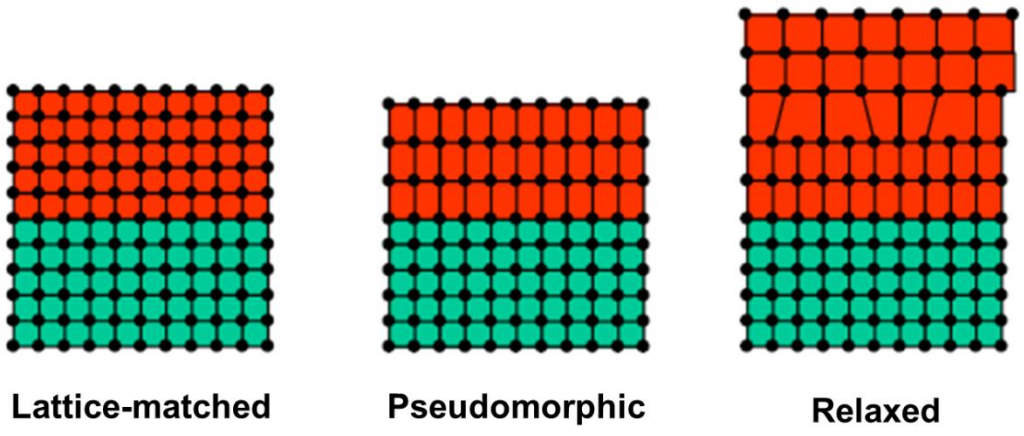

Fig. 2-4. Schematic illustrations for types of heteroepitaxial growth.

2.2. AlGaN/GaN heterojunction

2.2.1. Alloys and heterojunctions using III-N semiconductors

III-N semiconductors also enable us to realize various types of III-N alloys having different bandgap and lattice constant. The ternary III-N, $A_xB_{1-x}N$, can be carefully engineered in respect to composition. The behavior of the lattice parameter *a* and bandgap E_g with the change of composition can be described by Vegard's law:

$$a(A_xB_{1-x}N) = xa_A + (1-x)a_B \,, \tag{2-2}$$

$$E_{g,A_xB_{1-x}N} = xE_{g,A} + (1-x)E_{g,B} + bx(1-x) \,, \tag{2-3}$$

where *b* is the bowing parameter and *x* is the molar fraction of A. Figure 2-5 shows the relationship between lattice constant and bandgap for GaN, AlN, InN, and their alloys. With a bandgap between 0.78 eV and 6.25 eV and lattice parameter *a* from 3.112 Å to 3.545 Å, the AlGaN alloys offer broad engineering possibilities. InAlN has an additional unique feature for HEMTs. When the In composition ratio is 17%, the lattice constant of $In_{0.17}Al_{0.83}N$ in accordance with that of GaN is prepared on the c-plane of the GaN layer. Besides that, the large conduction-band offset at the InAlN/GaN interface can be a big advantage for HEMT applications.

AlGaN is an alloy of AlN and GaN. AlGaN/GaN heterojunctions are the most popular application for HEMTs, as shown in 1.3.2. Comparing with the InAlN/GaN system, AlGaN and GaN have no lattice-matching selections, resulting in tensile-straining in the AlGaN/GaN heterostructures. This feature leads to polarization effects, which will be explained in the next section.

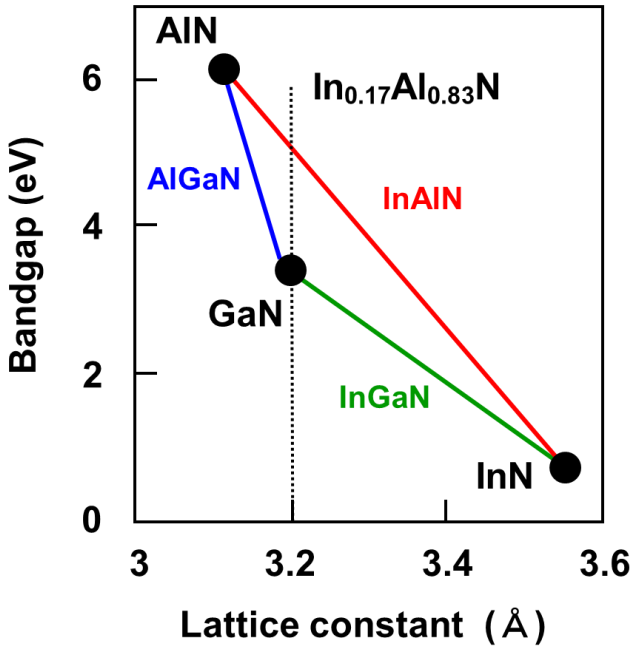

Fig. 2-5. Relationship between lattice constant and bandgap for GaN, AlN, InN, and their alloys.

2.2.2. Polarization effects in III-N heterojunctions

As shown in Fig. 2-2, III-N semiconductors grown on the c-plane lead to "spontaneous polarization" due to the symmetric configuration of cations and anions in the c-axis direction. Ambacher *et al*.[4] calculated the spontaneous polarization charge densities P_{sp} for GaN, AlN, and InN are

GaN: $P_{sp} = -1.8 \times 10^{13}$ /cm^2,
AlN: $P_{sp} = -5.1 \times 10^{13}$ /cm^2,
InN: $P_{sp} = -2.0 \times 10^{13}$ /cm^2.

The polarization charges are induced both on the c-plane and the opposite c-plane, as shown in Fig. 2-6. At the (0001) Ga-face surface, the negative charges are induced by the cation atoms, Ga, Al, and In, resulting in the internal electric field in the [000-1] direction. At the (000-1) N-face surface, on the other hand, the internal electric field shows the [0001] direction.

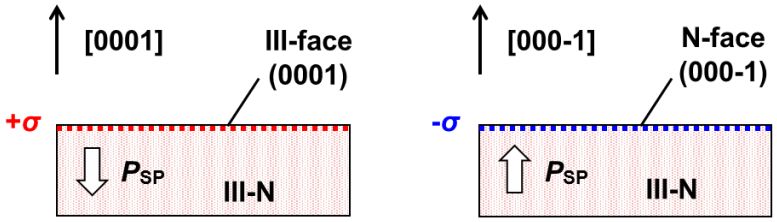

Fig. 2-6. Spontaneous polarization and internal electric fields in III-N semiconductors.

In addition to spontaneous polarization, the lattice strain and compression due to the lattice-mismatched junction lead to "piezoelectric polarization." Let us consider this polarization effect in the AlGaN/GaN heterojunction. As schematically shown in Fig. 2-7, the AlGaN layer that has a smaller lattice constant *a* than that of GaN is strained in the horizontal direction so that it cancels the lattice-constant difference. Consequently, the compression of the AlGaN in the vertical (c-axis) direction leads to an increase in the internal electric field due to the piezoelectric polarization. As shown in Fig. 2-7, in the heterojunction grown on the (0001) orientation, the piezoelectric field shows the [000-1] direction, which is the same as that of the spontaneous polarization. Therefore, by either spontaneous or piezoelectric polarization, or by both, the potential of the heterojunction is bent downward, leading to accumulation of the two-dimensional electron gas (2DEG).

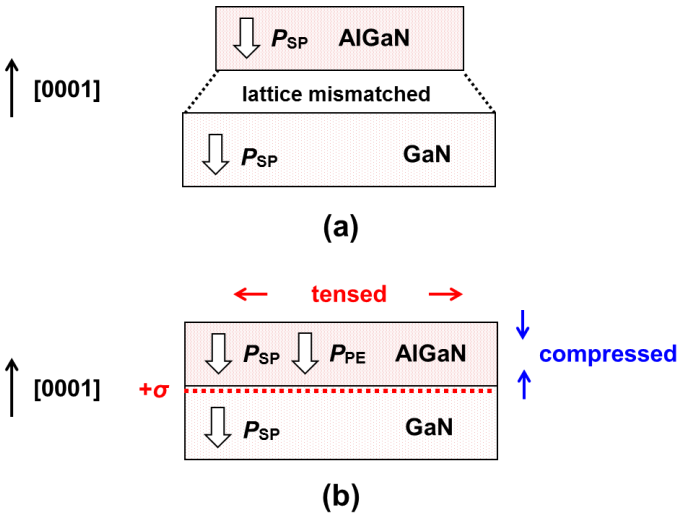

Fig. 2-7. Piezoelectric polarization in III-N heterostructures.

2.2.3. Two-dimensional electron gas induced at III-N heterointerfaces

Figure 2-8 shows the band diagram of the AlGaN/GaN heterojunction at equilibrium. As mentioned above, the band bent downward by the internal electric fields create the potential quantum well at the AlGaN/GaN interface. As a result, 2DEG with high electron density is induced at the heterointerface. The electron mobility of such 2DEG is not affected by the impurity scattering because those internal electric fields are induced even in un-doped III-N systems. Note that the origin of 2DEG has not been cleared yet, but is under discussion. III-N electron devices utilizing such 2DEG are called as HEMTs or heterojunction-field-effect transistors.

Ibbetson *et al*. proposed the following equation for the calculation 2DEG density:

$$qn_s = \sigma_{PZ}(1 - t_{CR}/t), \tag{2-4}$$

where n_s, σ_{PZ}, t_{CR}, and t are 2DEG density, polarization-induced charge at AlGaN/GaN interface, the critical thickness, and the thickness of AlGaN layer, respectively.[5)]

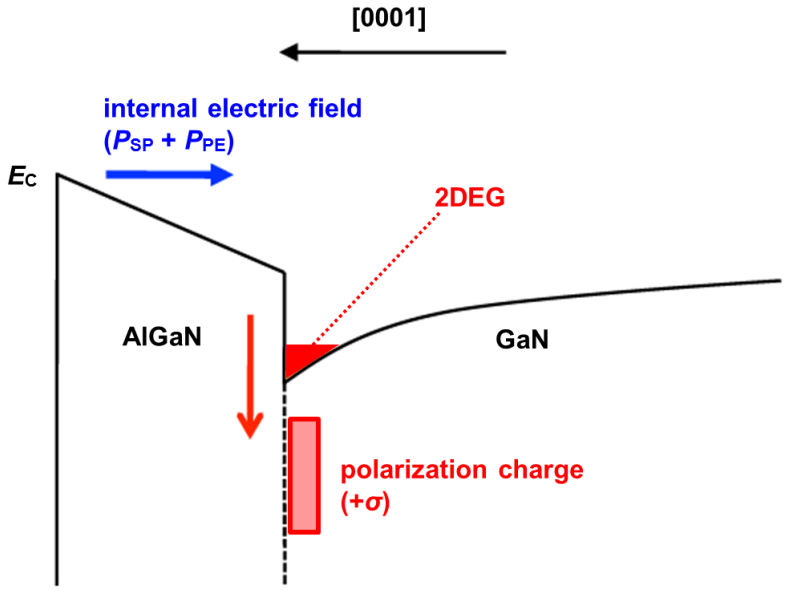

Fig. 2-8. Conduction-band diagram of AlGaN/GaN heterostructure.

Table 2-3 shows the polarization charge density and the conduction-band offsets reported for the AlGaN/GaN and InAlN/GaN heterostructures.[6] ΔP_0 is the spontaneous polarization charge density difference between the barrier and channel layers. P_{total} is the total polarization charge density at the heterointerface as described using ΔP_0 and the piezoelectric polarization charge density P_{PE},

$$P_{total} = \Delta P_0 - P_{PE}. \tag{2-5}$$

When the Al composition ratio is 20% in the AlGaN/GaN heterostructure, the resulting P_{total} is 1.18×10^{13} cm^{-2}, which is one order of magnitude higher than the inversion carrier densities at Si and SiC MOS interfaces. Using $In_{0.17}Al_{0.83}N$ as a barrier layer of HEMTs, the lattice-matched InAlN/GaN heterojunction shows P_{PE} of zero. However, higher P_{SP} of InAlN gives the positive ΔP_0 with density two times higher compared with that of AlGaN, resulting in P_{total} of 2.73×10^{13} cm^{-2}. The larger conduction-band offset at the InAlN/GaN interface is also expected to suppress the gate leakage current under a forward gate bias.

Table 2-3. Polarization effect parameters and conduction-band offset of III-N heterostructures.[6]

	ΔP_0 (cm^{-2})	ΔP_{PE} (cm^{-2})	ΔP_{total} (cm^{-2})	ΔE_c (eV)
$Al_{0.2}Ga_{0.8}N/GaN$	6.50×10^{12}	5.32×10^{13}	1.18×10^{13}	0.30
$In_{0.17}Al_{0.83}N/GaN$	2.73×10^{13}	0	2.73×10^{13}	0.68

In the case of the AlGaN/GaN heterojunction, the P_{SP} is proportional to the Al composition ratio of AlGaN, leading to higher-density 2DEG. The typical Al composition ratio of AlGaN, which is usually used for HEMTs, is around 20–35%, resulting in 2DEG density of around 10^{13} cm^{-2}. Fig. 2-9 shows the relationship between the 2DEG density and the thickness of AlGaN with an Al composition ratio of 34%.[5] Ideally, 2DEG density increases with the AlGaN thickness due to the increase of P_{PE}. In a real case, the lattice strain can be relaxed with the thicker growth of AlGaN, resulting in the saturation of the 2DEG density. Furthermore, the thinner AlGaN also relaxes the

compression of itself, leading to decrease of P_{PE}. As a consequence, when the resulting ΔP_0 is zero, the heterojunction system does not create the 2DEG channel. In the AlGaN/GaN heterostructure, therefore, 2DEG density can be modulated utilizing the Al composition ratio and the thickness of the AlGaN barrier layer.

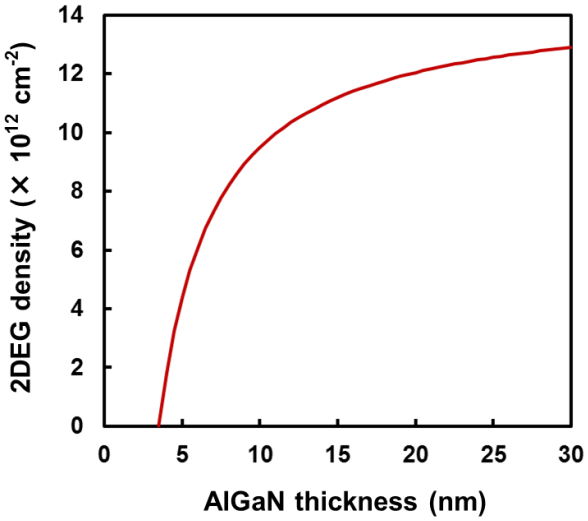

Fig. 2-9. Relationship between the 2DEG density and the thickness of AlGaN with the Al composition ratio of 34%.[5)]

References

1) S. Strite, and H. Morkoc, J. Vac. Sci. Technol. B **10**, 1237 (1992).
2) I. Vurgaftman, and J. R. Meyer, J. Appl. Phys. **94**, 3675 (2003).
3) M. A. Moram, and M. E. Vickers, Reports on Progress in Physics **72**, 036502 (2009).
4) O. Ambacher, J. Smart, J. R. Shealy, N. G. Weimann, K. Chu, M. Murphy, W. J. Schaff, and L. F. Eastman, J. Appl. Phys. **85**, 3222 (1999).
5) J. P. Ibbetson, P. T. Fini, K. D. Ness, S. P. DenBaars, J. S. Speck, and U. K. Mishra, Appl. Phys. Lett. **77**, 250 (2000).
6) J. Kuzmík, IEEE Electron Device Lett. **22**, 510 (2001).

Chapter 3

Basics on insulated-gate structures and characterization of insulator/semiconductor interface

3.1. Introduction

To develop insulated-gate structures applicable to practical GaN-based devices, the characterization of metal-insulator-semiconductor (MIS) or metal-oxide-semiconductor (MOS) interface properties have become of utmost importance for understanding the underlying physics and chemistry required for circumventing problematic issues. Although different insulator materials have been used in GaN-based devices, including high electron mobility transistors (HEMTs), the resulting insulator/III-N semiconductor interfacial properties are still not fully understood.

Thus, this chapter introduces the origins and effects of the electronic states induced at the interface between insulators and GaN-based materials. Furthermore, the evaluation methods of the interface states are described, focusing on the capacitance–voltage (*C–V*) characteristics of the MOS structures.

3.2. Origin of surface and interface states

3.2.1. Fermi level pinning

The basic idea about band alignment at the metal-semiconductor (M-S) interface is to align the bands naturally with each other, keeping the energy distance of each band from the vacuum level unchanged at the interface. This is the well-known Mott-Schottky limit. In reality, however, as shown in Fig. 3-1, there is a strong tendency for the metal Fermi level to align with a characteristic energy position of the semiconductor E_0. This makes the value of Schottky barrier heights (SBH) independent or weakly dependent on the metal work function. This phenomenon is called “Fermi level pinning.” How strongly the barrier height ϕ_{B} depends on the metal work function ϕ_{m} is usually expressed phenomenologically in terms of the interface index *S* defined by:

$$S = \frac{d\phi_B}{d\phi_m}. \tag{3-1}$$

Using S, SBH can be expressed as:

$$\phi_B = S(\phi_m - \chi_s) + (1 - S)(E_C - E_0), \tag{3-2}$$

where χ_s is the electron affinity of the semiconductor. $S = 1$ corresponds to the Mott-Schottky limit and $S = 0$ corresponds to the completely pinned limit (Bardeen limit).

Extensive studies on semiconductor surfaces and interfaces carried out in the last 10–30 years have revealed that Fermi level pinning also exists on free surfaces, at insulator-semiconductor (I-S) interfaces and heterojunction (S-S) interfaces. In order to explain the origin of Fermi level pinning, several models were proposed.

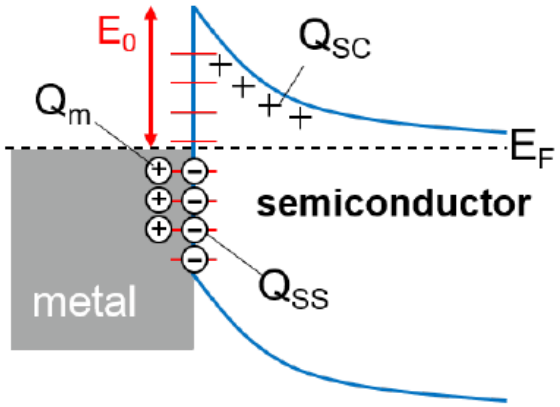

Fig. 3-1. Schematic illustration of Fermi level pinning due to surface states.

3.2.2. Charge neutrality level

Hasegawa *et al*. stressed that M-S, S-S, and I-S interfaces are closely connected through the so-called charge neutrality level (CNL), which can be defined as the boundary energy at which states in the gap state continuum change from a donor-type to acceptor-type character with increasing energy.[1)] In a one-dimensional model of a semiconductor, this boundary energy is the branch point energy of the complex band structure, and it lies at the midgap.[2)] In a three-dimensional crystal, the energy position of CNL can be determined as the zero point of the cell-averaged real-space Green's function,[2)] as the average hybrid orbital energy position in the tight-binding theory of

the bands,[1] as the midgap point of the dielectric energy gap (dielectric midgap),[3] or as the empirical tight-binding branch point energy.[4]

The roles of the CNL at the interface are as follow: (1) the reference energy for band lineup at the S-S interface; (2) the Fermi level pinning point at the M-S interface in the Bardeen limit; and (3) the Fermi level pinning point at the I-S interface. Thus, it is an energy reference point of fundamental importance for interfaces.

3.2.3. Metal-induced gap state model

In 1965, V. Heine proposed that the evanescent tails of the wave functions in metals effectively serve interface states and pin the Fermi level, as shown in Fig. 3-2.[5] Tersoff later called these types of states the metal-induced gap states (MIGS), and showed the way to calculate the position of the CNL of these states as the pinning point.[2] Fermi level pinning by MIGS is schematically shown in Fig. 3-3 (a). It should be noted that this model applies only to the pinning at the M-S interface and the pinning should be intrinsic.

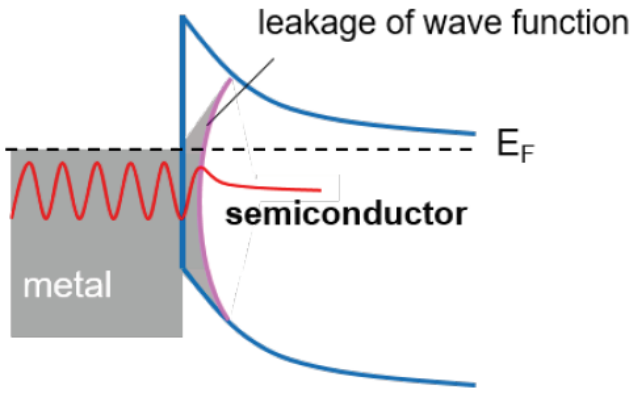

Fig. 3-2. Schematic illustration of MIGS model.

3.2.4. Disorder-induced gap state model

In 1986, Hasegawa and Ohno proposed a disorder-induced gap state (DIGS) model, in which the disorder of bonds near the interface, caused by the interface formation process, produces an interface state continuum due to incomplete separation of bonding

and anti-bonding states.[1)] The Fermi level pinning mechanism is similar to that of the MIGS model, as shown in Fig 3-3 (a). However, the origin of the states is different and the pinning in the DIGS model is an intrinsic one. Additionally, the DIGS model applies not only to the M-S interface but also to the free surfaces and the I-S interfaces as well as to defective S-S interfaces. The primary difference between the MIGS and the DIGS model is that Fermi level pinning may be avoided or inevitable. In the MIGS model, the pinning is intrinsic; due to the simultaneous occurrence of extrinsic defects, the *S* value can decrease but the pinning does not disappear. On the other hand, in the DIGS model, pinning disappears and the Schottky-Mott limit can be realized if the interface disorder is removed by improving the interface formation process. Teraji and Hara found that the *S* value could be changed from 0.22 to 0.99 in SiC, and a Schottky-Mott extreme of S = 0.99 realized by changing the interface formation process.[6)] Furthermore, Hasegawa *et al*. conducted a pulse electrochemical process that can form an oxide-free interface without process damage to form metallic dots. As a result, it is possible to get S = 0.4 in GaAs and InP, which are relatively pinning materials with $S \simeq 0.1$, and get $S \simeq 1$ when the dot size is small.[7–9)]

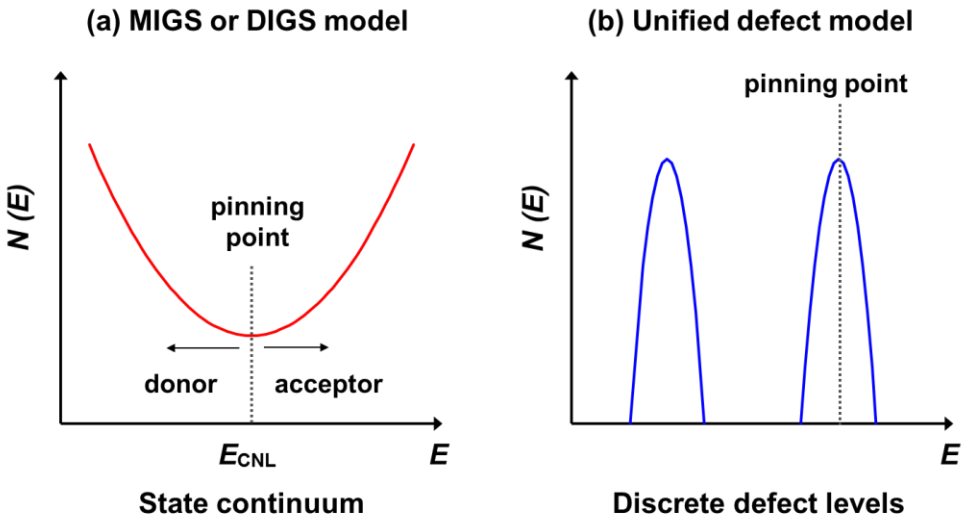

Fig. 3-3. Fermi level pinning mechanisms for (a) MIGS or DIGS, and (b) Unified defect model.

3.2.5. Unified defect model

As another model of extrinsic pinning, Spicer *et al*. proposed a unified defect model in which near-interface discreet levels on the semiconductor side due to processing induced native defects serve as the pinning states, as shown in Fig. 3-3 (b).[10] The unified defect model applies not only to the M-S interface but also to the free surface and I-S interface. This model is a persuasive model but it does not give the experimentally observed pinning positions.

3.2.6. Border trap model

To explain the instability of MOS structures using GaAs, InP, and InGaAs, a border trap (BT) model was proposed.[11] This model assumes defect levels inside the gate insulator, as shown in Fig. 3-4 (a). In this case, BTs have long time constants as they interact with the conduction band electrons via tunneling, leading to large frequency dispersion of *C*–*V* characteristics even at accumulation bias, as shown in Fig. 3-5.[12–15] The DIGS model, as schematically shown in Figure 3-4 (b), can well explain frequency dispersion at accumulation bias.[1, 16, 17] In this model, it is assumed that the disordered region at the semiconductor surface includes defects, dangling bonds and lattice displacement (disorder in bond lengths and angles), thereby producing electronic states with density distributions in both energy and space. When interface states have space distribution, electron capture/emission processes also include tunneling effects. Recently, Galatage *et al*. reported a comparison of the BT and DIGS models by fitting both models to experimental data.[15] Although both models suggested that frequency dispersion was caused by high-density electronic states within 0.8 nm from the crystalline semiconductor surface, they claimed that the experimental capacitance frequency dispersion in accumulation can be well explained by the DIGS model. This led them to conclude that frequency dispersion is indeed due primarily to DIGSs in the semiconductor side. Moreover, since the *C*–*V* frequency dispersion in InGaAs MOS structures has been observed for a variety of dielectrics, including Al_2O_3; HfO_2; ZrO_2; LaAlO; and HfAlO, it is unlikely that the same BT would have almost the same energy from the InGaAs conduction band edge can be consistently reproduced using different dielectric materials. Furthermore, Choi *et al*. theoretically predicted that the oxygen vacancies in the Al_2O_3 films act as BTs that lead to the leakage current in Al_2O_3/GaN MOS structures.[18] Defect levels in insulator films, BTs in insulator films near the I-S interface, and acceptor-type interface states at the I-S interface are involved in the

threshold voltage shift (ΔV_{th}) mechanism in GaN MOS-HEMTs.[17] Higher forward gate bias induces a higher gate leakage current, probably via the Fowler–Nordheim tunneling process, leading to electron injection to traps and interface states. This causes instability of V_{th} in GaN MOS-HEMTs, as described in 1.5.1.

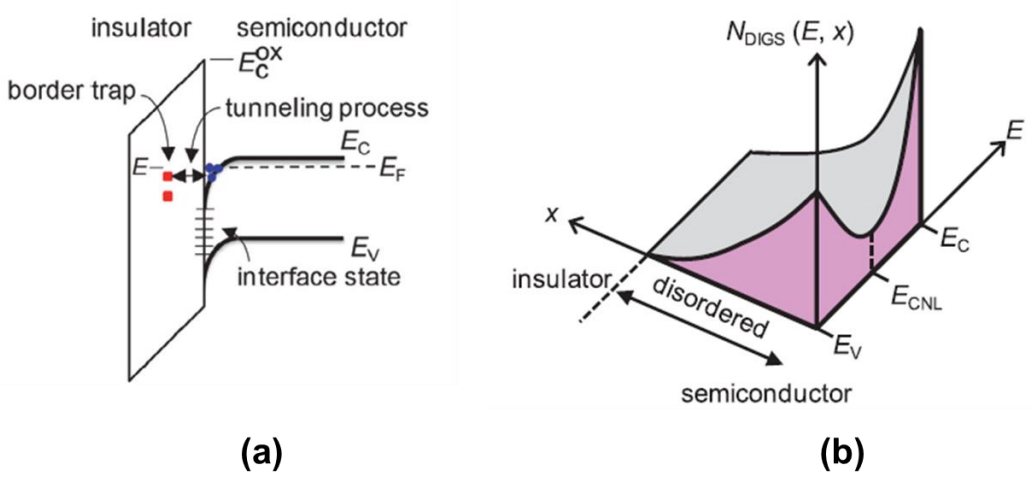

Fig. 3-4. Schematic illustrations of (a) border trap and (b) disorder-induced gap state model (Reproduced from ref. 17, with the permission of IOP publishing).

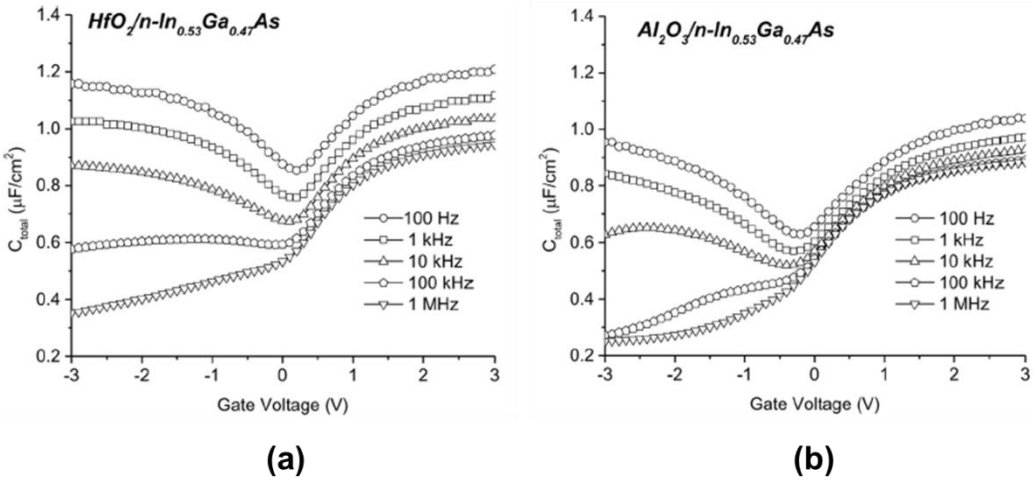

Fig. 3-5. *C*–*V* characteristics as function of frequency of (a) HfO_2 and (b) Al_2O_3 on n-InGaAs (Reproduced from ref. 15, with the permission of AIP publishing).

3. 3. Characterization of interface states for insulated-gate GaN HEMTs

To obtain stable V_{th} and gate controllability of insulated-gate GaN HEMTs, it is very important to characterize the electronic states at the insulator/barrier interface. From the viewpoint of device application, it is desirable to evaluate interface state properties using an actual HEMT structure with a very thin barrier layer (less than 30 nm) such as AlGaN or InAlN. However, in comparison with a conventional insulated-gate structure using a single semiconductor layer, it is very difficult to characterize the insulator/barrier interface. Insulated-gate HEMTs have two interfaces: insulator/barrier and barrier/GaN. This makes the potential modulation rather complicated because the applied field is divided into three parts: insulator, barrier, and GaN layers.

Accordingly, this section presents the characterization of electronic states at the insulator/barrier interface, particularly focusing on Al_2O_3/AlGaN/GaN structures. To understand the basic behavior of interface states in MOS-HEMTs, *C–V* characteristics are calculated by a numerical solver of the one-dimensional Poisson equation.[19)] Furthermore, interface states near the midgap are characterized by photo-assisted *C–V* technique.[20, 21)]

3.3.1. Capacitance-voltage characteristics of MOS-HEMTs

Figure 3-6 (a) shows the calculated *C–V* characteristics of Al_2O_3/AlGaN/GaN structures assuming physical parameters summarized in Table 3-1. As shown in Fig. 3-6 (a), the ideal *C–V* curve shows a two-step capacitance change, which is the characteristic feature of the MOS-HEMT structure having two interfaces.[20)] The nearly flat capacitance C_{TOTAL} around zero bias indicates that 2DEG accumulates at the AlGaN/GaN interface. When we apply the positive gate bias, electrons start to distribute in the AlGaN layer, leading to an increase of capacitance to the insulator capacitance C_{Al2O3}. The two broken lines show an example of the *C–V* calculation assuming the two typical interface state density (D_{it}) distributions, D_{it1} and D_{it2}, shown in Fig. 3-6 (b). In the D_{it} distributions, the CNL (E_{CNL}) is a branch point for acceptor- and donor-like interface states having a U-shaped distribution, which is in accordance with the DIGS model, as explained in 3.2.4. D_{it} distributions assumed in the calculation are expressed by:

$$D_{it}^{A,D}(E) = D_{it0}\,exp\left[\left(\frac{\left|E - E_{CNL}\right|}{E_{0A,0D}}\right)^{n_{A,D}}\right], \tag{3-3}$$

where E_{0A} and n_A are the curvature of the acceptor-like D_{it}^{A} branch, E_{0D} and n_D are the curvature of donor-like D_{it}^{D} branch, respectively, and D_{it0} is the minimum density at E_{CNL}. Additionally, we also took into account time constants for electron emission from the interface states using the Shockley-Read-Hall (SRH) statistics. Time constant τ as a function of the trap energy level E_T can be calculated using the following equation:

$$\tau = \frac{1}{\sigma N_C \upsilon} exp\left(\frac{E_C - E_T}{kT}\right), \tag{3-4}$$

where k, T, and σ are the Boltzmann constant, temperature, and the capture cross section of the interface states, and N_C and v are the effective density of states in the conduction band of the AlGaN and the thermal velocity of electrons, respectively. For example, in the case of AlGaN with an Al composition of 30% (E_g = 4.0 eV), the time constant for electron emission to the conduction band is estimated to be in the 10^{10}-10^{20} s range for near-midgap states at room temperature (RT) and even at 200°C, as shown in Fig. 3-7.[20] In this case, the charge condition of such deeper states cannot be changed by bias sweeping in a standard *C*–*V* measurement. In addition, due to the exponentially increased time constants, only some electrons can be emitted from the interface states during the measurement duration, which is determined by the emission efficiency (η_e). Using the actual *C*–*V* measurement time (t_{meas}), the η_e is given by:

$$\eta_e = 1 - exp\left(-\frac{t_{meas}}{\tau}\right). \tag{3-5}$$

In the calculation, the resulting charge Q_{it} in the interface states at each gate bias can be estimated using η_e, D_{it} distributions, and the following equation:

$$Q_{it} = q\int_{E_V}^{E_C} D_{it}^{D}\left[1 - f_0\left(1-\eta_e\right) - \eta_e f\right]dE - q\int_{E_V}^{E_C} D_{it}^{A}\left[f_0\left(1-\eta_e\right) + \eta_e f\right]dE \ , \tag{3-6}$$

where f_0 and f are the Fermi–Dirac function at the start bias and at each bias, respectively. In Fig. 3-6 (b), E_{Tm} is the deepest energy of the state that can respond during t_{meas}. E_{Tm} can also be described by using SRH statistics as follows:

$$E_{Tm} = kT\,ln\left(\sigma N_C \upsilon t_{meas}\right). \tag{3-7}$$

Assuming that σ is 1×10^{-16} cm^2 and t_{meas} is 100 s, E_{Tm} was estimated to be 0.8 eV from the conduction-band edge in the Al_2O_3/AlGaN system. This means, therefore, that only 25% or less of the interface states can be detected while the others are in "frozen states" that cannot de-trap electrons during *C–V* sweeping at RT. As shown in Fig. 3-6 (a), the interface states led to on-set voltage shifts toward the positive direction and stretch-out of *C–V* curves in the positive bias range. This is due to the change of the interface state charge within the "effective states" when the Fermi level E_F is moving between the conduction-band edge E_C to E_{Tm}, as shown in Fig. 3-8 (b). In the negative bias range, in contrast, only parallel voltage shifts were observed. As shown in Fig. 3-8 (c), when E_F moves down toward the valence-band edge E_V at the Al_2O_3/AlGaN interface, the "frozen states" in the energy range of E_{Tm} to E_V cannot change their electron occupation rate because their corresponding time constants are longer than the sweeping time of 100 s. Because the interface charge density is not a function of the gate bias during the negative bias sweep, the interface states do not cause the stretch-out behavior. It follows, therefore, that the detection of the interface states using the standard *C–V* measurement in the negative bias region is difficult.

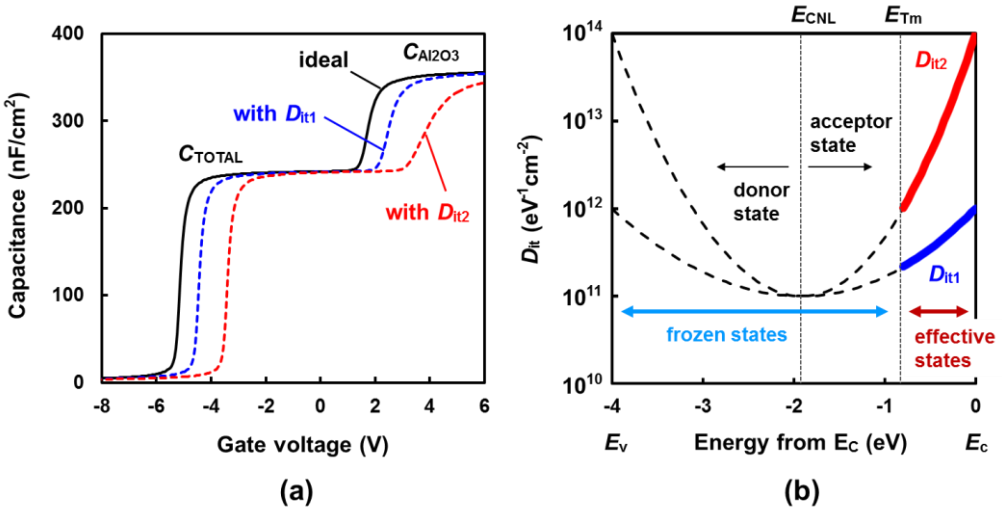

Fig. 3-6. (a) Calculated *C–V* characteristics of Al_2O_3/AlGaN/GaN structures. (b) Al_2O_3/AlGaN interface density distributions assumed in calculation.

Table 3-1. Parameters assumed in *C*–*V* calculation.

Parameter name	Value
Bandgap (eV)	3.4 (GaN) 4.0 (AlGaN) 6.7 (Al_2O_3)
Permittivity	9.5 (GaN) 9.25 (AlGaN) 8.5 (Al_2O_3)
Effective mass of electron	0.2 (GaN) 0.23 (AlGaN)
Effective mass of hole	0.8 (GaN, AlGaN)
Doping density (cm^{-3})	10^{15} (GaN, AlGaN)
Band offset (eV)	0.384 (AlGaN/GaN) 2.2 (Al_2O_3/AlGaN)
Surface barrier height (eV)	4.5 (Ni/Al_2O_3)
2DEG density (cm^{-3})	1.0×10^{13}
E_{CNL} (eV)	E_c -1.9
D_{it0} ($cm^{-2}eV^{-1}$)	1.0×10^{11}
E_{0A}	1.252119 (D_{it1}) 0.722911 (D_{it2})
n_A	2
E_{0D}	1.383921 (D_{it1}) 0.799007 (D_{it2})
n_D	2
σ (cm^2)	10^{-16} (Al_2O_3/AlGaN)
t_{meas}	100

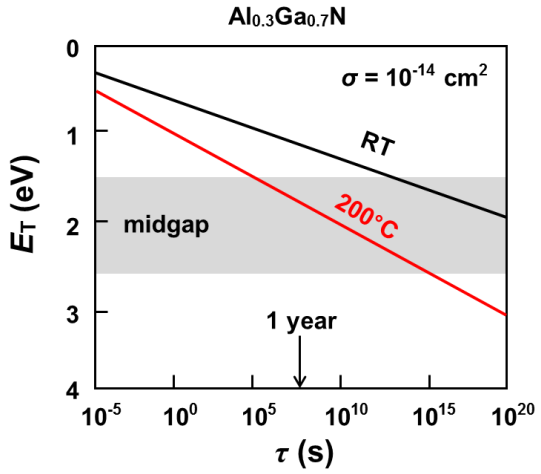

Fig. 3-7. Emission time constant τ at $Al_{0.3}Ga_{0.7}N$ bandgap as function of trap energy E_T, which is based on the Shockley-Read-Hall static model.[20)]

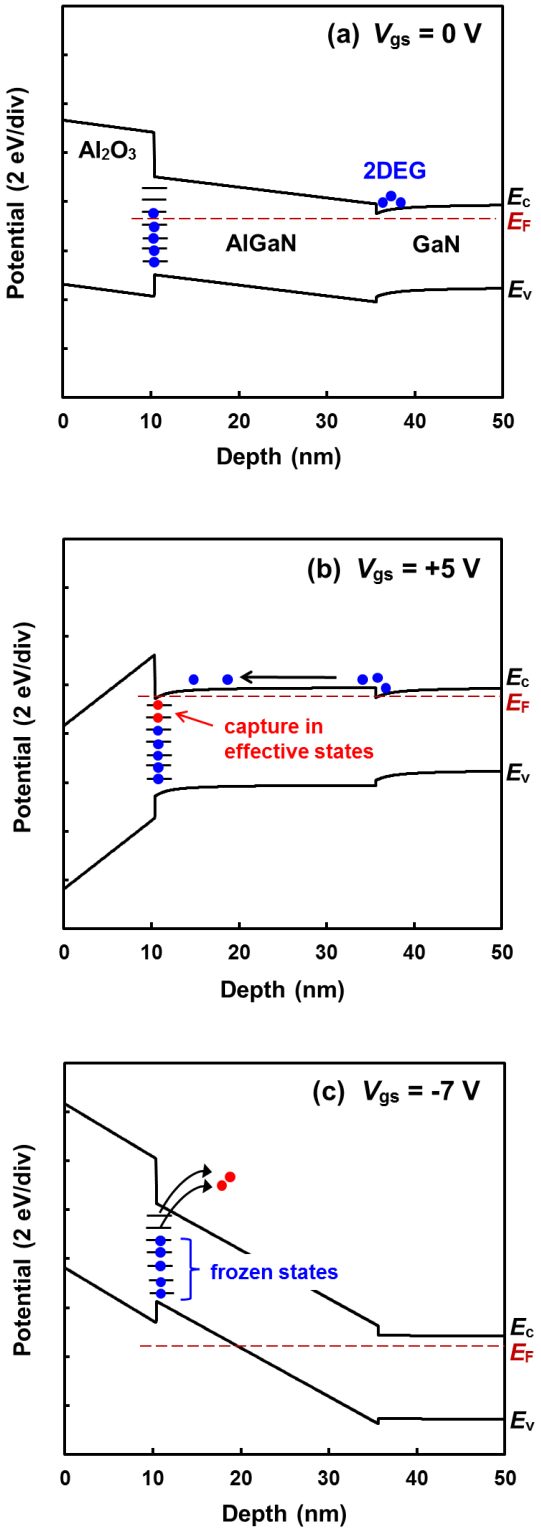

Fig. 3-8. Band diagrams of Al_2O_3/AlGaN/GaN structure at (a) V_{gs} = 0 V, (b) V_{gs} = +5 V, and (c) V_{gs} = -7 V.

3.3.2. Photo-assisted *C–V* measurement

To evaluate near-midgap electronic states at the insulator/barrier interface in insulated-gate GaN HEMTs, a photo-assisted *C–V* technique was developed by Mizue *et al*.[20] Figure 3-9 (a) shows schematic illustrations of the photoionization effects of interface states under a monochromatic light with energy less than the bandgap of GaN. First, under dark condition, a forward gate voltage high enough to observe the insulator capacitance is applied. At this state, almost all interface traps are filled with electrons under a nearly flat band condition. Then, the gate bias is swept toward a value more negative than the threshold voltage. After reaching a sufficiently negative gate bias, a monochromatic light with photon energy of $h\nu_1$ is illuminated on the sample surface. Consequently, we are effectively inducing photo-assisted electron emission from the interface states within the energy range corresponding to the photon energy range, as schematically shown in Fig. 3-9 (a). After switching the light off, we restarted the voltage sweep toward 0 V under dark condition. As shown in Fig. 3-9 (b), we can observe the *C–V* curve shift toward the reverse bias direction, corresponding to the change in the interface state charge Q_{it} ($h\nu_1$). Using different photon energies, we can induce a systematic *C–V* shift according to the photon energy, as shown in Fig. 3-9 (b). The ΔV_{th} between two photon energies corresponds to the interface charge difference, ΔQ_{it}, in the energy range $\Delta h\nu$ shown in Fig. 3-9 (c). The state density can be simply estimated using the observed ΔV_{th} in the following equation:

$$D_{it}\left(E = E_{AVG}\right) = \frac{C_{\mathrm{TOTAL}}}{q}\frac{\Delta V_{th}}{\Delta h\nu}, \tag{3-8}$$

where C_{TOTAL} is the total capacitance of Al_2O_3 and AlGaN, and E_{AVG} is the average interface energy schematically shown in Fig. 3-9 (c).

It should be emphasized that the present method uses incident photons with energies less than the bandgap of GaN. On the other hand, some groups have reported photo-assisted *C–V* characterization of MIS- and MOS-HEMTs using a light source with photon energies larger than the GaN bandgap.[22, 23] In this case, holes are generated and accumulated at the oxide/AlGaN and AlGaN/GaN interfaces. In addition, the interaction of holes with the interface states, especially at reverse bias, has to be considered. This makes the charge dynamics in MOS-HEMTs complicated and the evaluation of interface states very difficult. Matys *et al*. proposed a simulation method

for the photo-assisted *C*–*V* characteristics, taking into account the electron-hole generation and the recombination processes, as well as the hole capture process at the interface states.[24, 25] Comparing their calculation results to the experimental data, they were able to estimate the state density distribution at the Al_2O_3/AlGaN interface near the valence-band maximum of AlGaN.

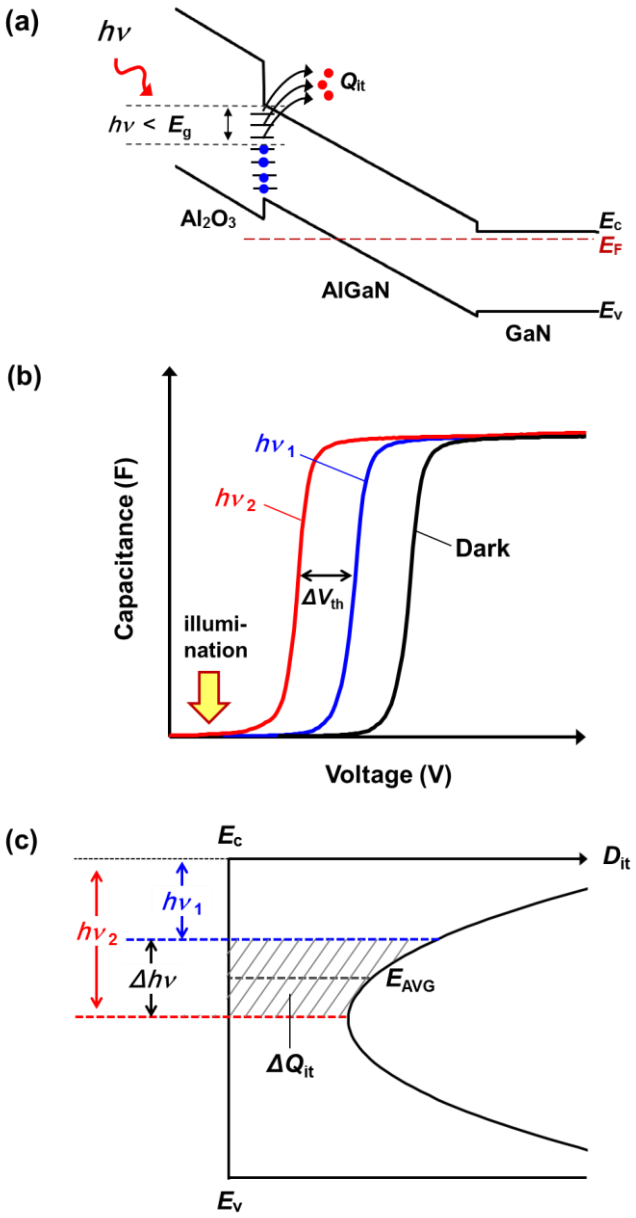

Fig. 3-9. Schematic illustration of (a) photo-assisted electron emission at Al_2O_3/AlGaN interface, (b) photo-assisted *C*–*V* characteristics, and (c) interface state charge and energy range corresponding to ΔV_{th}, in photo-assisted *C*–*V* curves.

3.4. Conclusion

This chapter described the origin and effects of the electronic states induced at the interface between insulators and GaN-based materials. The evaluation methods of the interface states were explained, focusing on the *C–V* characteristics of the MOS structures. In the case of wide bandgap semiconductors, not all the interface states can emit electrons due to the longer time constants compared to the actual *C–V* measurement time. Thus, photo-assisted *C–V* measurement is necessary to characterize the interface states near the midgap of GaN-based MOS-HEMTs. This technique is demonstrated for AlGaN and InAlN/GaN MOS-HEMTs in chapters 4 and 6, respectively.

References

1) H. Hasegawa and H. Ohno, J. Vac. Sci. Technol. B **4**, 1130 (1986).
2) J. Tersoff, Phys. Rev. Lett. **52**, 465 (1984).
3) M. Cardona and N. E. Christensen, Phys. Rev. B **35**, 6182 (1987).
4) W. Monch, J. Appl. Phys. **80**, 5076 (1996).
5) V. Heine, Phys. Rev. **138**, A1689 (1965).
6) T. Teraji and S. Hara, Phys. Rev. B **70**, 035312 (2004).
7) H. Hasegawa, T. Sato and C. Kaneshiro, J. Vac. Sci. Technol. B **17**, 1856 (1999).
8) T. Sato, S. Kasai and H. Hasegawa, Appl. Surf. Sci. **175/176**, 181 (2001).
9) H. Hasegawa, T. Sato and S. Kasai, Appl. Surf. Sci. **166**, 92 (2000).
10) W. E Spicer, I. Lindau, P. R. Skeath and C. Y. Su, J. Vac. Sci. Technol. **17**, 1019 (1980).
11) Y. Yuan, L. Wang, B. Yu, B. Shin, J. Ahn, P. C. McIntyre, P. M. Asbeck, M. J. W. Rodwell, and Y. Taur, IEEE Electron Device Lett. **32**, 485 (2011).
12) H.-P. Chen, Y. Yuan, B. Yu, J. Ahn, P. C. McIntyre, P. M. Asbeck, M. J. W. Rodwell, and Y. Taur, IEEE Trans. Electron Devices **59**, 2383 (2012).
13) G. Brammertz, A. Alian, D. H.-C. Lin, M. Meuris, M. Caymax, and W.-E. Wang, IEEE Trans. Electron. Devices **58**, 3890 (2011).
14) G. Jiao, C. Yao, Y. Xuan, D. Huang, P. D. Ye, and M.-F. Li, IEEE Trans. Electron Devices **59**, 1661 (2012).
15) R. V. Galatage, D. M. Zhernokletov, H. Dong, B. Brennan, C. L. Hinkle, R. M. Wallace, and E. M. Vogel, J. Appl. Phys. **116**, 014504 (2014).
16) R. V. Galatage, D. M. Zhernokletov, H. Dong, B. Brennan, C. L. Hinkle, R. M. Wallace, and E. M. Vogel, J. Appl. Phys. **116**, 014504 (2014).
17) Z. Yatabe, J. T. Asubar, and T. Hashizume, J. Appl. D **49**, 393001 (2016).
18) M. Choi, J. L. Lyons, A. Janotti, and C. G. Van de Walle, Phys. Status Solidi B **250**, 787 (2013).
19) M. Miczek, C. Mizue, T. Hashizume, and B. Adamowicz: J. Appl. Phys. **103**, 104510 (2008).
20) C. Mizue, Y. Hori, M. Miczek, and T. Hashizume, Jpn. J. Appl. Phys. **50**, 021001 (2011).
21) Z. Yatabe, Y. Hori, W. Ma, J. T. Asubar, M. Akazawa, T. Sato, and T. Hashizume: Jpn. J. Appl. Phys. **53**, 100213 (2014).
22) R. Yeluri, B. L. Swenson, and U. K. Mishra, J. Appl. Phys. **111**, 043718 (2012).
23) M. Fagerlind and N. Rorsman, J. Appl. Phys. **112**, 014511 (2012).

24) M. Matys, B. Adamowicz, and T. Hashizume, Appl. Phys. Lett. **101**, 231608 (2012).
25) M. Matys, B. Adamowicz, Y. Hori, and T. Hashizume, Appl. Phys. Lett. **103**, 021603 (2013).

Chapter 4

Reduction in threshold voltage shift of AlGaN/GaN MOS-HEMTs by controlling oxidant source for ALD-Al_2O_3

4.1. Introduction

As described above, GaN high electron mobility transistors (HEMTs) have demonstrated good performance in high power applications, such as power amplifiers in wireless base stations and rader systems.[1, 2)] The primary requirement for high power devices is a low gate leakage current for high power operation and high reliability. Over the past few years, several groups have attempted to suppress the gate leakage current using metal-insulator-semiconductor (MIS), and/or metal-oxide-semiconductor (MOS) structures. Among the various insulator films that have been employed in AlGaN/GaN MOS-HEMTs, Al_2O_3 is one of the most attractive ones because of its wide band gap (~7.0 eV), high dielectric constant (~9.0), and high breakdown voltage (~10 MV/cm).[3-6)] Furthermore, the Al_2O_3 films must be kept thin to suppress the degradation of radio frequency (RF) performance due to the decrease in transconductance (g_m). Thus, the atomic layer deposited (ALD)-Al_2O_3 is desirable for AlGaN/GaN MOS-HEMTs in terms of controllability for Al_2O_3 thickness. On the other hand, threshold voltage (V_{th}) shift of AlGaN/GaN MOS-HEMTs was reported when using ALD-Al_2O_3.[7-8)] It is considered that the V_{th} shift occurred due to an electron trap in AlGaN/GaN MOS-HEMTs during a positive gate-voltage (V_{gs}) sweep, and this causes the degradation in operation stability. Therefore, the V_{th} shift is one of the critical issues to be solved for power applications. However, the mechanism has not been yet confirmed. One of the possible origins for the V_{th} shift is impurities such as OH residues [$Al(OH)_x$] that are attributed to the oxidant source remaining in ALD-Al_2O_3, and they may function as electron traps. On the other hand, several studies have reported that the nonstoichiometric gallium oxide (GaO_x) functions as electron traps at the Al_2O_3/GaN interface.[9)]

In this chapter, we have investigated the mechanism for the V_{th} shift of Al_2O_3/AlGaN/GaN MOS-HEMTs by focusing on $Al(OH)_x$ in ALD-Al_2O_3 and GaN oxidation at the Al_2O_3/GaN interface. Furthermore, we demonstrated the reductions in the V_{th} shift and the gate leakage current by controlling the oxidant sources for the ALD method.

4.2. Experimental Procedure

We have fabricated AlGaN/GaN MOS-HEMTs as shown in Fig. 4-1.[10] The gate length, gate width, and gate-drain length were 1, 50, and 10 μm, respectively. A 40-nm-thick Al_2O_3 film was deposited on the AlGaN/GaN HEMT epitaxial structure (n-GaN/n-AlGaN/GaN/buffer/substrate) by using the ALD method at 350°C. Trimethylaluminum (TMA) was used as the aluminum source, and O_2 plasma and H_2O vapor were used as the oxidant sources to investigate the GaN oxidation at the Al_2O_3/GaN interface. Al_2O_3 films were formed by the following reactions:[11, 12]

$$2Al(CH_3)_3 + 4O_2 \rightarrow Al_2O_3 + 2CO_2 + 4CH_4 + H_2O, \quad (4\text{-}1)$$

$$2Al(CH_3)_3 + 3H_2O \rightarrow Al_2O_3 + 6CH_4. \quad (4\text{-}2)$$

After deposition, post-deposition annealing (PDA) in N_2 atmosphere was performed to decrease the amount of $Al(OH)_x$ for 1 min at 700°C and 800°C. Annealing temperatures were determined by H_2O thermal desorption spectroscopy (TDS) of the as-deposited ALD-Al_2O_3 due to following $Al(OH)_x$ dehydration. [13–17]

$$2AlOH \rightarrow Al_2O_3 + H_2O. \quad (4\text{-}3)$$

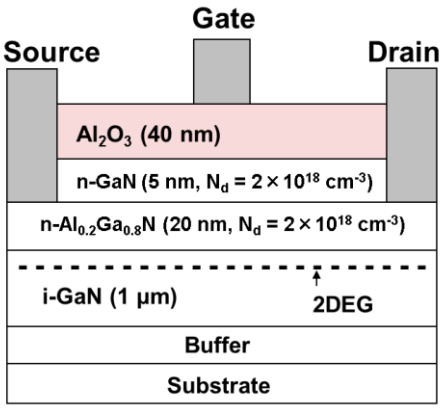

Fig. 4-1. Schematic cross-sectional view of AlGaN/GaN MOS-HEMTs used in this work (Reproduced from ref. 10, copyright 2013 by the Japan Society of Applied Physics).

X-ray photoelectron spectroscopy (XPS) was used to analyze the $Al(OH)_x$ in ALD-Al_2O_3, and the GaN oxidation at the Al_2O_3/GaN interface by using those test pieces for analysis that had the same structure as devices (Al_2O_3/n-GaN/n-AlGaN/GaN/buffer/substrate). Furthermore, the depth of GaN oxidation was estimated from the oxygen-concentration (O-concentration) of GaN layer that was evaluated by the chemical composition analysis. To prevent the GaN surface from exposed to the air, we removed the Al_2O_3 films in XPS chamber by argon ion sputtering.

After device fabrication, V_{th} shift was evaluated by capacitance–voltage (C–V) measurement at 100 kHz. The gate bias was swept from forward (-20 to 10 V) to reverse (10 to -20 V) in the dark, and the V_{th} shift was estimated from the hysteresis width. After that, the trap level which determines the V_{th} shift was evaluated by photo-assisted C–V measurement to investigate the effect of captured electrons as shown in Fig. 4-2.[10] The V_{th} shift (ΔV_{th}) with light irradiation was estimated from the comparison of the C–V curves between before (dark) and after light condition (light). Light irradiation was conducted by halogen lamp which has broadband wavelength (380–900 nm). Negative V_{gs} of -20 V was applied for 10 minutes under light irradiation, and the V_{gs} was swept from -20 V to 10 V at 100 kHz. To estimate the trap level from the conduction band edge (E_c), the photon energy was changed from 1.38 to 3.26 eV by using a band pass filter. Furthermore, the drain-to-source current versus gate-to-source voltage (I_{ds}–V_{gs}) and the gate-current versus gate-to-source voltage (I_g–V_{gs}) characteristics were measured at the drain-to-source voltage (V_{ds}) of 10 V. The V_{gs} was swept from forward (-20 to 10 V) to reverse (10 to -20 V) in the dark, and the V_{th} shift was estimated from the hysteresis of I_{ds}–V_{gs} curves.

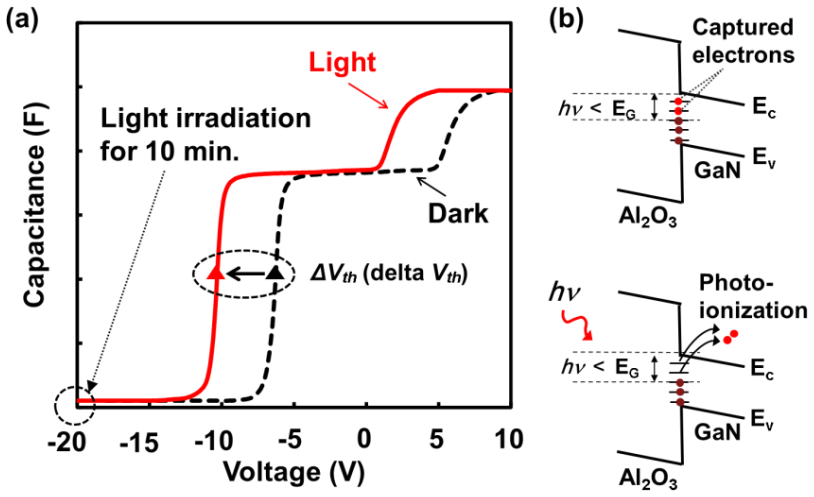

Fig. 4-2. (a) *C–V* curves of AlGaN/GaN MOS-HEMTs obtained at before and after light irradiation. (b) Schematic illustrations for photo-ionization of captured electrons under light irradiation (Reproduced from ref. 10, copyright 2013 by the Japan Society of Applied Physics).

4.3. Results and Discussion

4.3.1. Mechanism for V_{th} shift of Al_2O_3/AlGaN/GaN MOS-HEMTs

The relationship between the oxidant source and the V_{th} shift is shown in Fig. 4-3.[18] The V_{th} shift of O_2 plasma-Al_2O_3 was larger than that of H_2O vapor-Al_2O_3. By increasing PDA temperature, the V_{th} shift could be reduced for both oxidant sources. To investigate the mechanism of the V_{th} shift, we measured the $Al(OH)_x$ concentration in ALD-Al_2O_3 by XPS. Figure 4-4 shows the O 1s spectrum of the as-deposited Al_2O_3.[18] Sapphire was used as a standard reference sample. The O 1s spectrum of ALD-Al_2O_3 was different from an ideal Al_2O_3 spectrum due to $Al(OH)_x$ residues. Furthermore, H_2O thermal desorption due to $Al(OH)_x$ dehydration was observed in ALD-Al_2O_3 as shown in Fig. 4-5.[18] Thus, Figures 4-4 and 4-5 indicate that $Al(OH)_x$ was formed in ALD-Al_2O_3 for both oxidant source cases.

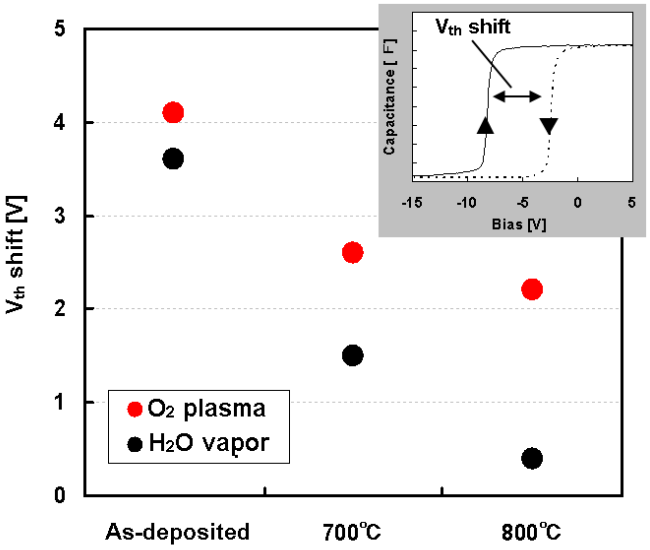

Fig. 4-3. Variation in V_{th} shift with oxidant source and PDA temperature. Upper right inset shows the *C*–*V* profile to estimate V_{th} shift (Reproduced from ref. 18, with the permission of CS-MANTECH).

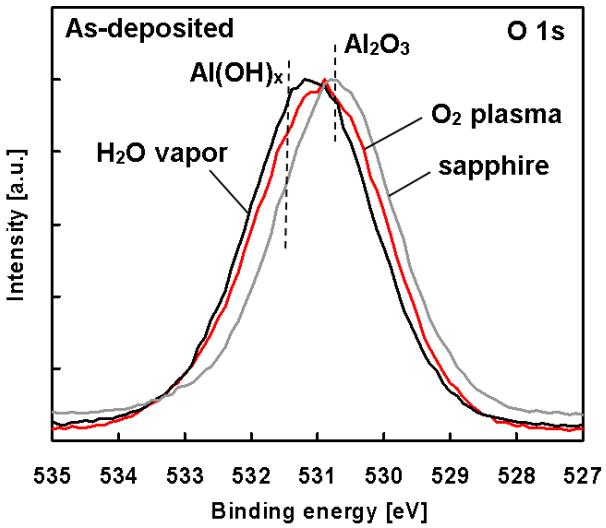

Fig. 4-4. O 1s spectrum of as-deposited H_2O vapor and O_2 plasma-Al_2O_3 measured by XPS (Reproduced from ref. 18, with the permission of CS-MANTECH).

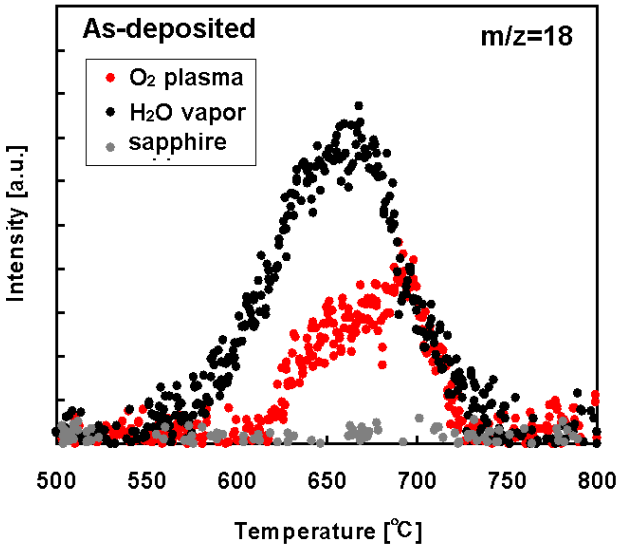

Fig. 4-5. H_2O thermal desorption spectrum of as-deposited H_2O vapor and O_2 plasma-Al_2O_3 measured by TDS (Reproduced from ref. 18, with the permission of CS-MANTECH).

Figure 4-6 shows the effect of PDA on the V_{th} shift and the $Al(OH)_x$ concentration,[18] which was calculated by waveform analysis of separating the O 1s spectrum into Al_2O_3 (530.7 eV) and $Al(OH)_x$ (531.33 eV).[19] We found that the $Al(OH)_x$ concentration was decreased by increasing PDA temperature. It was confirmed that the V_{th} shift was reduced corresponding to decreasing the $Al(OH)_x$ concentration, suggesting that the V_{th} shift was attributed to $Al(OH)_x$ in ALD-Al_2O_3. On the other hand, the V_{th} shift of O_2 plasma-Al_2O_3 was larger than that of H_2O vapor-Al_2O_3 at the same $Al(OH)_x$ concentration. Moreover, the difference in the V_{th} shift was remarkable at low $Al(OH)_x$ concentrations when PDA was applied at 800°C. Therefore, another origin of the V_{th} shift, in addition to $Al(OH)_x$ effect, should be considered, focusing on the effect of the oxidant source. A possible hypothesis is that GaN oxidation at the Al_2O_3/GaN interface was promoted by O_2 plasma because of its high reactivity.

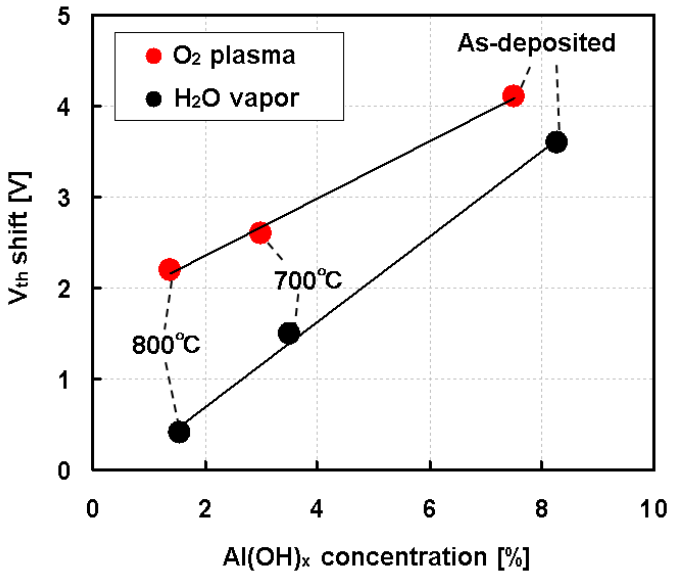

Fig. 4-6. $Al(OH)_x$ concentration dependence on V_{th} shift for H_2O vapor and O_2 plasma-Al_2O_3. PDA temperature was varied (Reproduced from ref. 18, with the permission of CS-MANTECH).

To verify the effect of the oxidant source on GaN oxidation at the Al_2O_3/GaN interface, we measured Ga 3d spectrum on very thin 2-nm-thick ALD-Al_2O_3 deposited on GaN. 800°C PDA was applied after Al_2O_3 deposition. GaO_x concentration was calculated by waveform analysis of separating the Ga 3d spectrum into GaN (19.7 eV) and GaO_x (20.8 eV).[20] Figure 4-7 shows the Ga 3d spectrum at the Al_2O_3/GaN interface.[18] The Ga 3d spectrum of O_2 plasma-Al_2O_3 was shifted to higher binding energy relative to H_2O vapor-Al_2O_3. Figure 4-8 shows the GaO_x concentrations for H_2O vapor and O_2 plasma, respectively.[18] From these results, it was confirmed that the GaO_x concentration of O_2 plasma-Al_2O_3 was higher than that of H_2O vapor-Al_2O_3, as we had expected.

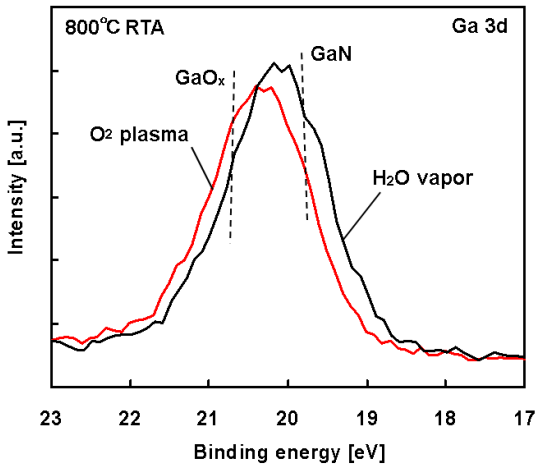

Fig. 4-7. Ga 3d spectrum at Al_2O_3/GaN interface for H_2O vapor and O_2 plasma-Al_2O_3 measured by XPS. 800°C PDA was applied in this figure case (Reproduced from ref. 18, with the permission of CS-MANTECH).

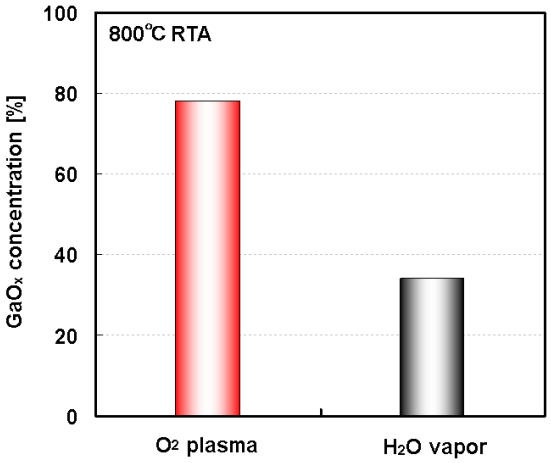

Fig. 4-8. Comparison of GaO_x concentration between O_2 plasma and H_2O vapor-Al_2O_3. 800°C PDA was applied in this figure case (Reproduced from ref. 18, with the permission of CS-MANTECH).

Furthermore, the depth of GaN oxidation was estimated from the oxygen-concentration (O-concentration) of GaN layer that was evaluated by the chemical composition analysis. To prevent the GaN surface from exposed to the air, we removed the Al_2O_3 films in XPS chamber by argon ion sputtering. Figure 4-9 shows the depth profile of GaN oxidation at the Al_2O_3/GaN interface.[10] O_2 plasma-Al_2O_3 had larger oxygen-concentration than H_2O vapor-Al_2O_3 at each depth. So, it was confirmed that GaN oxidation was promoted by O_2 plasma, and its depth extended about 4 nm from the Al_2O_3/GaN interface. We believe that active oxygen, such as radicals and ions, which were generated by O_2 plasma, accelerated the GaN oxidation at the Al_2O_3/GaN interface because of its high reactivity. These results indicate that GaN oxidation at the Al_2O_3/GaN interface also caused the V_{th} shift, in addition to $Al(OH)_x$ in ALD-Al_2O_3.

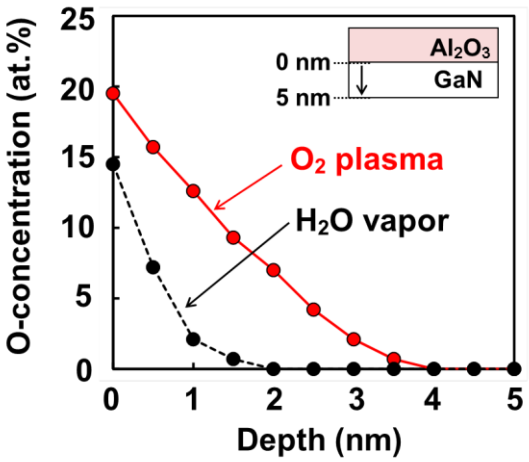

Fig. 4-9. Depth profile of GaN oxidation at Al_2O_3/GaN interface for O_2 plasma-Al_2O_3 and H_2O vapor-Al_2O_3 measured by XPS (Reproduced from ref. 10, copyright 2013 by the Japan Society of Applied Physics).

To investigate the effect of GaN oxidation at the Al_2O_3/GaN interface on the I_{ds}–V_{gs} characteristics, we have fabricated two kinds of AlGaN/GaN MOS-HEMTs using H_2O vapor and O_2 plasma-Al_2O_3 for the gate insulator films as shown in Fig. 4-1. Focusing on the electron trap at the Al_2O_3/GaN interface, we applied 800°C PDA to reduce the amount of $Al(OH)_x$ in ALD-Al_2O_3. Figure 4-10 shows the I_{ds}–V_{gs} curves, which were measured at the V_{ds} of 10 V.[18] The gate bias was swept from forward (-20 to 10 V) to reverse (10 to -20 V) in the dark, and the V_{th} shift was estimated from the hysteresis of I_{ds}–V_{gs} curves. When PDA temperature was varied, it was confirmed that AlGaN/GaN

MOS-HEMT with H_2O vapor-Al_2O_3, which was applied 800°C PDA showed the smallest V_{th} shift. This trend was in agreement with the results of *C*–*V* measurement as shown in Fig. 4-6. On the other hand, as shown in Fig. 4-10, V_{th} which was defined from the forward sweep curve of O_2 plasma-Al_2O_3 was larger than that of H_2O vapor-Al_2O_3. We have already reported that the reversible change in V_{th} was caused by the captured electrons in the deep level, which might exist at the Al_2O_3/GaN interface, and the captured electrons could be released to the 2DEG due to negative gate bias stress.[8)] Therefore, if electrons were captured in the oxidized GaN layer at the Al_2O_3/GaN interface, it was concerned that V_{th} shifted positive value from the veritable V_{th}.

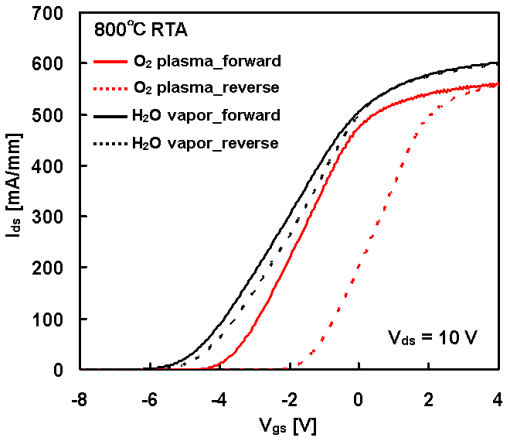

Fig. 4-10. I_{ds}–V_{gs} curves for AlGaN/GaN MOS-HEMTs using H_2O vapor and O_2 plasma-Al_2O_3 for gate insulator films. 800°C PDA was applied in this figure case (Reproduced from ref. 18, with the permission of CS-MANTECH).

Then, to investigate the effect of captured electrons at the Al_2O_3/GaN interface on the V_{th} shift, we evaluated the trap level of AlGaN/GaN MOS-HEMTs by photo-assisted *C*–*V* measurement. Figures 4-11 (a) and (b) show the *C*–*V* curves of AlGaN/GaN MOS-HEMTs when using O_2 plasma and H_2O vapor, respectively.[10)] The V_{th} shift with light irradiation was estimated from the comparison of the *C*–*V* curves between the dark and the light condition. In this case, the photon energy was applied at 3.26 eV without a band pass filter. As shown in Fig. 4-11, the V_{th} shift of O_2 plasma-Al_2O_3 was larger than that of H_2O vapor-Al_2O_3. From these results, it is considered that the V_{th} shift with light irradiation occurred due to the electron trap in the oxidized-GaN layer at the Al_2O_3/GaN interface which was confirmed by XPS measurement, when using O_2 plasma.

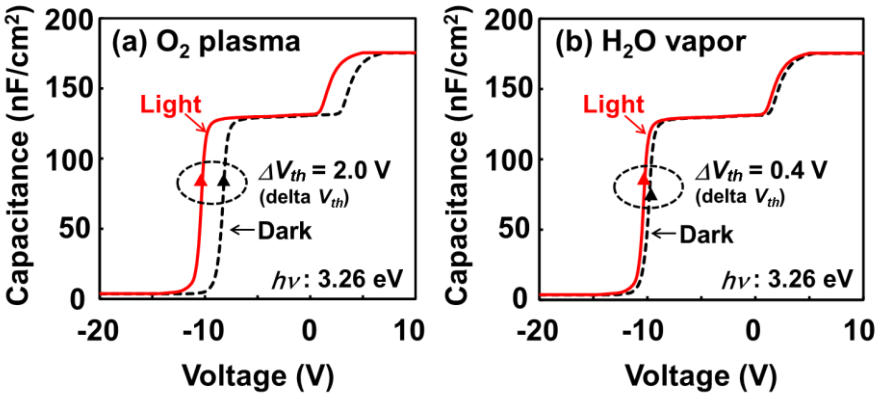

Fig. 4-11. *C–V* curves of AlGaN/GaN MOS-HEMTs obtained before and after light irradiation when using (a) O_2 plasma-Al_2O_3 and (b) H_2O vapor-Al_2O_3. Photon energy was applied at 3.26 eV (Reproduced from ref. 10, copyright 2013 by the Japan Society of Applied Physics).

To estimate the trap level from the conduction band edge, we changed the photon energy from 1.38 to 3.26 eV by using a band pass filter. Figure 4-12 shows the relationship between the wavelength and the V_{th} shift.[10)] As shown in Fig. 4-12, the V_{th} shift with light irradiation of O_2 plasma-Al_2O_3 was larger than that of H_2O vapor-Al_2O_3 at each wavelength between 380 and 480 nm. Therefore, it is considered that the deep trap sites which were located around 2.58–3.26 eV from the conduction band edge were attributed to GaN oxidation due to O_2 plasma. Moreover, according to previous studies,[21–26)] vacancy-type defects such as nitrogen vacancy (V_N) and gallium vacancy (V_{Ga}) are located around 0.24 and 2.62 eV from the conduction band edge, respectively. Furthermore, oxygen at a nitrogen site (O_N) and its complex with V_{Ga} (V_{Ga}-O_N) are located around 0.5 and 2.3-3.3 eV from the conduction band edge, respectively. So, the deep trap sites due to GaN oxidation when using O_2 plasma were possibly attributed to vacancy-type defects such as V_{Ga} and V_{Ga}-O_N.

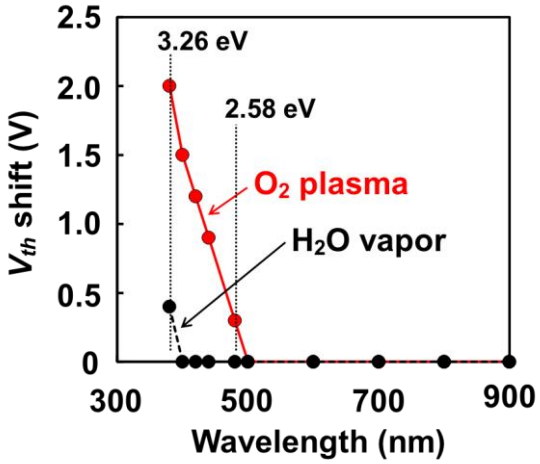

Fig. 4-12. Relationship between wavelength and V_{th} shift of AlGaN/GaN MOS-HEMT measured by photo-assisted *C*–*V* measurement (Reproduced from ref. 10, copyright 2013 by the Japan Society of Applied Physics).

Figure 4-13 shows our proposed mechanism for the V_{th} shift due to GaN oxidation when using O_2 plasma.[10] We clarified in our study that GaN oxidation was promoted by O_2 plasma, and oxidized-GaN layer was formed at the Al_2O_3/GaN interface. Furthermore, we confirmed that the V_{th} shift with light irradiation occurred when the photon energy was applied at 2.58–3.26 eV. From these results, it is considered that the deep trap sites were generated in oxidized-GaN layer because of plasma-induced damages, and this caused the V_{th} shift when using O_2 plasma. Consequently, it is indispensable to suppress GaN oxidation at the Al_2O_3/GaN interface when using O_2 plasma. On the other hands, H_2O vapor-Al_2O_3 has more leaky characteristics than O_2 plasma-Al_2O_3 because of a lower dielectric constant and mass density.[27–31] Therefore, we proposed novel hybrid-Al_2O_3 structure for the gate insulator.

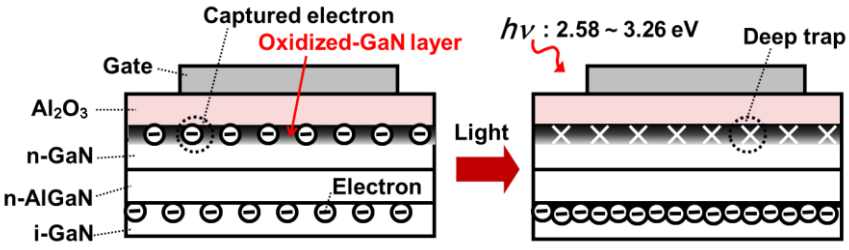

Fig. 4-13. Schematic cross-sectional view of proposed mechanism for V_{th} shift of AlGaN/GaN MOS-HEMT due to GaN oxidation when using O_2 plasma-Al_2O_3 (Reproduced from ref. 10, copyright 2013 by the Japan Society of Applied Physics).

4.3.2. Reduction in V_{th} shift and gate leakage current with hybrid-Al_2O_3 structure

To reduce the V_{th} shift and the gate leakage current of AlGaN/GaN MOS-HEMTs, we applied hybrid-Al_2O_3 structure (lower H_2O vapor-Al_2O_3/upper O_2 plasma-Al_2O_3) as shown in Fig. 4-14.[10] The concept of this structure is reducing the V_{th} shift due to GaN oxidation that was extended by about 4 nm from the Al_2O_3/GaN interface when using O_2 plasma. So, we inserted a 5 nm-thick H_2O vapor-Al_2O_3 between GaN and O_2 plasma-Al_2O_3. To compare the DC characteristics with the conventional structure, the total thickness of ALD-Al_2O_3 was fixed at 40 nm. Other fabrication processes were the same as those for the conventional structure.

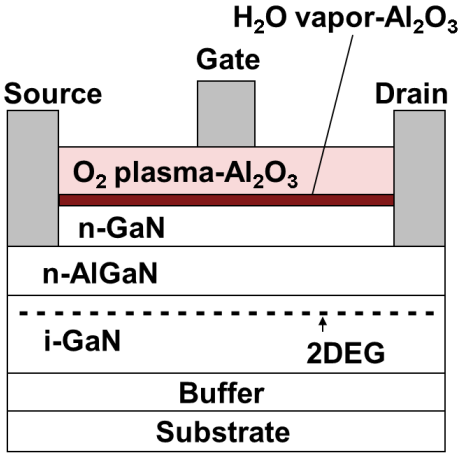

Fig. 4-14. Schematic cross-sectional view of AlGaN/GaN MOS-HEMTs using hybrid-Al_2O_3 structure (Reproduced from ref. 10, copyright 2013 by the Japan Society of Applied Physics).

After the device fabrication, I_{ds}–V_{gs} and I_g–V_{gs} characteristics were measured at the V_{ds} of 10 V. The V_{gs} was swept from forward (-20 to 10 V) to reverse (10 to -20 V) in the dark, and the V_{th} shift was estimated from the hysteresis of I_{ds}–V_{gs} curves. Figures 4-15 show I_{ds}–V_{gs} (a) and I_g–V_{gs} (b) characteristics of AlGaN/GaN MOS-HEMTs when using O_2 plasma-Al_2O_3, H_2O vapor-Al_2O_3, and hybrid-Al_2O_3.[10] As shown in Fig. 4-15

(a), the V_{th} shift of O_2 plasma-Al_2O_3 was larger than that of H_2O vapor-Al_2O_3. This trend was in agreement with the results of photo-assisted *C*–*V* measurement as shown in Figs. 4-11 and 4-12. On the other hand, by applying hybrid-Al_2O_3 structure, the V_{th} shift was successfully reduced to 0.25 V, same as H_2O vapor-Al_2O_3. Therefore, it was revealed that suppressing GaN oxidation at the Al_2O_3/GaN interface by controlling the initial oxidant source is effective to reduce the V_{th} shift when using O_2 plasma. Furthermore, as shown in Fig. 4-15 (b), the gate leakage current of hybrid-Al_2O_3 was 3 orders of magnitude lower than that of H_2O vapor-Al_2O_3 at V_{gs} of 20 V. Thus, in addition to the reduction in the V_{th} shift, the gate leakage current was successfully reduced to the same as O_2 plasma-Al_2O_3 by applying hybrid-Al_2O_3 structure.

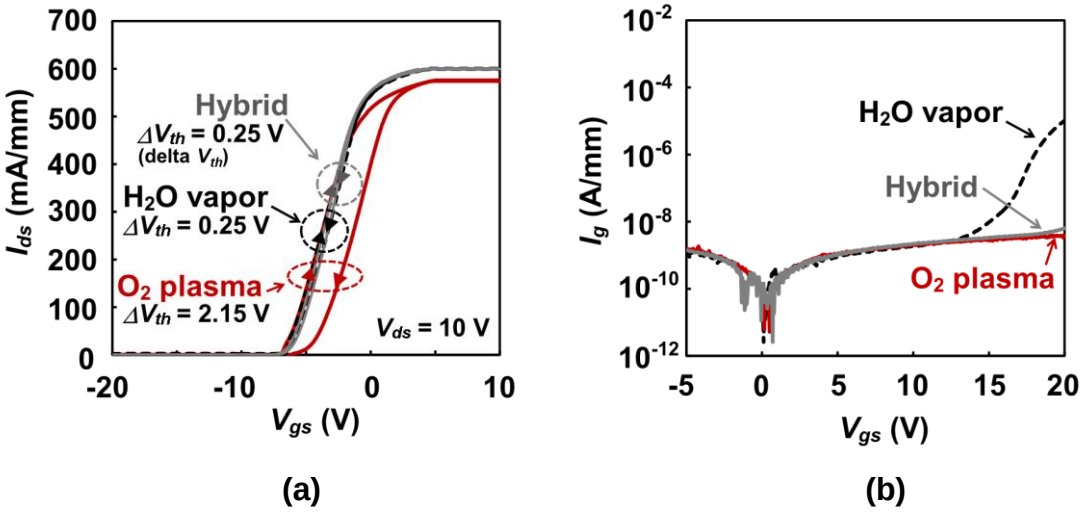

Fig. 4-15. (a) I_{ds}–V_{gs} and (b) I_g–V_{gs} characteristics of AlGaN/GaN MOS-HEMTs using O_2 plasma-Al_2O_3, H_2O vapor-Al_2O_3, and hybrid-Al_2O_3 (Reproduced from ref. 10, copyright 2013 by the Japan Society of Applied Physics).

4.4. Conclusion

We have investigated the V_{th} shift of AlGaN/GaN MOS-HEMTs when using ALD-Al_2O_3 for the gate insulator films. As an oxidant source for ALD-Al_2O_3, H_2O vapor and O_2 plasma were compared, focusing on the V_{th} shift, which was evaluated by *C–V* hysteresis. As a result, we found that both $Al(OH)_x$ residues in ALD-Al_2O_3 and GaN oxidation layer at the Al_2O_3/GaN interface affected the V_{th} shift. By increasing PDA temperature, the $Al(OH)_x$ concentration could be decreased, suppressing the V_{th} shift. On the other hand, GaN oxidation layer at the Al_2O_3/GaN interface was promoted by O_2 plasma and the V_{th} shift of O_2 plasma-Al_2O_3 was larger than that of H_2O vapor-Al_2O_3. In addition, photo-assisted *C–V* measurement revealed that the deep trap sites which were located around 2.58–3.26 eV from the conduction band edge were generated in the oxidized-GaN layer at the Al_2O_3/GaN interface due to plasma-induced damages, and this caused the V_{th} shift when using O_2 plasma. From the I_{ds}–V_{gs} characteristics, we confirmed that AlGaN/GaN MOS-HEMT with H_2O vapor-Al_2O_3, which was annealed at high temperature, showed the smallest V_{th} shift. However, H_2O vapor-Al_2O_3 has more leaky characteristics than O_2 plasma-Al_2O_3 because of a lower dielectric constant and mass density. Thus, we controlled the oxidant source, and demonstrated the reductions in the V_{th} shift and the gate leakage current by applying hybrid-Al_2O_3 structure (lower H_2O vapor-Al_2O_3/upper O_2 plasma-Al_2O_3) for AlGaN/GaN MOS-HEMTs. The obtained results indicate that the controlling the oxidant source is key role in improving performance and operation stability of AlGaN/GaN MOS-HEMTs using ALD-Al_2O_3.

References

1) T. Kikkawa, Jpn. J. Appl. Phys. **44**, 4846 (2005).
2) T. Kikkawa, K. Makiyama, T. Ohki, M. Kanamura, K. Imanishi, N. Hara, and K. Joshin, Phys. Status Solidi A **206**, 1135 (2009).
3) Z. H. Liu, G. I. Ng, S. Arulkumaran, Y. K. T. Maung, K. L. Teo, S. C. Foo, and S. Vicknesh, Proc. European Microwave Integrated Circuits Conf., 41 (2010).
4) P. D. Ye, B. Yang, K. K. Ng, J. Bude, G. D. Wilk, S. Halder, and J. C. M. Hwang, Appl. Phys. Lett. **86**, 063501 (2005).
5) P. D. Ye, B. Yang, K. K. Ng, J. Bude, G. D. Wilk, S. Halder, and J. C. M. Hwang, Int. J. High Speed Electron. Syst. **14**, 791 (2004).
6) F. Medjdoub, N. Sarazin, M. Tordjman, M. Magis, M. A. di Forte-Poisson, M. Knez, E. Delos, C. Gaquiere, S. L. Delage, and E. Kohn, Elentron. Lett. **43**, 691 (2007).
7) C. Mizue, Y. Hori, M. Miczek, and T. Hashizume: Jpn, J. Appl. Phys. **50**, 021001 (2011).
8) T. Imada, K. Motoyoshi, M. Kanamura, and T. Kikkawa, IEEE Integrated Reliability Workshop Final Report, 38 (2011).
9) N. Nepal, N. Y. Garces, D. J. Meyer, J. K. Hite, M. A. Mastro, and C. R. Eddy, Jr., Appl. Phys. Express **4**, 055802 (2011).
10) S. Ozaki, T. Ohki, M. Kanamura, N. Okamoto, and T. Kikkawa, Jpn. J. Appl. Phys. **52**, 11NG04 (2013).
11) X. Li, Q. Chen, L. Sang, L. Yang, Z. Liu, and Z. Wang, Phys. Procedia **18**, 100 (2011).
12) J. Kim, K. Chakrabarti, J. Lee, K. Y. Oh, and C. Lee, Mater. Chem. Phys. **78**, 733 (2003).
13) A. W. Ott, J. W. Klaus, J. M. Johnson, and S. M. George, Thin Solid Films **292**, 135 (1997).
14) L. G. Gosset, J. F. Damlencourt, O. Renault, D. Rouchon, Ph. Holliger, A. Ermolieff, I. Trimaille, J. J. Ganem, F. Martin, and M. N. Semeria, J. Non-Cryst. Solids **303**, 17 (2002).
15) G. Catana, W. Griinert, P. Van Der Voort, E. F. Vansant, R. A. Schoonheydt, and B. M. Weckhuysen, J. Phys. Chem. B **104**, 9195 (2000).
16) R. L. Puurunen, J. Appl. Phys. **97**, 121301 (2005).
17) U. Das, and K. Raghavachari, J. Chem. Phys. **124**, 021101 (2006).
18) S. Ozaki, T. Ohki, M. Kanamura, T. Imada, N. Nakamura, N. Okamoto, T.

Miyajima, and T. Kikkawa, CS-MANTECH Tech. Dig., 311 (2012).
19) D. E. Passoja et al., J. Vac. Sci. Technol. **21**, 933 (1982).
20) S. D. Wolter et al., Thin Solid Films **371**, 153 (2000).
21) A. Arehart, A. Corrion, C. Poblenz, J. S. Speck, U. K. Mishra, and S. A. Ringel, Appl. Phys. Lett. **93**, 112101 (2008).
22) D. Johnstone: Proc. SPIE 6473, 64730L (2007).
23) J. Elsner, R. Jones, M. I. Heggie, P. K. Sitch, M. Haugk, T. Frauenheim, S. Oberg, and P. R. Briddon, Phys. Rev. B **58**, 12571 (1998).
24) S. J. Chua, H. W. Choi, J. Zhang, and P. Li, Phys. Rev. B **64**, 205302 (2001).
25) S. Limpijumnong, and C. G. Van de Walle, Phys. Rev. B **69**, 035207 (2004).
26) Y. S. Puzyrew, T. Roy, M. Beck, B. R. Tuttle, R. D. Schrimpf, D. M. Fleetwood, and S. T. Pantelides, J. Appl. Phys. **109**, 034501 (2011).
27) J. L. van Hemmen, S. B. S. Heil, J. H. Klootwijk, F. Roozeboom, C. J. Hodson, M. C. M. van de Sanden, and W. M. M. Kessels, J. Electrochem. Soc. **154**, 165 (2007).
28) S. E. Potts, G. Dingemans, C. Lachaud, and W. M. M. Kessels, J. Vac. Sci. Technol. A **30**, 021505 (2012).
29) G. Dingemans, M. C. M. van de Sanden, and W. M. M. Kessels, Electrochem. Solid-State Lett. **13**, H76 (2010).
30) H. B. Profijt, S. E. Potts, M. C. M. van de Sanden, and W. M. M. Kessels, J. Vac. Sci. Technol. A **29**, 050801 (2011).
31) K. B. Jinesh, J. L. van Hemmen, M. C. M. van de Sanden, F. Roozeboom, J. H. Klootwijk, W. F. A. Besling, and W. M. M. Kessels, J. Electrochem. Soc. **158**, G21 (2011).

Chapter 5

Effect of surface-oxide-control for InAlN barrier layers on gate leakage current and current collapse of InAlN/GaN MOS-HEMTs

5.1. Introduction

As already discussed previously in this thesis, GaN high electron mobility transistors (HEMTs) have performed quite well in high power applications, such as power amplifiers in wireless base stations, radar systems and millimeter-wave communications.[1-5] The primary requirement for power amplifiers is a large drain current for achieving a high level of power and efficiency. Especially, GaN-HEMTs using an InAlN electron-supplying layer are promising because of their high spontaneous polarization for enhancing two-dimensional electron gas (2DEG).[6] However, a large gate leakage current of InAlN/GaN HEMTs often limits their operation. Several methods have been reported to reduce the gate leakage current using metal-oxide-semiconductor (MOS) structures by the thermal oxidation and plasma treatment of oxygen.[7, 8] The oxide on the surface of InAlN (surface-oxide) is comprised of aluminum oxide (Al_2O_3) and indium oxide (In_2O_3).[9] However, the bandgap of In_2O_3 (~3.4 eV) is lower than that of Al_2O_3 (~7.0 eV). Therefore, the amount of In_2O_3 for the surface-oxide must be decreased to reduce the gate leakage current of InAlN/GaN MOS-HEMTs. In this chapter, we proposed water (H_2O) vapor oxidation to decrease In_2O_3 for the surface-oxide by focusing on the intermediate hydroxide, and demonstrated a reduction in the gate leakage current and current collapse of InAlN/GaN MOS-HEMTs using H_2O vapor.

5.2. Experimental Procedure

We have fabricated two kinds of 0.1 μm gate-length InAlN/GaN MOS-HEMTs using O_2 plasma and H_2O vapor as oxidant sources as shown in Fig. 5-1.[10] The gate area was selectively oxidized under a vacuum before metallization at 300°C using an atomic-layer-deposition chamber. A 2-nm-thick surface-oxide was formed by the following reactions:

$$4M + 3O_2 \rightarrow 2M_2O_3,$$
(M: Metal) (5.1)

$$2M + 6H_2O \rightarrow 2M(OH)_3 + 3H_2,$$
$$2M(OH)_3 \rightarrow M_2O_3 + 3H_2O. \quad (5.2)$$

The thickness of surface-oxide was measured by high-angle annular dark field (HAADF) scanning Transmission Electron Microscope (STEM) as shown in Fig. 5-2.[10] The chemical structure of the surface-oxide was evaluated by X-ray photoelectron spectroscopy (XPS). After device fabrication, the drain-to-source current versus gate-to-source voltage (I_{ds}–V_{gs}) and the gate current versus gate-to-source voltage (I_g–V_{gs}) characteristics were measured at a drain-to-source voltage (V_{ds}) of 5 V. The current collapse was evaluated by decreasing the I_{ds} due to pinched-off bias stress (V_{gs} = -3 V, V_{ds} = 20 V) from pulsed I_{ds}–V_{ds} characteristics. The pulse width and their separation were 1 μs and 1 ms, respectively. The ratio of I_{ds} with bias stress to I_{ds} without bias stress was quantified at a V_{ds} of 5 V.

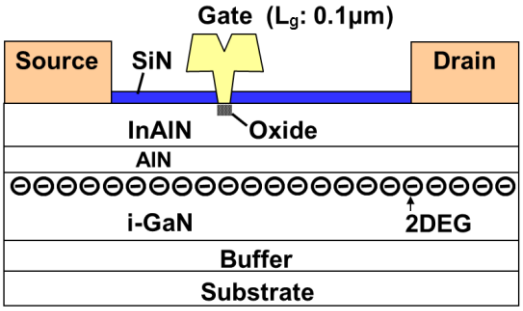

Fig. 5-1. Schematic cross-sectional view of InAlN/GaN MOS-HEMTs used in this work (Reproduced from ref. 10, with the permission of Jon Wiley and Sons).

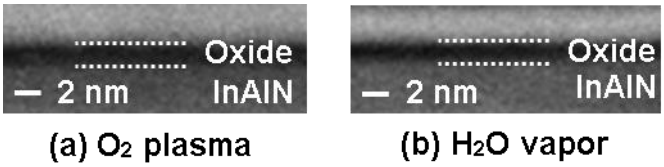

Fig. 5-2. HAADF STEM image of surface-oxide when using (a) O_2 plasma and (b) H_2O vapor (Reproduced from ref. 10, with the permission of Jon Wiley and Sons).

5.3 Results and Discussion

Figure 5-3 shows Oxygen (O) 1s spectrum of the surface-oxide when using O_2 plasma (a) and H_2O vapor (b) measured by XPS.[10] We have conducted a waveform analysis by separating the O 1s spectrum into Al_2O_3 and In_2O_3 to calculate their ratio. As shown in these figures, the ratio of Al_2O_3 to In_2O_3 when using H_2O vapor was larger than that of O_2 plasma due to the decrease in In_2O_3. Then, we focused on the thermal stability of intermediate hydroxide of the H_2O vapor oxidation. According to previous studies,[11, 12] aluminium hydroxide [$Al(OH)_x$] is thermally stable because it changes into Al_2O_3 at 300°C by the following dehydration reaction:

$$2Al(OH)_3 \rightarrow Al_2O_3 + 3H_2O. \quad (5.3)$$

On the other hand, indium hydroxide [$In(OH)_x$] is thermally unstable because it desorbs at 150°C. So, it is suggested that Al_2O_3 was selectively increased when using 300°C H_2O vapor because of $In(OH)_x$ desorption. Conversely, it is difficult to decrease In_2O_3 when using O_2 plasma even at the same temperature as H_2O vapor, because $In(OH)_x$ is not formed on the surface of InAlN by the O_2 plasma oxidation as shown in equation 5.1.

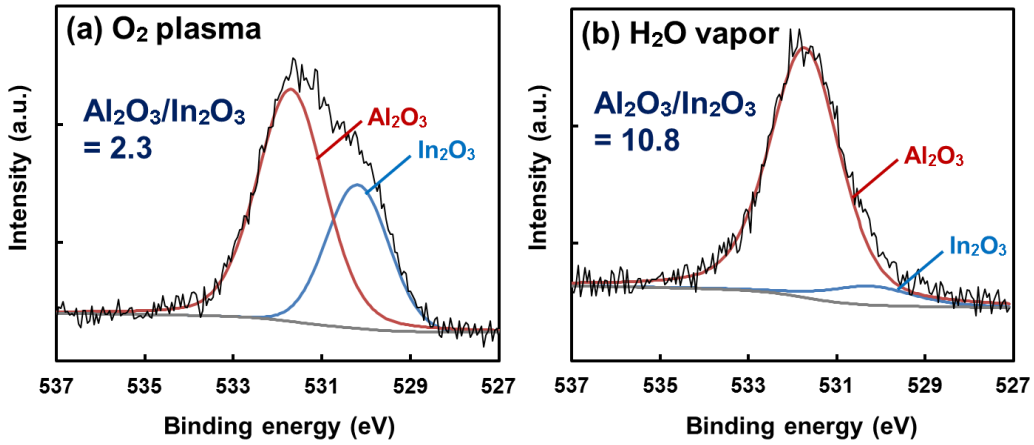

Fig. 5-3. O 1s spectrum of surface-oxide when using (a) O_2 plasma and (b) H_2O vapor measured by XPS (Reproduced from ref. 10, with the permission of Jon Wiley and Sons).

To investigate the effect of decreasing In_2O_3 for the surface-oxide on the gate leakage current of InAlN/GaN MOS-HEMTs, we measured the I_{ds}–V_{gs} and I_g–V_{gs} characteristics of InAlN/GaN MOS-HEMTs using O_2 plasma and H_2O vapor. InAlN/GaN HEMTs (without oxide) were used as a reference. As shown in Fig. 5-4, the gate leakage current of InAlN/GaN MOS-HEMTs was reduced by both oxidant

sources.[10] However, the gate leakage when using H_2O vapor was one order of magnitude lower than that of O_2 plasma. This means that decreasing In_2O_3 for the surface-oxide is effective in reducing the gate leakage current when using H_2O vapor, as we had expected.

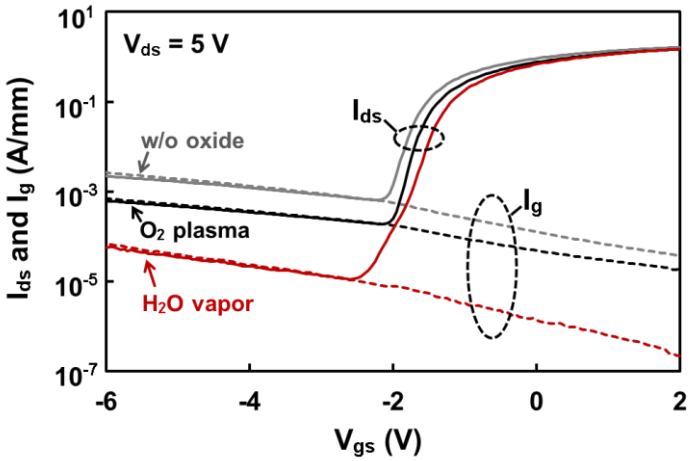

Fig. 5-4. I_{ds}–V_{gs} and I_g–V_{gs} characteristics of InAlN/GaN MOS-HEMTs (Reproduced from ref. 10, with the permission of Jon Wiley and Sons).

After that, we evaluated the current collapse of InAlN/GaN MOS-HEMTs. Figure 5-5 shows the pulsed I_{ds}–V_{ds} characteristics of InAlN/GaN HEMT (a), and InAlN/GaN MOS-HEMTs when using O_2 plasma (b) and H_2O vapor (c).[10] The current collapse was quantified by the ratio of I_{ds} with bias stress to I_{ds} without bias stress at the V_{ds} of 5 V. As shown in these figures, the current collapse was successfully reduced when using H_2O vapor which decreased In_2O_3 for the surface-oxide. Therefore, it is assumed that the electron trap in the surface-oxide was reduced by changing the oxidant source from O_2 plasma to H_2O vapor due to the decrease in In_2O_3.

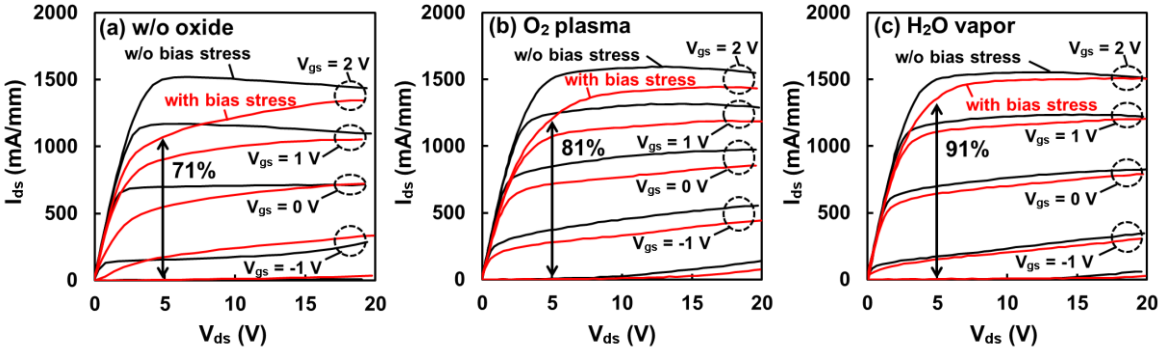

Fig. 5-5. Current collapse of (a) InAlN/GaN HEMT, and InAlN/GaN MOS-HEMTs when using (b) O_2 plasma and (c) H_2O vapor (Reproduced from ref. 10, with the permission of Jon Wiley and Sons).

Then, we used a transmission-line-model (TLM) method to evaluate the electron trap in the surface-oxide. The passivation films were not deposited by focusing on the surface-oxide. As shown in Fig. 5-6, the sheet resistance (R_{sh}) will increase if the electron is captured in the surface-oxide.[10] On the other hand, the captured electron is released and R_{sh} will return to the initial value if the amount of photon energy that is applied corresponds to the trap levels. So, we measured R_{sh} before and after light irradiation using a halogen lamp which has broadband wavelength (380–900 nm), and evaluated the electron trap by focusing on the decrease in R_{sh}.

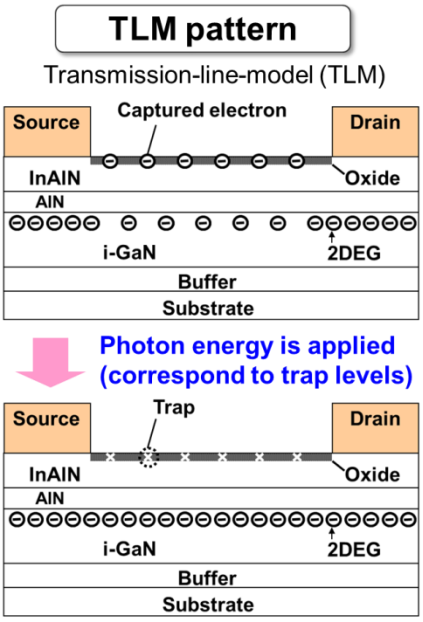

Fig. 5-6. Schematic cross-sectional view of TLM pattern used in evaluation for electron trap (Reproduced from ref. 10, with the permission of Jon Wiley and Sons).

Figure 5-7 shows a comparison of R_{sh} obtained before and after light irradiation when using O_2 plasma and H_2O vapor.[10)] The level of photon energy was 1.38–3.26 eV. As shown in Fig. 5-7, the R_{sh} of O_2 plasma was larger than that of H_2O vapor under the dark condition. However, the values were almost the same under the light condition, because the decrease in R_{sh} was drastic when using O_2 plasma. It is suggested that a number of electron traps exist in the surface-oxide when using O_2 plasma. According to previous studies,[13, 14)] the major trap sites in Al_2O_3 and In_2O_3 are the oxygen vacancies and their trap levels are located at around 2.45 and 1.6–2.0 eV from the conduction band edge, respectively. These values corresponded with the photon energy used in our experiment. So, the trap sites in the surface-oxide were possibly attributed to the oxygen vacancies. Furthermore, the Gibbs free energy of In_2O_3 (-198.6 kcal/mol) is larger than that of Al_2O_3 (-377.9 kcal/mol).[15)] So, In_2O_3 is unstable compared with Al_2O_3, and an electron trap such as an oxygen vacancy is easily generated in In_2O_3.[16)] For this reason, surface-oxide-control with H_2O vapor is effective in reducing the electron trap due to the decrease in In_2O_3, and so the current collapse could be reduced.

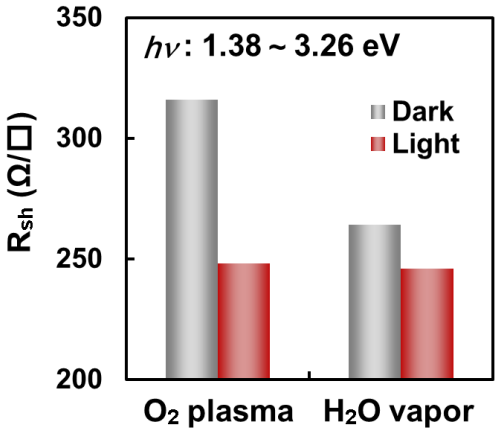

Fig. 5-7. Comparison of R_{sh} obtained before and after light irradiation when using O_2 plasma and H_2O vapor. The level of photon energy was 1.38–3.26 eV (Reproduced from ref. 10, with the permission of Jon Wiley and Sons).

Figure 5-8 shows our proposed mechanism for surface-oxide control of InAlN/GaN MOS-HEMTs.[10)] Figure 5-8 (a) shows the situation when O_2 plasma is used. In this case, the ratio of Al_2O_3 to In_2O_3 for the surface-oxide is small due to the increase in In_2O_3, so the gate leakage current could not be effectively reduced because the bandgap of the surface-oxide is narrow. Furthermore, an electron trap such as an oxygen vacancy is easily generated in In_2O_3, so the I_{ds} is decreased by the current collapse. On the other hand, as shown in Fig. 5-8 (b), the ratio of Al_2O_3 to In_2O_3 could be increased when using H_2O vapor due to the decrease in In_2O_3. So, the gate leakage current and current collapse are successfully reduced when using H_2O vapor. Therefore, decreasing In_2O_3 for the surface-oxide has a key role in reducing the gate leakage current and current collapse of InAlN/GaN MOS-HEMTs.

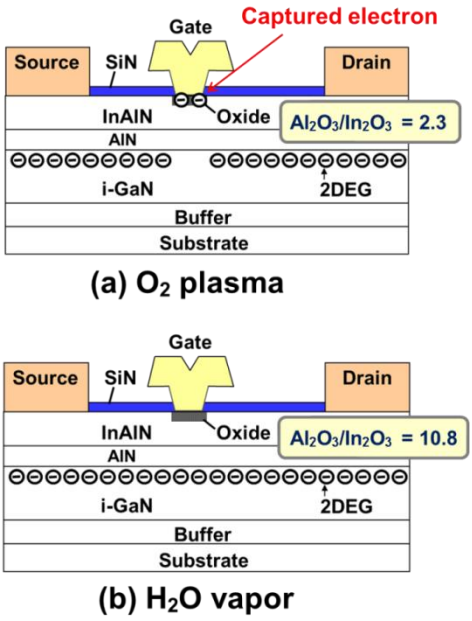

Fig. 5-8. Schematic cross-sectional view of proposed mechanism for surface-oxide-control of InAlN/GaN MOS-HEMTs when using (a) O_2 plasma and (b) H_2O vapor (Reproduced from ref. 10, with the permission of Jon Wiley and Sons).

5.4. Conclusion

We have investigated the effect of oxidant sources on the performance of InAlN/GaN MOS-HEMTs. We clarified that the surface-oxide of InAlN is comprised of Al_2O_3 and In_2O_3 when using conventional O_2 plasma, and In_2O_3 causes the gate leakage current and current collapse of InAlN/GaN MOS-HEMTs due to its narrow bandgap and electron traps such as oxygen vacancies. Then, we proposed H_2O vapor oxidation to decrease In_2O_3 for the surface-oxide by focusing on the thermal stability of intermediate hydroxide. $Al(OH)_x$ is thermally stable because it changes into Al_2O_3 at 300°C. On the other hands, $In(OH)_x$ is thermally unstable because it desorbs at 150°C. Therefore,

Al_2O_3 was selectively increased when using 300°C H_2O vapor because of $In(OH)_x$ desorption, and the gate leakage current and current collapse were successfully reduced due to the decrease in In_2O_3. We concluded from these results that a key role in improving the performance of InAlN/GaN MOS-HEMTs is decreasing In_2O_3 for the surface-oxide.

References

1) T. Kikkawa, Jpn. J. Appl. Phys. **44**, 4846 (2005).
2) T. Kikkawa, K. Makiyama, T. Ohki, M. Kanamura, K. Imanishi, N. Hara, and K. Joshin, Phys. Status Solidi A **206**, 1135 (2009).
3) S. Masuda, T. Ohki, K. Makiyama, M. Kanamura, N. Okamoto, H. Shigematsu, K. Imanishi, T. Kikkawa, K. Joshin, and N. Hara, EuMIC Dig., 1796 (2009).
4) K. Makiyama, T. Ohki, M. Kanamura, K. Joshin, K. Imanishi, N. Hara, and T. Kikkawa, Phys. Status Solidi C **6**, 1012 (2009).
5) M. Micovic, A. Kurdoghlian, H. P. Moyer, P. Hashimoto, M. Hu, M. Antcliffe, P. J. Willadsen, W. S. Wong, R. Bowen, I. Milosavljevic, Y. Yoon, A. Schmitz, M. Wetzel, C. McGuire, B. Hughes, and D. H. Chow, IEEE CSIC Symp. Dig., 10 (2008).
6) K. Makiyama, S. Ozaki, N. Okamoto, T. Ohki, Y. Niida, Y. Kamada, K. Joshin, and K. Watanabe, Proceedings of Lester Eastman Conference on High Performance Devices, S5-H7 (2014).
7) M. Alomari, F. Medjdoub, J. F. Carlin, E. Feltin, N. Grandjean, A. Chuvilin, U. Kaiser, C. Gaquière, and E. Kohn, IEEE Electron Device Lett. **30**, 1131 (2009).
8) D. S. Lee Jinwook, W. Chung, H. Wang, X. Gao, S. Guo, P. Fay, and T. Palacios, IEEE Electron Device Lett. **32**, 755 (2011).
9) M. Akazawa, B. Gao, T. Hashizume, M. Hiroki, S. Yamahata, and N. Shigekawa, J. Appl. Phys. **109**, 013703 (2011).
10) S. Ozaki, K. Makiyama, T. Ohki, Y. Kamada, M. Sato, Y. Niida, N. Okamoto, and K. Joshin, Phys. Status Solidi **A** 213, 1259, (2015).
11) J. G. Speight, Lange' s Handbook of Chemistry 16th Ed., 1.37 (2005).
12) A. W. Ott, J. W. Klaus, J. M. Johnson, and S. M. George, Thin Solid Films **292**, 135 (1997).
13) D. Liu, S. J. Clark, and J. Robertson, Appl. Phys. Lett. **96**, 032905 (2010).
14) Z. P. Wei, D. L. Guo, B. Liu, R. Chen, L. M. Wong, W. F. Yang, S. J. Wang, H. D. Sun, and T. Wu, Appl. Phys. Lett. **96**, 031902 (2010).
15) O. Salihoglu, A. Muti, K. Kutluer, T. Tansel, R. Turan, C. Kocabas, and A. Aydinli, Proceedings of SPIE **8353**, 83530Z (2012).
16) G. Frank and H. Kostlin, Appl. Phys. A **27**, 197 (1982).

Chapter 6

Improved performance and operation stability of Al_2O_3/InAlN/GaN MOS-HEMTs with post-metallization annealing process

6.1. Introduction

As described above, GaN-based high electron mobility transistors (HEMTs) have been making steady progress in high-frequency and high-power applications, such as radio frequency (RF) amplifiers in wireless base stations and radar systems.[1)] An electron saturation velocity as high as 2×10^7 cm/s and a high two-dimensional electron gas (2DEG) density of over 1×10^{13} cm^{-2}, which originate from spontaneous and piezoelectric polarization fields as well as from a large conduction band offset, are well-suited for power amplifiers. It is known that GaN HEMTs using In-based barrier layers such as InAlN and InAlGaN are promising because of their high spontaneous polarization and high band offset at the conduction band, for enhancing 2DEG density.[2–4)] In fact, Makiyama *et al*.[5)] demonstrated an output power density of 3 W/mm at 96 GHz in GaN HEMTs using InAlGaN barrier layers. These are desirable for the fifth generation (5G) communication system where the W band (75–110 GHz) and the E band (60–90 GHz) frequency ranges are expected to be used for the wireless backhaul of mobile communications. However, a large gate leakage current of InAlN/GaN HEMTs often limits their operations.[6)] Appropriately, metal-oxide-semiconductor (MOS) structures are suitable for addressing the leakage current issue and therefore improving the performance of InAlN/GaN HEMTs.[7-14)]

Among the various kinds of insulators that have been applied to achieve excellent performance of InAlN/GaN MOS-HEMTs, Al_2O_3 has been one of the most attractive because of its wide bandgap (~7.0 eV), high dielectric constant (~9.0), and high breakdown voltage (~10 MV/cm). To obtain stable performance and reliability for Al_2O_3/InAlN/GaN MOS-HEMTs, a low-state-density at the Al_2O_3/InAlN interface is absolutely required similar to AlGaN/GaN MOS-HEMTs.[15–17)] However, Al_2O_3/InAlN/GaN MOS-HEMTs are still suffering from unexpected issues such as an instability of the threshold voltage (V_{th}), a steep decrease in transconductance (g_m) at forward gate bias and severe current collapse which is a temporary reduction of the drain current under high power operation. Especially, in the case of millimeter-wave applications including W-band and E-band, the current collapse increases with short

gate-length (less than 200 nm) due to a high electric field at the gate edge.[4, 18)]

In this chapter, we evaluated the DC characteristics and operation stability of Al_2O_3/InAlN/GaN MOS-HEMTs using ALD-Al_2O_3 by focusing on post-metallization annealing (PMA) process to control defect levels in Al_2O_3[19)] and electronic states at the Al_2O_3/InAlN interface.[20, 21)]

6.2. Device fabrication

We fabricated InAlN/GaN MOS-HEMTs as shown in Fig. 6-1.[22)] The gate length, gate width, and gate-drain length were 0.5, 50, and 10 μm, respectively. Al_2O_3 films with a nominal thickness of 20 nm were deposited on the InAlN/GaN HEMT epitaxial structures (InAlN/AlN/GaN/buffer/substrate) by using an atomic-layer-deposition (ALD) method at 300°C. Trimethylaluminum (TMA) and O_2 plasma were used as precursors for ALD. After the Al_2O_3 deposition, we patterned Ni/Au bilayer gate electrode and carried out PMA in air at 300°C for 12 hours. To improve the defect level in Al_2O_3 and electronic states at the Al_2O_3/InAlN interface, we had carried out various kinds of control processes including post-deposition and post-metallization annealing by changing atmosphere, temperature and time. At present, the best result was obtained under the PMA in air at 300°C for 12 hours. According to Kaneki *et al.*,[23)] the annealing process has an effect on reducing the state densities at the Al_2O_3/GaN interface, probably due to the relaxation of dangling bonds and/or point defects at the GaN surface (Al_2O_3/GaN interface). In addition, there is a possibility that such a relaxation of dangling bonds and defects is enhanced by the long-time annealing process. Furthermore, it is also expected that annealing in air (air-annealing) enhances the passivation of dangling bonds including the oxygen vacancies in the oxide films.[24)] Thus, we used long-time PMA in air for ALD-Al_2O_3.

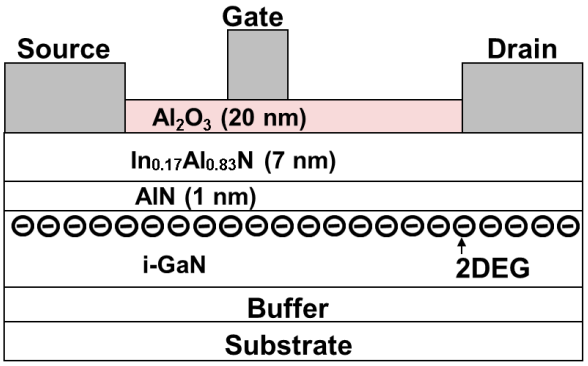

Fig. 6-1. Schematic cross-sectional view of InAlN/GaN MOS-HEMTs used in this work (Reproduced from ref. 22, copyright 2017 by the Japan Society of Applied Physics).

6.3. Results and Discussion

6.3.1. DC characteristics of Al_2O_3/InAlN/GaN MOS-HEMTs

Figure 6-2 shows the drain-to-source current versus drain-to-source voltage (I_{ds}–V_{ds}) characteristics of InAlN/GaN MOS-HEMTs without (a) and with PMA (b).[22] The gate-to-source voltage (V_{gs}) was varied from -5 to 2 V with a 1 V step. We confirmed that the I_{ds}–V_{ds} characteristics were improved by PMA with a maximum drain current (I_{max}) of 1140 mA/mm and an on-state resistance (R_{on}) of 5.3 Ω.mm at a V_{gs} of 2 V. These characteristics are relatively well behaved compared with previous reports.[10–14] After PMA, we also confirmed the decrease in sheet resistance (R_{sh}) around 12% from the transmission-line-model (TLM) measurement. Thus, it is likely that the improvement of I_{max} and R_{on} with PMA was attributed to the decrease in R_{sh}, probably due to the increase in the 2DEG density. A possible mechanism for the decrease in R_{sh} will be discussed later.

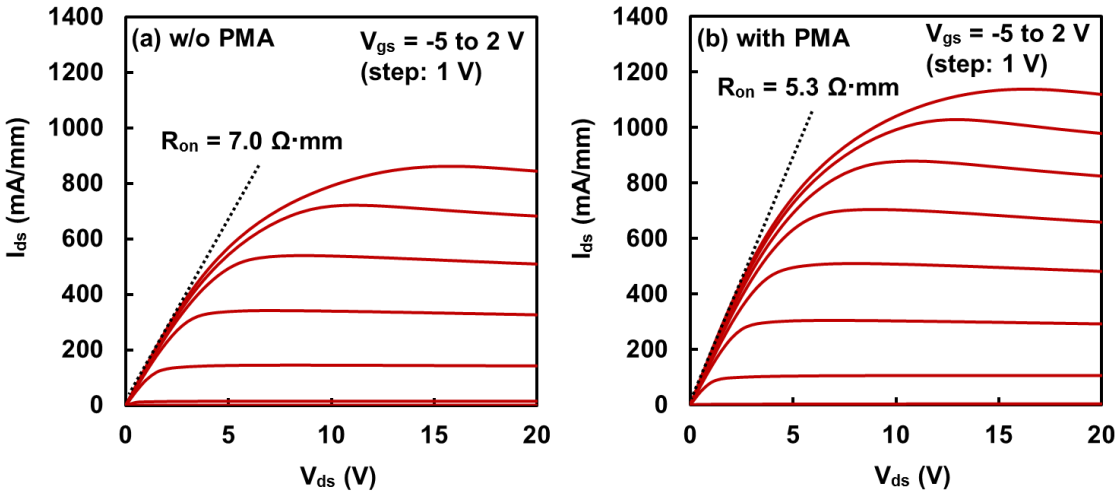

Fig. 6-2. I_{ds}–V_{ds} characteristics of InAlN/GaN MOS-HEMTs (a) without and (b) with PMA (Reproduced from ref. 22, copyright 2017 by the Japan Society of Applied Physics).

Figure 6-3 (a) shows the I_{ds}–V_{gs} and g_m–V_{gs} characteristics of InAlN/GaN MOS-HEMTs measured at a V_{ds} of 15 V.[22] It was confirmed that the V_{th} was shifted to the reverse bias direction after PMA. This is dominantly due to the increase in the 2DEG density and the reduction of defect levels in Al_2O_3. In addition, we observed improvement of g_m linearity (the wider range of constant g_m) after PMA. We calculated the subthreshold slope of InAlN/GaN MOS-HEMTs from the log scale I_{ds}–V_{gs} characteristics as shown in Fig. 6-3 (b). A high value of subthreshold slope was obtained before PMA. It is likely that various kinds of defects such as dangling bonds, point defects and oxidized-InAlN,[4] resulted in high state density at the Al_2O_3/InAlN interface before PMA. On the other hand, the subthreshold slope was significantly decreased, down to 75 mV/dec with PMA. These results indicate that the interface properties of InAlN/GaN MOS-HEMTs were improved by PMA process.

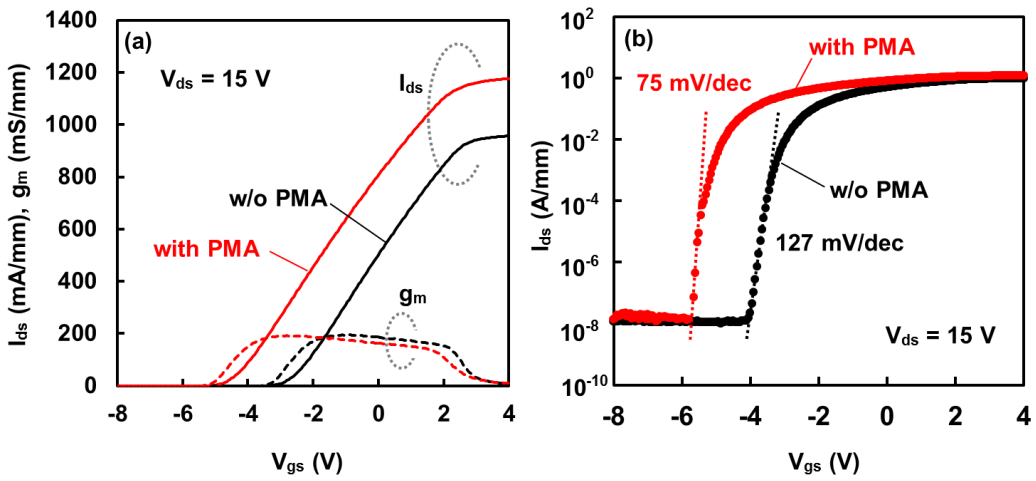

Fig. 6-3. (a) I_{ds}–V_{gs} and g_m–V_{gs} characteristics of InAlN/GaN MOS-HEMTs without and with PMA. (b) Log scale I_{ds}–V_{gs} characteristics of InAlN/GaN MOS-HEMTs without and with PMA (Reproduced from ref. 22, copyright 2017 by the Japan Society of Applied Physics).

Figures 6-4 (a) and (b) show the potential profile of the Al_2O_3/InAlN/GaN structures[22] as calculated by using the numerical solver of the one-dimensional Poisson equation designed by Miczek *et al.*[25] We calculated the surface potential (V_S) of InAlN by changing the V_{gs} to understand the gate controllability of InAlN/GaN MOS-HEMTs. V_S was defined as follows:

$$V_S = E_C - E_F. \tag{6-1}$$

where E_C and E_F are the energy at the conduction band minimum and the Fermi level, respectively. We assumed two types of interface state density distributions D_{it} (E) at the Al_2O_3/InAlN interface, as shown in Fig. 6-4 (c).[22] In the case of high D_{it}, the V_S was poorly controlled with changing the V_{gs} from 0 to 5 V. The V_S change (ΔV_S) was estimated to be 0.3 eV. On the other hand, the V_S controllability was significantly improved by the reduction in state densities at the Al_2O_3/InAlN interface (ΔV_S = 1.3 eV between V_{gs} = 0 and 5 V). Therefore, it is considered that the improvement of g_m linearity and subthreshold slope was attributed to the decrease in state densities at the Al_2O_3/InAlN interface with PMA.

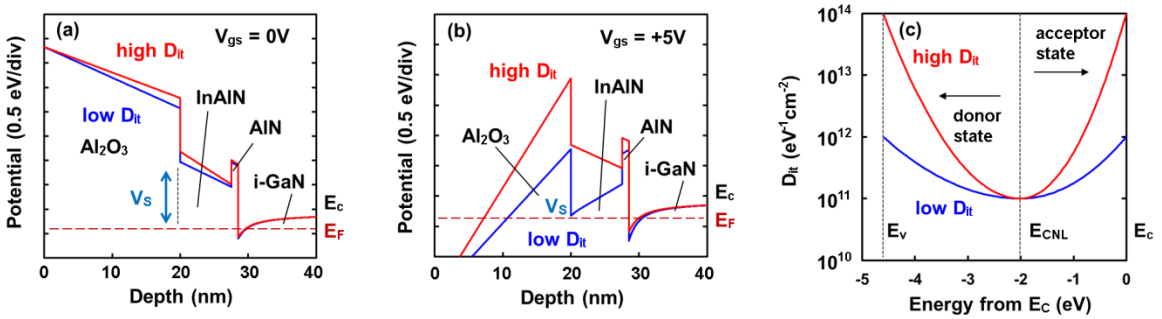

Fig. 6-4. Potential profile of Al_2O_3/InAlN/GaN structures at (a) V_{gs} = 0 V and (b) V_{gs} = +5 V. (c) Interface state density distributions used in calculation (Reproduced from ref. 22, copyright 2017 by the Japan Society of Applied Physics).

6.3.2. Characterization of ALD-Al_2O_3

Subsequently, we evaluated the defects in ALD-Al_2O_3 before and after annealing by using cathodoluminescence (CL). In the metal oxides, nonstoichiometry and point defects, such as impurity, vacancy, and interstitial, are generally presented. According to Jonnard *et al.*,[26] the defects related to oxygen vacancies such as F^+ center (oxygen vacancy having trapped one electron) and F center (oxygen vacancy having trapped two electrons) are mainly analyzed by CL. In our experiment, we used blanket ALD-Al_2O_3 deposited on quartz substrate by focusing on the oxygen vacancies in the Al_2O_3 films. Figure 6-5 shows CL spectra of ALD-Al_2O_3 before and after annealing.[22] To clarify the effect of air-annealing, we also evaluated N_2 annealing for ALD-Al_2O_3 as a reference. The condition of N_2 annealing such as temperature and time (except for atmosphere) was the same as air-annealing (300°C for 12 hours). The 330 and 420 nm peaks were attributed to F^+ and F centers, respectively. After air-annealing, both peaks were significantly decreased, indicating the reduction in oxygen vacancies in ALD-Al_2O_3. This behavior was not observed when using N_2 annealing. Considering these results, there is a possibility that air-annealing enhances the relaxation and the passivation of dangling bonds in ALD-Al_2O_3 including the oxygen vacancies.

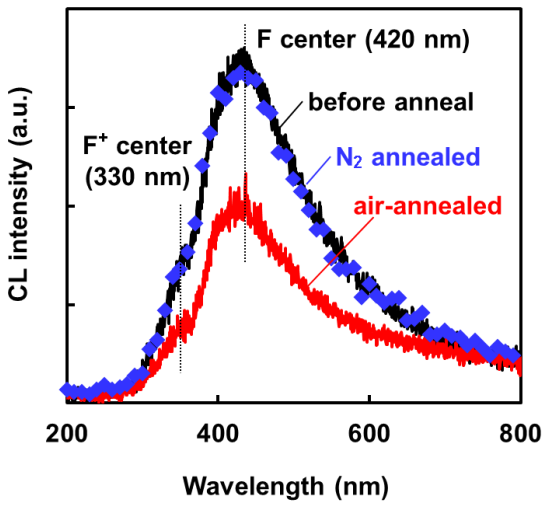

Fig. 6-5. Cathodeluminescence of ALD-Al_2O_3 before and after annealing (Reproduced from ref. 22, copyright 2017 by the Japan Society of Applied Physics).

Table 6-1[22] shows the mass density and film stress of ALD-Al_2O_3 as evaluated using the Rutherford backscattering spectrometry (RBS) and thin film stress measurement.[27, 28] We confirmed that the mass density of ALD-Al_2O_3 before and after N_2 annealing was close to that of the previous study which used O_2 plasma as an oxidant source for ALD.[29] The increase in mass density with N_2 annealing was less than 4%. On the other hand, the mass density significantly increased, up to 3.3 g/cm^3 with air-annealing, probably due to the reduction in oxygen vacancies and the relaxation of dangling bonds in ALD-Al_2O_3. It was also confirmed the shrinkage of ALD-Al_2O_3 around 10% from the ellipsometry measurement taken after air-annealing. As shown in Table 6-1, we confirmed that the ALD-Al_2O_3 without annealing had tensile stress similar to reported values by Azize *et al.*[30] and Joglekar *et al.*[31] On the other hand, the air-annealing process increased tensile stress significantly. Krautheim *et al.*[28] reported that the tensile stress of ALD-Al_2O_3 was increased by annealing, and the main reason for this behavior is the volume reduction with increase in mass density. Thus, it is considered that the increase in tensile stress of our ALD-Al_2O_3 can be attributed to the shrinkage as a result of the densification through air-annealing.

Table 6-1. Mass density and film stress of ALD-Al_2O_3 before and after annealing (Reproduced from ref. 22, copyright 2017 by the Japan Society of Applied Physics).

	Mass density (g/cm^3)	Tensile stress (MPa)
before anneal	2.9	403
N_2 annealed	3.0	415
air-annealed	3.3	455

Figure 6-6 shows the polarization vectors and the schematic energy band diagrams of the Al_2O_3/InAlN/GaN structures before and after air-annealing.[22] According to Jeon *et al.*,[32] when the tensile stress is applied to the electron-supplying layer in GaN HEMTs, the piezoelectric polarization (P_{PE}) is enhanced. The P_{PE} increases the electric field in the electron-supplying layer because the direction of the P_{PE} is the same as that of the spontaneous polarizations (P_{SP}). Therefore, as the tensile stress was applied to the InAlN electron-supplying layer by air-annealing, the 2DEG density increased at the InAlN/GaN interface, as shown in Fig. 6-6 (b). We assumed P_{PE} in the InAlN electron-supplying layer after air-annealing as -3.5×10^{-6} C/cm^2 by using tensile strain value of 2%. The conduction-band offsets between Al_2O_3/InAlN, InAlN/AlN and AlN/GaN were 0.9, 0.5, and 1.5 eV, respectively.[20, 33] In view of this behavior, the P_{PE} applied by air-annealed ALD-Al_2O_3 attribute to the decrease in R_{sh} with PMA in our experiment.

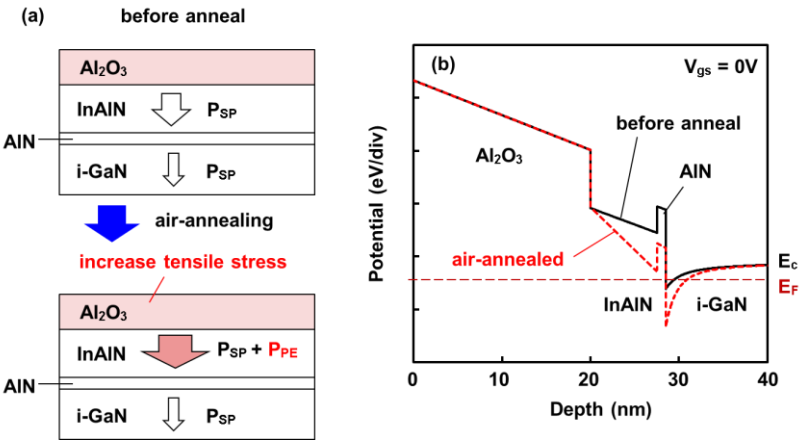

Fig. 6-6. (a) Polarization vectors and (b) schematic energy band diagrams of Al_2O_3/InAlN/GaN structures obtained before and after air-annealing (Reproduced from ref. 22, copyright 2017 by the Japan Society of Applied Physics).

6.3.3. Operation stability of Al_2O_3/InAlN/GaN MOS-HEMTs

We then investigated the operation stability of Al_2O_3/InAlN/GaN MOS-HEMTs with PMA. Figure 6-7 shows the leakage characteristics of InAlN/GaN MOS-HEMTs without and with PMA.[22] We confirmed that the gate leakage current was slightly suppressed by PMA process. Choi *et al.*[19] theoretically predicted that the oxygen vacancies in the Al_2O_3 films act as border traps, and they lead to the leakage current in Al_2O_3/GaN MOS structures. Therefore, the suppression in the gate leakage current would relate to the reduction in the oxygen vacancies in ALD-Al_2O_3 with PMA.

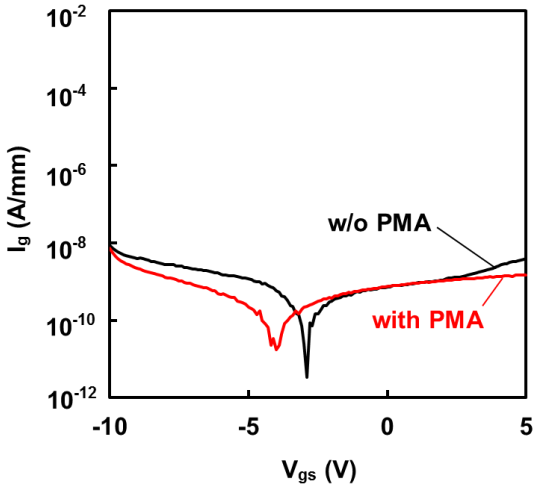

Fig. 6-7. Leakage characteristics of InAlN/GaN MOS-HEMTs without and with PMA (Reproduced from ref. 22, copyright 2017 by the Japan Society of Applied Physics).

Figure 6-8 shows the V_{th} shift (ΔV_{th}) as a function of the maximum forward bias voltage (V_{MF}).[22] In our experiment, the V_{th} was determined at I_{ds} = 1 μA/mm from the log scale I_{ds}–V_{gs} curves, and the V_{MF} was changed from 2 to 10 V. As shown in Fig. 6-8, the ΔV_{th} was increased by increasing the V_{MF} for both samples. On the other hand, the ΔV_{th} after PMA was smaller than that of before PMA, at the same V_{MF}. Defect levels in insulator films, border traps in insulator films near the insulator/(Al)GaN interfaces, and acceptor-type interface states at the insulator/(Al)GaN interface are involved in the ΔV_{th} mechanism in GaN MOS-HEMTs.[7] The higher forward gate bias induces the higher gate leakage current probably due to the Fowler–Nordheim tunneling process, leading to electron injection to traps and interface states mentioned above. Thus, the decrease in ΔV_{th} also attributed to the reduction in those traps and states with PMA.

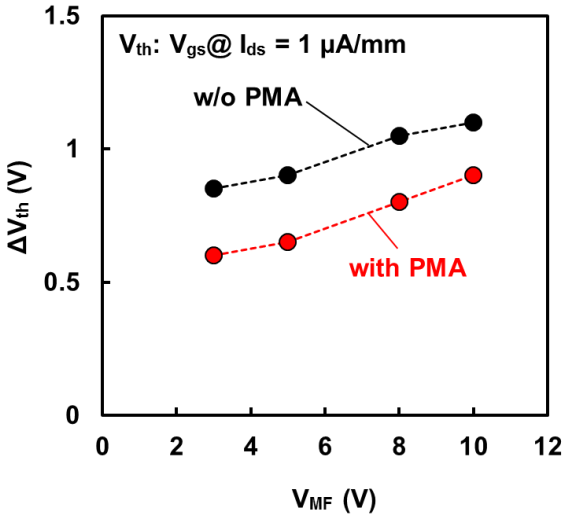

Fig. 6-8. ΔV_{th} of InAlN/GaN MOS-HEMTs as a function of V_{MF} (Reproduced from ref. 22, copyright 2017 by the Japan Society of Applied Physics).

Then, we measured pulsed *I*–*V* characteristics of Al_2O_3/InAlN/GaN MOS-HEMTs to evaluate the current collapse. The current collapse is one of the critical issues for operation stability, because it causes RF performance degradations, due to the decrease in the drain current under operation. According to the widely accepted "virtual gate" model,[34] a high off-state drain bias voltage induces electron trapping at the surface states of the barrier layer via a tunneling injection at the gate edge on the drain side. Subsequently, surface charges deplete the underlying 2DEG and increase the drain resistance, leading to current collapse. Figure 6-9 shows the pulsed I_{ds}–V_{ds} characteristics of Al_2O_3/InAlN/GaN MOS-HEMTs without (a) and with PMA (b), measured at a V_{gs} of 0 and 2 V. In this case, the pulse width and their separation were 1 μs and 1 ms, respectively. For the MOS-HEMT without PMA, a significant current decrease was observed under the off-state quiescent bias with a high drain voltage ($V_{gs\text{-}q}$ = -7 V and $V_{ds\text{-}q}$ = 20 V). In addition, this quiescent bias made the gate control of the current very difficult, indicating that the pronounced current collapse behavior was due to the surface charging and the potential pinning at the InAlN surface, particularly in the gate-to-drain access region. On the other hand, the PMA process effectively mitigated the current collapse effects, as shown in Fig. 6-9 (b).

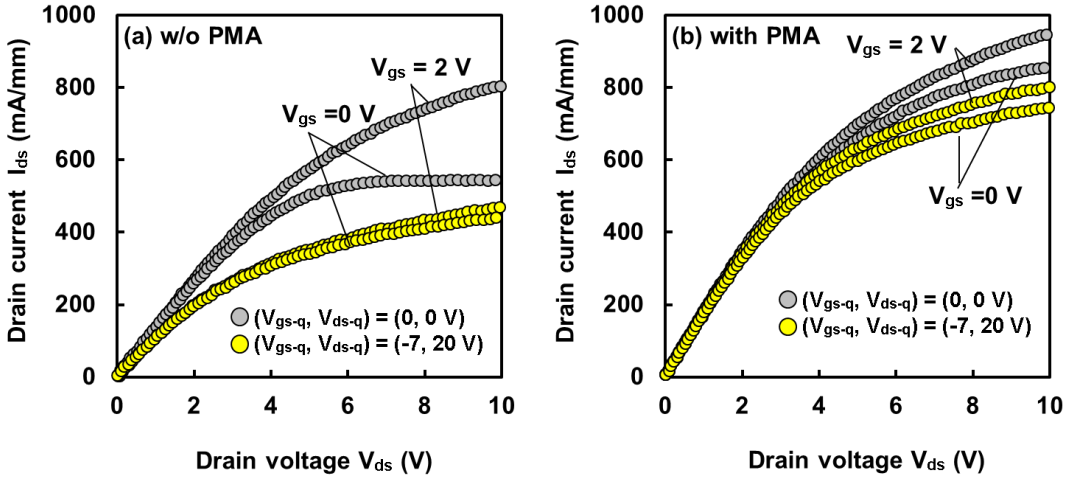

Fig. 6-9. Pulsed I_{ds}–V_{ds} characteristics of Al_2O_3/InAlN/GaN MOS-HEMTs (a) without and (b) with PMA.

The current collapse was then evaluated by the R_{on} increase after applying a pinched-off bias stress (R_{on} with bias stress/R_{on} without bias stress) at a V_{gs} of 2 V. The R_{on} increase as a function of the quiescent drain bias (V_{ds-q}) is shown in Fig. 6-10. In the sample without PMA, a significant R_{on} increase was observed with increasing V_{ds-q}. The current collapse is strongly dependent on the drain voltage during the off-state stress.[35, 36] On the basis of the gate injection and surface-hopping model,[37, 38] electron conduction via trap-to-trap hopping can be promoted with an increasing drain voltage. Consequently, this may lead to the widening of the "virtual gate" from the gate edge until some further distance on the gate-to-drain access region.[39] Thus, it is likely that various kinds of defects such as dangling bonds and point defects resulted in high state densities at the Al_2O_3/InAlN interface before PMA. On the other hand, the R_{on} increase was suppressed with PMA, indicating the interface properties of the Al_2O_3/InAlN/GaN MOS-HEMTs were improved by PMA process. These pulsed *I*–*V* characteristics are relatively well behaved compared with previous reports.[11, 12, 40] Cico *et al.*[40] also observed a similar reduction in the current collapse for Al_2O_3/InAlN/GaN MOS-HEMTs by forming gas annealing (N_2 was 90% and H_2 was 10%) at 700°C. They demonstrated that deep level states such as vacancy-type defects were removed by forming gas annealing at the Al_2O_3/InAlN interface, because a significant reduction in the *C*–*V* hysteresis was observed due to ultraviolet light irradiation (2.58–3.88 eV) after forming gas annealing.

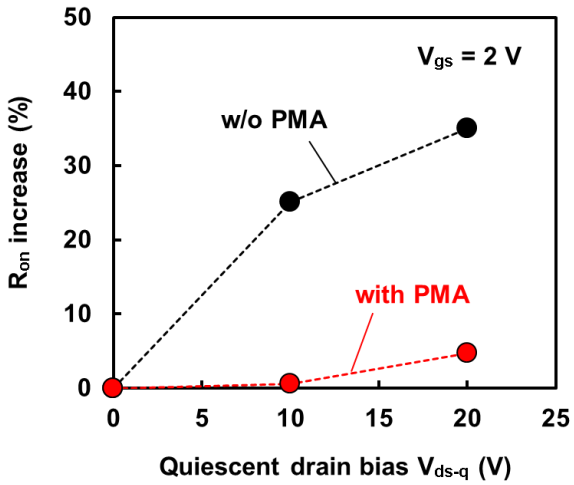

Fig. 6-10. Comparison of R_{on} increase as a function of Quiescent drain bias.

6.3.4. Al_2O_3/InAlN interface characterization

To evaluate the Al_2O_3/InAlN interface properties, we carried out photo-assisted *C–V* measurements on the Al_2O_3/InAlN/GaN MOS-HEMTs with a photon energy (*hv*) from 1.38 to 2.58 eV. We used MOS diodes fabricated on the same Al_2O_3/InAlN/GaN heterostructures. Figure 6-11 shows schematic illustrations of the photo-assisted electron emission at the Al_2O_3InAlN interface (a) and photo-assisted *C–V* characteristics (b), before and after the illumination. First, the gate voltage was swept from 0 to -20 V at 100 kHz under a dark condition. Then, the gate voltage was kept at -20 V and the monochromatic light was illuminated on the sample surface for 60 s. Consequently, we observed the photo-assisted electron emission from the interface states with the energy range corresponding to the photon energy range. After the illumination, the *C–V* sweeping was restarted toward 0 V under a dark condition. When the sample surface is illuminated with a higher photon energy, a larger amount of photo-assisted electron emission causes larger V_{th} shifts in the *C–V* curves. The parallel *C–V* shift toward the reverse bias direction indicates that the interface states at the Al_2O_3/InAlN act as fixed charges in this bias range.[41, 42] Figure 6-12 shows the photo-assisted *C–V* characteristics of the Al_2O_3/InAlN/GaN MOS-HEMTs without (a) and with PMA (b). In the sample without PMA, we observed clearer V_{th} shift than for the sample with PMA. The V_{th} shift

before PMA was enlarged with increasing a photon energy, as shown in Fig. 6-12 (a), indicated high-density electronic states near midgap at the Al_2O_3/InAlN interface before PMA. On the other hand, interface states were effectively reduced after PMA, contributing to the reduction in the current collapse of the Al_2O_3/InAlN/GaN MOS-HEMTs.

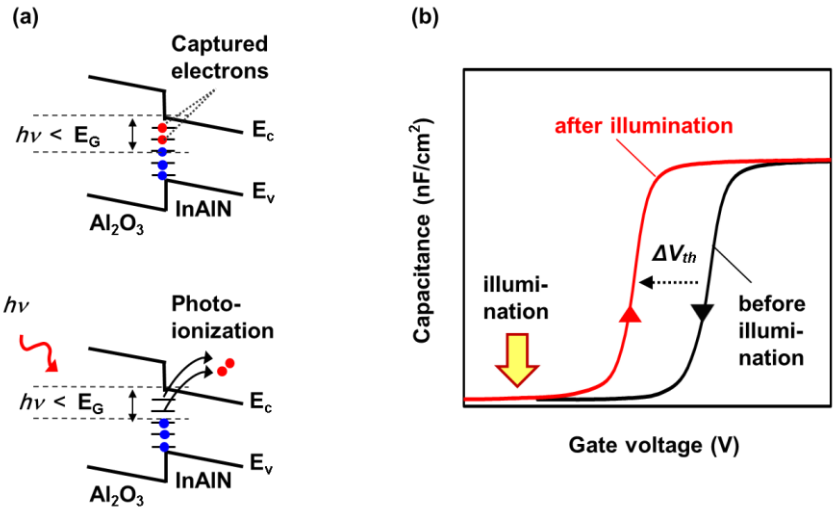

Fig. 6-11. Schematic illustrations of (a) photo-assisted electron emission at Al_2O_3/InAlN interface and (b) photo-assisted *C*–*V* characteristics.

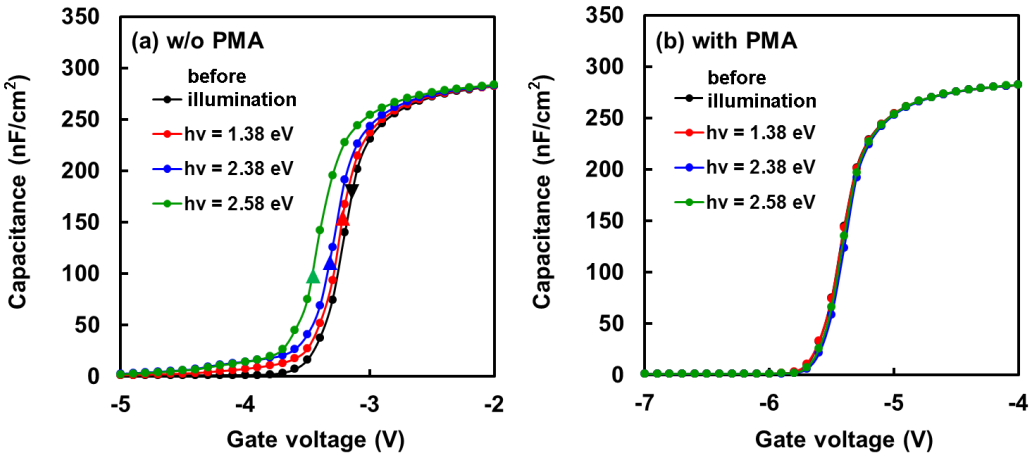

Fig. 6-12. Photo-assisted *C*–*V* characteristics of Al_2O_3/InAlN/GaN MOS-HEMTs (a) without and (b) with PMA.

Figures 6-13 (a) and (b) show the transmission electron microscope (TEM) images of the Al_2O_3/InAlN structures without and with PMA. For both images, periodic lattice points are clearly observed in the InAlN layer. By analyzing the periodicity of the lattice point pattern, a relative lattice constant of InAlN along c-axis at the Al_2O_3/InAlN interface was estimated, as indicated by the dotted lines in Figs. 6-13 (a) and (b). The relative lattice constant with respect to the ideal lattice constant of $In_{0.17}Al_{0.83}N$ (0.5105 nm) are plotted in Fig. 6-13 (c). A significant variation of the lattice constants was observed for the sample without PMA, indicating the disorder in the atomic bonding configuration at the Al_2O_3/InAlN interface. At an actual semiconductor surface, the termination of crystalline periodicity causes a peculiar bond configuration that includes dangling bonds and dimer bonds. In addition, the surface involves vacancies, adatoms and natural oxides. Such surface irregularity induces lattice disorder in bond lengths and angles. For example, Xue *et al*.[43] theoretically calculated the effect of Ga vacancies on the bond disorder at the Ga-polar GaN (0001) surface. They demonstrated that the electron transfer from the Ga-dangling bond to the N-dangling bond of a second layer N atom induced the downward relaxation of the neighboring Ga atom by 0.39 Å along c-axis. For the Al_2O_3/InAlN sample without PMA (as-deposited sample), the bond disorder at the InAlN surface remained almost unchanged even after the Al_2O_3 deposition, leading to the pronounced variation of the lattice constants, as shown in Fig. 6-13 (c). It is likely that such bond disorder is responsible for the high-density electronic states at the Al_2O_3/InAlN interface.[44, 45]

As shown in Fig. 6-13 (c), the sample with PMA showed a relatively flat distribution of the lattice constants, indicating that the PMA process is effective for the termination of the dangling bonds with O atoms and relaxation of the surface defects. This could improve the bond termination and the bonding order configuration at the Al_2O_3/InAlN interface, and the resulting reduction of the interface states was responsible for the improvement of the gate controllability and the operation stability, as shown in above. In fact, Zywietz *et al*.[46] predicted from theoretical calculations that the termination of Ga dangling bonds by O atoms effectively reduced the density of states (surface states) within the bandgap.

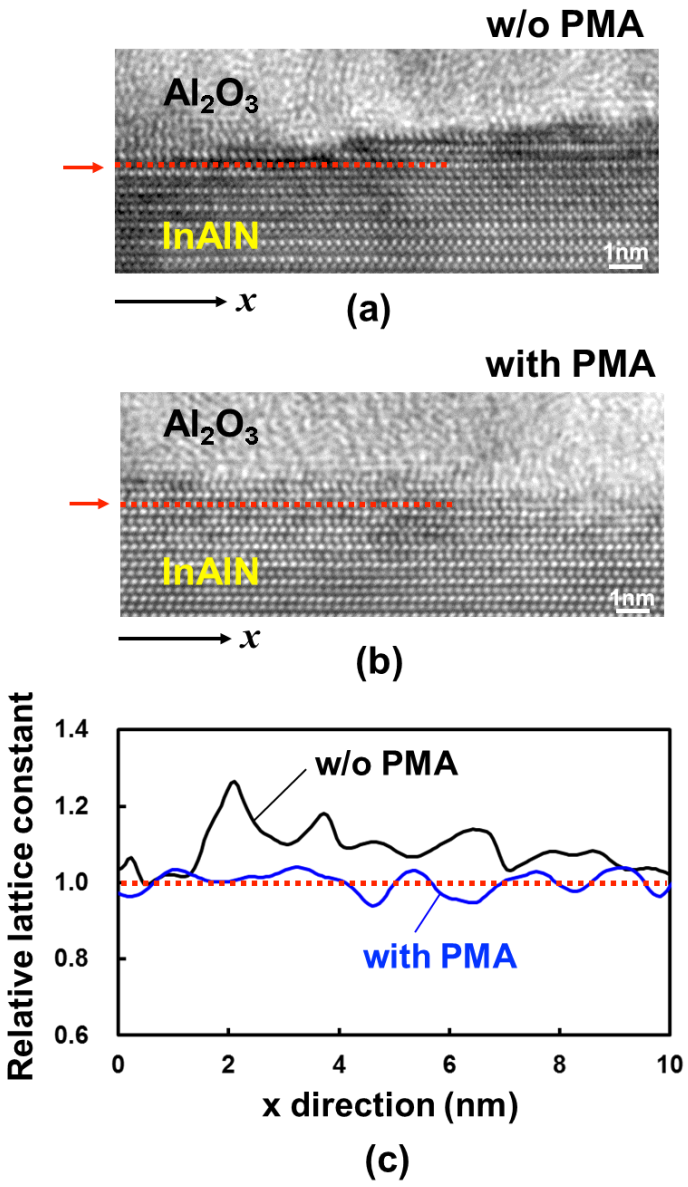

Fig. 6-13. TEM images of Al_2O_3/InAlN interfaces (a) without and (b) with PMA. (c) Comparison of relative lattice constant of InAlN along c-axis at Al_2O_3/InAlN interface.

6.4. Conclusion

We evaluated the DC characteristics and operation stability of Al_2O_3/InAlN/GaN MOS-HEMTs by focusing on PMA process to control the defect levels in Al_2O_3 and the electronic states at the Al_2O_3/InAlN interface. We clarified that the transconductance linearity, the subthreshold slope and the current collapse were improved by PMA, indicating the reduction in electronic states at the Al_2O_3/InAlN interface, which were evaluated by photo-assisted *C–V* measurements. Before PMA, high-density electronic states near midgap existed at the Al_2O_3/InAlN interface, and these interface states were effectively reduced after PMA. Furthermore, TEM analysis of the Al_2O_3/InAlN structures revealed that the bond disorder at the Al_2O_3/InAlN interface was significantly recovered after PMA. It is considered that PMA process is effective in enhancing the relaxation of dangling bonds and/or point defects at the Al_2O_3/InAlN interface. Consequently, the interface state densities were effectively reduced, leading to the improved gate controllability and operation stability for the Al_2O_3/InAlN/GaN MOS-HEMTs. The obtained results indicate that the present PMA process is promising for improving performance and operation stability of Al_2O_3/InAlN/GaN MOS-HEMTs.

References

1) T. Kikkawa, Jpn. J. Appl. Phys. **44**, 4846 (2005).
2) J. Kuzmik, IEEE Electron Device Lett. **22**, 510 (2001).
3) K. Joshin, K. Makiyama, S. Ozaki, T. Ohki, N. Okamoto, Y. Niida, M. Sato, S. Masuda, and K. Watanabe, IEICE Trans. Electron. E97-C, 923 (2014).
4) S. Ozaki, K. Makiyama, T. Ohki, Y. Kamada, M. Sato, Y. Niida, N. Okamoto, and K. Joshin, Phys. Status Solidi **A** 213, 1259, (2015).
5) K. Makiyama, S. Ozaki, T. Ohki, N. Okamoto, Y. Minoura, Y. Niida, Y. Kamada, K. Joshin, K. Watanabe and Y. Miyamoto, IEDM Tech. Dig. 213 (2015).
6) J. Kotani, A. Yamada, T. Ishiguro, S. Tomabechi, and N. Nakamura, Appl. Phys. Lett. **108**, 152109 (2016).
7) Z. Yatabe, J. T. Asubar, and T. Hashizume, J. Phys. D: Appl. Phys. **49**, 393001 (2016).
8) T. Hashizume, K. Nisgiguchi, S. Kaneki, J. Kuzmik and Z. Yatabe, Mat. Sci. Semicond. Process. **78**, 85 (2018).
9) K. Nishiguchi, S. Kaneki, S. Ozaki and T. Hashizume, Jpn. J. Appl. Phys. **56**, 101001 (2017).
10) G. Pozzovivo, J. Kuzmik, S. Golka, W. Schrenk, G. Strasser, D. Pogany, K. Čičo, M. Ťapajna, K. Fröhlich, J. Carlin, M. Gonschorek, E. Feltin, and N. Grandjean: Appl. Phys. Lett. **91**, 043509 (2007).
11) Z. Hu, Y. Yue, M. Zhu, B. Song, S. Ganguly, J. Bergman, D. Jena, and H. Xing, Appl. Phys. Express **7**, 031002 (2014).
12) M. Lachab, M. Sultana, Q. Fareed, F. Husna, V. Adivarahan, and A. Khan, J. Phys. D: Appl. Phys. **47**, 135108 (2014).
13) J. Freedsman, A. Watanabe, Y. Urayama, and T. Egawa: Appl. Phys. Lett. **107**, 103506 (2015).
14) H. Zhou, X. Lou, N. Conrad, M. Si, H. Wu, S. Alghamdi, S. Guo, R. Gordon, and P. Ye, IEEE Electron Device Lett. **37**, 556 (2016).
15) Z. Yatabe, Y. Hori, W. Ma, J. T. Asubar, M. Akazawa, T. Sato, and T. Hashizume: Jpn. J. Appl. Phys. **53**, 100213 (2014).
16) Y. Hori, Z. Yatabe, and T. Hashizume, J. Appl. Phys. **114**, 244503 (2013).
17) S. Ozaki, T. Ohki, M. Kanamura, N. Okamoto, and T. Kikkawa, Jpn. J. Appl. Phys. **52**, 11NG04 (2013).
18) S. Ozaki, K. Makiyama, T. Ohki, Y. Kamada, M. Sato, Y. Niida, N. Okamoto, and K. Joshin, IEEE Trans. Semicond. Manufacturing **29**, 370 (2016).

19) M. Choi, J. L. Lyons, A. Janotti, and C. G. Van de Walle, Phys. Status Solidi B **250**, 787 (2013).
20) M. Akazawa, M. Chiba, and T. Nakano, Appl. Phys. Lett. **102**, 231605 (2013).
21) T. Nakano, M. Chiba, and M. Akazawa, Jpn. J. Appl. Phys. **53**, 04EF06 (2014).
22) S. Ozaki, K. Makiyama, T. Ohki, N. Okamoto, S. Kaneki, K. Nishiguchi, N. Hara, and T. Hashizume, Appl. Phys. Express **10**, 061001 (2017).
23) S. Kaneki, J. Ohira, S. Toiya, Z. Yatabe, J. Asubar, and T. Hashizume: Appl. Phys. Lett. **109**, 162104 (2016).
24) Y. Wang, Q. Ma, L. Zheng, W. Liu, S. Ding, H. Lu, and D. Zhang: IEEE Trans. Electron Devices. **63**, 1893 (2016).
25) M. Miczek, C. Mizue, T. Hashizume, and B. Adamowicz: J. Appl. Phys. **103**, 104510 (2008).
26) P. Jonnarda, C. Bonnelle, G. Blaise, G. Re´mond, and C. Roques-Carmes: J. Appl. Phys. **88**, 6413 (2000).
27) W. S. Tan, P. A. Houston, G. Hill, R. J. Airey, and P. J. Parbook: J. Electron. Mater. **33**, 400 (2004).
28) G. Krautheim, T. Hecht, S. Jakschik, U. Schro¨der, and W. Zahn: Appl. Surf. Sci. **252**, 200 (2005).
29) J. L. van Hemmen, S. B. S. Heil, J. H. Klootwijk, F. Roozeboom, C. J. Hodson, M. C. M. van de Sanden, and W. M. M. Kessels: J. Electrochem. Soc. **154**, 165 (2007).
30) M. Azize, A. L. Hsu, O. I. Saadat, M. Smith, X. Gao, S. Guo, S. Gradeˇcak, and T. Palacios: IEEE Electron Device Lett. **32**, 1680 (2011).
31) S. Joglekar, M. Azize, E. J. Jones, D. Piedra, S. Gradeˇcak, and T. Palacios: IEEE Trans. Electron Devices. **63**, 318 (2016).
32) C. M. Jeon, and J. Leea: Appl. Phys. Lett. **86**, 172101 (2005).
33) D. Cociorva, W. G. Aulbur, and W. Wilkins: Solid State Commun. **124**, 63 (2002).
34) R. Vetury, N. Q. Zhang, S. Keller and U. K. Mishra, IEEE Trans. Electron Devices. **48**, 560 (2001).
35) W. Saito, T. Nitta, Y. Kakiuchi, Y. Saito, K. Tsuda, I. Omura and M. Yamaguchi, IEEE Trans. Electron Devices. **54**, 1825 (2007).
36) S. Arulkumaran, I. G. Ng, C. H. Lee, Z. H. Liu, K. Radhakrishnan, N. Dharmarasu and Z. Sun, Solid-State Electron. **54**, 1430 (2010).
37) R. J. Trew, D. S. Green and J. B. Shealy, IEEE Microwave Mag. **10**, 116 (2009).
38) J. Kotani, M. Tajima, S. Kasai and T. Hashizume, Appl. Phys. Lett. **91**, 093501 (2007).
39) K. Nishiguchi, J. T. Asubar, and T. Hashizume, Jpn. J. Appl. Phys. **53**, 070301

(2014).
40) K. Cico, D. Gregušová, J. Kuzmík, M. Jurkovic, A. Alexewicz, M. A. di Forte Poisson, D. Pogany, G. Strasser, S. Delage and K. Fröhlich: Solid-State Electron. **67**, 74 (2012).
41) C. Mizue, Y. Hori, M. Miczek, and T. Hashizume, Jpn. J. Appl. Phys. **50**, 021001 (2011).
42) Z. Yatabe, Y. Hori, S. Kim and T. Hashizume, Appl. Phys. Express **6**, 016502 (2013).
43) Q. K. Xue, Q. Z. Xue, R. Z. Bakhtizin, Y. Hasegawa, I. S. T. Tsong, and T. Sakurai, Phys. Rev. Lett. **82**, 3074 (1999).
44) H. Hasegawa and H. Ohno, J. Vac. Sci. Technol. B **4**, 1130 (1986).
45) R. V. Galatage, D. M. Zhernokletov, H. Dong, B. Brennan, C. L. Hinkle, R. M. Wallace, and E. M. Vogel, J. Appl. Phys. **116**, 014504 (2014).
46) T. K. Zywietz, J. Neugebauer and M. Scheffler: Appl. Phys. Lett. **74**, 1695 (1999).

Chapter 7

Conclusion

This thesis aimed at the characterization and control of electronic states in Al_2O_3-based insulated-gate structures by focusing on fabrication processes, to improve the performance and the operation stability of GaN metal-oxide-semiconductor high electron mobility transistors (MOS-HEMTs).

Chapter 1 started with the introduction of the requirement for next generation wireless communication systems represented by the 5th-generation mobile communication system (5G). GaN-based HEMTs have enormous potential as high-frequency devices used in power amplifiers for wireless base stations. In addition, insulated-gate structures are effective for improving the performance of GaN HEMTs. However, several problems remain unsolved, such as the instability of the threshold voltage (V_{th}), a steep decrease in transconductance (g_m) at the forward gate bias, and severe current collapse.

Chapter 2 explained the physical properties of III-N semiconductors and their heterostructures, followed by the generation mechanism of two-dimensional electron gas (2DEG). In the case of AlGaN/GaN HEMTs, a high-density and high-mobility electron channel could be generated at the undoped-AlGaN/GaN interface due to spontaneous and piezoelectric polarization, without the impurity scattering. This characteristic is well suited for power amplifiers used in high-frequency applications.

Chapter 3 discussed the origin and effects of the electronic states induced at the interface between insulators and GaN-based materials. The evaluation methods of the interface states were explained, focusing on the capacitance–voltage (*C*–*V*) characteristics of the MOS structures. In the case of wide bandgap semiconductors, not all the interface states can emit electrons due to the longer time constants compared to the actual *C*–*V* measurement time. Thus, photo-assisted *C*–*V* measurement is necessary to characterize the interface states near the midgap of GaN-based MOS-HEMTs.

Chapter 4 introduced the experimental results obtained for this thesis. The mechanism for V_{th} shift of AlGaN/GaN MOS-HEMTs was investigated when using atomic-layer-deposited (ALD)-Al_2O_3 for the gate insulator films. As an oxidant source for ALD-Al_2O_3, H_2O vapor and O_2 plasma were compared, and it was found that both $Al(OH)_x$ residues in ALD-Al_2O_3 and GaN oxidation layer at the Al_2O_3/GaN interface affected the V_{th} shift. By increasing the temperature of post-deposition annealing (PDA),

the $Al(OH)_x$ concentration could be decreased, suppressing the V_{th} shift. On the other hand, the GaN oxidation layer at the Al_2O_3/GaN interface was promoted by O_2 plasma and the V_{th} shift of O_2 plasma-Al_2O_3 was larger than that of H_2O vapor-Al_2O_3. Furthermore, it was clarified that the deep trap sites located around 2.58–3.26 eV from the conduction band edge were generated in the oxidized-GaN layer at the Al_2O_3/GaN interface due to plasma-induced damage, and this caused the V_{th} shift when using O_2 plasma. Therefore, the oxidant source was controlled, and the reductions in the V_{th} shift and the gate leakage current was demonstrated by applying a hybrid-Al_2O_3 structure (lower H_2O vapor-Al_2O_3/upper O_2 plasma-Al_2O_3) for AlGaN/GaN MOS-HEMTs.

Chapter 5 discussed the effect of oxidant sources on the performance of InAlN/GaN MOS-HEMTs, by focusing on the surface-oxide of InAlN barrier layers. It was clarified that the surface oxide comprises Al_2O_3 and In_2O_3 when using O_2 plasma oxidation, and In_2O_3 causes gate leakage and current collapse of InAlN/GaN MOS-HEMTs due to its narrow bandgap and electron traps such as oxygen vacancies. Then, the H_2O vapor oxidation was applied to decrease In_2O_3 for the surface-oxide by focusing on the thermal stability of intermediate hydroxide, and demonstrated a reduction in gate leakage current and current collapse of InAlN/GaN MOS-HEMTs with H_2O vapor.

Chapter 6 investigated the DC characteristics and operation stability of Al_2O_3/InAlN/GaN MOS-HEMTs by focusing on the post-metallization annealing (PMA) process to control the defect levels in Al_2O_3 and the electronic states at the Al_2O_3/InAlN interface. It was clarified that the transconductance linearity, the subthreshold slope, and the current collapse were improved by PMA, indicating a reduction in electronic states at the Al_2O_3/InAlN interface, which were evaluated by photo-assisted *C–V* measurements. Before PMA, high-density near-midgap electronic states existed at the Al_2O_3/InAlN interface, and these interface states were effectively reduced after PMA. Furthermore, TEM analysis of the Al_2O_3/InAlN structures revealed that the bond disorder at the Al_2O_3/InAlN interface was significantly recovered after PMA. It is considered that PMA process is effective in enhancing the relaxation of dangling bonds and/or point defects at the Al_2O_3/InAlN interface. Consequently, the interface state densities were effectively reduced, leading to improved gate controllability and operation stability for the Al_2O_3/InAlN/GaN MOS-HEMTs.

The results presented in this thesis indicate that the proposed interface controlling processes represented by optimized oxidant sources, PDA, and PMA are promising for improving performance and operation stability for GaN HEMTs using Al_2O_3-based insulated-gate structures, which have enormous potential as high-frequency devices used in next generation wireless communications.

List of publications/conferences/patents/awards

Publications

Journals

1. Shiro Ozaki, Toshihiro Ohki, Masahito Kanamura, Naoya Okamoto, and Toshihide Kikkawa, "Effect of Atomic-Layer-Deposition Method on Threshold Voltage Shift in AlGaN/GaN Metal-Insulator-Semiconductor High Electron Mobility Transistors", Jpn. J. Appl. Phys. **52**, 11NG04-1-4 (2013). (IF=1.452, TC=11)
2. Shiro Ozaki, Kozo Makiyama, Toshihiro Ohki, Yoichi Kamada, Masaru Sato, Yoshitaka Niida, Naoya Okamoto, Satoshi Masuda, and Kazukiyo Joshin, "Reduction in current collapse of AlGaN/GaN HEMTs using methyl silsesquioxane-based low-k insulator films", Phys. Status Solidi A **212**, 1153-1157 (2015). (IF=1.795, TC=3)
3. Shiro Ozaki, Kozo Makiyama, Toshihiro Ohki, Yoichi Kamada, Masaru Sato, Yoshitaka Niida, Naoya Okamoto, and Kazukiyo Joshin, "Surface-oxide-controlled InAlN/GaN MOS-HEMTs with Water Vapor", Phys. Status Solidi A **213**, 1259-1262 (2015). (IF=1.795, TC=2)
4. Shiro Ozaki, Kozo Makiyama, Toshihiro Ohki, Yoichi Kamada, Masaru Sato, Yoshitaka Niida, Naoya Okamoto, and Kazukiyo Joshin, "Millimeter-wave GaN HEMTs with Cavity-gate Structure Using MSQ-based Inter-layer Dielectric", IEEE Trans. Semicond. Manufacturing **29**, 370-375 (2016). (IF=1.336, TC=4)
5. Shiro Ozaki, Kozo Makiyama, Toshihiro Ohki, Naoya Okamoto, Shota Kaneki, Kenya Nishiguchi, Naoki Hara, and Tamotsu Hashizume, "Effects of air annealing on DC characteristics of InAlN/GaN MOS high-electron-mobility transistors using atomic-layer-deposited Al_2O_3", Appl. Phys. Express **10**, 061001-1-4 (2017). (IF=2.555, TC=3)

Proceedings

1. Shiro Ozaki, Toshihiro Ohki, Masahito Kanamura, Tadahiro Imada, Norikazu Nakamura, Naoya Okamoto, Toyoo Miyajima, and Toshihide Kikkawa, "Effect of Oxidant Source on Threshold Voltage Shift of AlGaN/GaN MIS-HEMTs Using ALD-Al_2O_3 Gate Insulator films", CS-MANTECH Tech. Dig., 311-314 (2012).
2. Shiro Ozaki, Kozo Makiyama, Toshihiro Ohki, Yoichi Kamada, Masaru Sato, Yoshitaka Niida, Naoya Okamoto, and Kazukiyo Joshin, "Millimeter-wave GaN

HEMTs with Cavity-gate Structure Using MSQ-based Inter-layer Dielectric", CS-MANTECH Tech. Dig., 27-30 (2016).

3. 尾崎史朗, 多木俊裕, 金村雅仁, 今田忠紘, 中村哲一, 岡本直哉, 宮島豊生, 吉川俊英, "原子層堆積 Al_2O_3 を用いた絶縁ゲート型 GaN-HEMT の閾値シフト低減", 電子情報通信学会技術研究報告書, Vol. 112, No. 327, ED2012-75, pp. 41-44 (2012).
4. 尾崎史朗, 牧山剛三, 多木俊裕, 鎌田陽一, 佐藤優, 新井田佳孝, 岡本直哉, 増田哲, 常信和清, "MSQ Low-k 絶縁膜を用いたミリ波帯 GaN-HEMT の電流コラプス抑制", 電子情報通信学会技術研究報告書, Vol. 114, No. 337, ED2014-90, pp. 81-84 (2014).
5. 尾崎史朗, 牧山剛三, 多木俊裕, 鎌田陽一, 佐藤優, 新井田佳孝, 岡本直哉, 常信和清, "水蒸気を用いた表面酸化制御 InAlN/GaN MOS-HEMT", 電子情報通信学会技術研究報告書, Vol. 116, No. 158, ED2016-27, pp. 1-4 (2016).

Journals related to this study

1. Kozo Makiyama, Toshihiro Ohki, Naoya Okamoto, Masahito Kanamura, Satoshi Masuda, Yasuhiro Nakasha, Kazukiyo Joshin, Kenji Imanishi, Naoki Hara, Shiro Ozaki, Norikazu Nakamura, Toshihide Kikkawa, "High-power GaN-HEMT with low current collapse for millimeter-wave amplifier", Phys. Status Solidi C **8**, 2442-2444 (2011).
2. Kazukiyo Joshin, Kozo Makiyama, Shiro Ozaki, Toshihiro Ohki, Naoya Okamoto, Yoshitaka Niida, Masaru Sato, Satoshi Masuda, and Keiji Watanabe, "Millimeter-wave GaN HEMT for power amplifier applications", IEICE Trans. Electron. E97-C, 923 (2014).
3. Kenya Nishiguchi, Shota Kaneki, Shiro Ozaki, and Tamotsu Hashizume, "Current linearity and operation stability in Al_2O_3-gate AlGaN/GaN MOS high electron mobility transistors", Jpn. J. Appl. Phys. **56**, 101001-1-8 (2017).

Conferences

International conferences

1. Shiro Ozaki, Toshihiro Ohki, Masahito Kanamura, Tadahiro Imada, Norikazu Nakamura, Naoya Okamoto, Toyoo Miyajima, and Toshihide Kikkawa, "Effect of Oxidant Source on Threshold Voltage Shift of AlGaN/GaN MIS-HEMTs Using ALD-Al_2O_3 Gate Insulator films", CS-MANTECH 2012 (International Conference on Compound Semiconductor Manufacturing Technology) / Boston, Massachusetts,

USA

2. Shiro Ozaki, Toshihiro Ohki, Masahito Kanamura, Naoya Okamoto, and Toshihide Kikkawa, “Effect of ALD Method on Threshold Voltage Shift in AlGaN/GaN MIS-HEMTs”, ISPlasma 2013 (International Symposium on Advanced Plasma Science and its Applications) / Nagoya, Japan
3. Shiro Ozaki, Kozo Makiyama, Toshihiro Ohki, Yoichi Kamada, Masaru Sato, Yoshitaka Niida, Naoya Okamoto, Satoshi Masuda, and Kazukiyo Joshin, “Reduction in current collapse of AlGaN/GaN HEMTs using MSQ-based low-k insulator films”, IWN 2014 (International Workshop on Nitride Semiconductors) / Wroclaw, Poland
4. Shiro Ozaki, Kozo Makiyama, Toshihiro Ohki, Yoichi Kamada, Masaru Sato, Yoshitaka Niida, Naoya Okamoto, and Kazukiyo Joshin, “Surface-oxide-controlled InAlN/GaN MOS-HEMTs with Water Vapor”, ICNS 2015 (International Conference on Nitride Semiconductors) / Beijing, China
5. Shiro Ozaki, Kozo Makiyama, Toshihiro Ohki, Yoichi Kamada, Masaru Sato, Yoshitaka Niida, Naoya Okamoto, and Kazukiyo Joshin, “Millimeter-wave GaN HEMTs with Cavity-gate Structure Using MSQ-based Inter-layer Dielectric”, CS-MANTECH 2016 (International Conference on Compound Semiconductor Manufacturing Technology) / Miami, Florida, USA
6. Shiro Ozaki, Kozo Makiyama, Toshihiro Ohki, Atsushi Yamada, Junji Kotani, Yoshitaka Niida, Masaru Sato, Yoichi Kamada, Motonobu Sato, Naoya Okamoto, and Norikazu Nakamura, “Ultra-thin Al_2O_3 Atomic Layer Deposition on H2O-pretreated InAlN/GaN MIS-HEMTs”, SISC 2016 (IEEE Semiconductor Interface Specialists Conference) / San Diego, California, USA
7. Shiro Ozaki, Kozo Makiyama, Yoshitaka Niida, Toshihiro Ohki, Naoya Okamoto, Yuichi Minoura, Masaru Sato, Yoichi Kamada, Kazukiyo Joshin, and Keiji Watanabe, “GaN-HEMT Device Technologies for W-band High-Power Amplifier”, AWAD 2017 (Asia-Pacific Workshop on Fundamentals and Applications of Advanced Semiconductor Devices) / Gyeongju, Korea
8. Shiro Ozaki, Kozo Makiyama, Toshihiro Ohki, Yoichi Kamada, Masaru Sato, Yoshitaka Niida, Naoya Okamoto, and Kazukiyo Joshin, “Cavity-gate Structure for Millimeter-wave GaN HEMTs Using MSQ-based Inter-layer Dielectric”, TWHM 2017 (Topical Workshop on Heterostructure Microelectronics) / Kirishima, Japan

Domestic conferences

1. 尾崎史朗, 多木俊裕, 金村雅仁, 今田忠紘, 中村哲一, 岡本直哉, 宮島豊生, 吉川俊英, “原子層堆積 Al_2O_3 を用いた絶縁ゲート型 GaN-HEMT の閾値シフト低減”, 電子情報通信学会電子デバイス研究会, 大阪府 (2012 年 11 月).
2. 尾崎史朗, 多木俊裕, 金村雅仁, 今田忠紘, 中村哲一, 岡本直哉, 宮島豊生, 吉川俊英, “ALD-Al_2O_3 を用いた絶縁ゲート型 GaN-HEMT の閾値シフト低減”, 第 60 回応用物理学会春季学術講演会, 27P-G4-11, 神奈川県 (2013 年 3 月).
3. 尾崎史朗, 牧山剛三, 多木俊裕, 鎌田陽一, 佐藤優, 新井田佳孝, 岡本直哉, 増田哲, 常信和清, “MSQ Low-k 絶縁膜を用いたミリ波帯 GaN-HEMT の電流コラプス抑制”, 電子情報通信学会電子デバイス研究会, 大阪府 (2014 年 11 月).
4. 尾崎史朗, 牧山剛三, 多木俊裕, 鎌田陽一, 佐藤優, 新井田佳孝, 岡本直哉, 常信和清, “水蒸気を用いた表面酸化制御 InAlN/GaN MOS-HEMT”, 電子情報通信学会電子デバイス研究会, 東京都 (2016 年 7 月).
5. 尾崎史朗, “ALD-Al_2O_3 を用いた絶縁ゲート型 GaN-HEMT”, 日本真空学会研究例会, 東京都 (2016 年 12 月).

Patents

1. 尾崎史朗, 金村雅仁, 中村哲一, 宮島豊生, 武田正行, 渡部慶二, 吉川俊英, 今西健治, 多木俊裕, 今田忠紘, “半導体装置及び半導体装置の製造方法”, 特許第 5636867 号 (平成 26 年 10 月 31 日登録)
2. 尾崎史朗, 武田正行, “エッチングする方法及びエッチング装置”, 特許第 5750951 号 (平成 27 年 5 月 29 日登録)
3. 尾崎史朗, “半導体装置の製造方法”, 特許第 5957994 号 (平成 28 年 7 月 1 日登録)
4. 尾崎史朗, “半導体装置”, 特許第 6107922 号 (平成 29 年 3 月 17 日登録)
5. 尾崎史朗, 岡本直哉, “化合物半導体装置及びその製造方法”, 特許第 6237429 号 (平成 29 年 11 月 10 日登録)

Awards

1. 5th International Symposium on Advanced Plasma Science and its Applications for Nitrides and Nanomaterials (ISPlasma), Best Presentation Award, “Effect of ALD Method on Threshold Voltage Shift in AlGaN/GaN MIS-HEMTs” (2013年2月1日)
2. 11th International Conference on Nitride Semiconductors (ICNS), Best Poster Award, “Surface-oxide-controlled InAlN/GaN MOS-HEMTs with Water Vapor” (2015 年 9 月 3 日)

3. 2016 International Conference on Compound Semiconductor Manufacturing Technology (CS-MANTECH), He Bong Kim Award (Honorable Mention), “Millimeter-wave GaN HEMTs with Cavity-gate Structure Using MSQ-based Inter-layer Dielectric” (2017 年 5 月 23 日)